

# 15<sup>th</sup> Annual Alberta Biomedical Engineering Conference Program and Proceedings



October 24<sup>th</sup> – 26<sup>th</sup>, 2014  
Banff Park Lodge  
Banff, Alberta





We gratefully acknowledge the support of our sponsors  
for making this conference a success



NSERC CREATE Training Program  
for Biomedical Engineers for the  
21st Century



UNIVERSITY OF  
CALGARY

BME Graduate Program



McCaig Institute  
*for Bone and Joint Health*



SCHULICH  
School of Engineering



Schulich Student Activities Fund

Zymetrix

BOSE Biomaterial & Tissue Engineering  
Technology Development Centre

LIBIN  
CARDIOVASCULAR  
INSTITUTE of Alberta

ET The Institution of  
Engineering and Technology

SCHULICH  
School of Engineering



Centre for Bioengineering Research and Education

C  
B  
R  
E





# 15<sup>th</sup> Alberta Biomedical Engineering Conference Banff 2014



October 24-26, 2014  
Banff Park Lodge  
Banff, AB

## PROGRAM COMMITTEE

### CONFERENCE ORGANIZERS

Co-Chairs

Michael Kallos, University of Calgary  
Roman Krawetz, University of Calgary  
Christopher Dennison, University of Alberta

Student Co-Chairs

Chris Sarsons, Maria Engel, University of Calgary

### ABSTRACT REVIEWERS

University of Calgary

Roman Krawetz  
Richard Frayne  
Brent Edwards  
Carolyn Anglin  
Kartikeya Murari  
Neil Duncan  
Elena Di Martino  
Michael Kallos  
Steve Boyd

## 15<sup>th</sup> Alberta Biomedical Engineering Conference

University of Alberta

Christopher Dennison  
Jason Carey  
Larry Unsworth  
Albert Vette  
Carolyn Van Toen

### POSTER JUDGES

University of Calgary

John Bertram  
Signe Bray  
Brent Edwards  
Anders Nygren

University of Alberta

Doug Hill  
Andrew Martin

### PODIUM JUDGES

University of British Columbia  
Robarts Institute

Dr. Gunter P. Siegmund  
Dr. Robert Bartha

### TRAINEE VOLUNTEERS

University of Calgary

Christopher Sarsons	Student co-chair; student organizer, undergraduate funding, great challenge, AV organization, volunteer recruitment, registration package assembly
Maria Engel	Student organizer, social event planning, great challenge, volunteer recruitment, registration table, registration package assembly
Isaac Acosta Calvillo	Student organizer, ordering registration gifts, registration package assembly
Muhammad S. Noor	Fundraising, podium session chair
Ali Melia	Fundraising, registration table, podium session chair
Sam Dorosz	Fundraising
Krysta Powers	Great challenge
Michael Purdy	Registration table
Karri Bertram	Registration table
Shrushrita Sharma	Registration table
Jaqueline Rios	Registration table
Giampaolo Martufi	Registration package assembly, podium session chair
Warren Xu	Registration package assembly
Jillian Beveridge	Registration package assembly
Lin Hui	Registration package assembly
Daniel Comaduran	Registration package assembly
Marquez	Registration package assembly
Erin Hildebrandt	Registration package assembly, podium session chair
Chris Waters	Photography, podium session chair
Eng Kuan Moo	Podium session chair
Mohsen Maleki	Podium session chair
John Sevick	Podium session chair
Jane Desrochers	Podium session chair
Stefan Hoerzer	Podium session chair

## 15<sup>th</sup> Alberta Biomedical Engineering Conference

Kevin Bolt	Registration table
An Le	Registration package assembly
Shah Iqbal	Registration package assembly

University of Alberta	Brooklyn Knowles	Student organizer, volunteer recruitment
	Nam Huynh	Volunteer
	Hamed Nazeri	Volunteer

### CONFERENCE EVENT COORDINATOR

University of Calgary

Elizabeth Mullaney

**Thank you to Amanda Lottermoser, NSERC Create Training Program (Admin)**

**A BIG THANK YOU TO ALL OF OUR VOLUNTEERS WHO HELPED WITH THE ORGANIZATION AND PLANNING OF OUR CONFERENCE THIS YEAR!**

**A SPECIAL THANK YOU TO  
LISA MAYER FOR HER ONGOING SUPPORT  
OF THE BME CONFERENCE.**

# PROGRAM

**Podium sessions are in the Summit Assiniboine room.**

**Poster sessions are in the Castle and Alpine Meadows rooms.**

**You must wear your name badge in order to access all meals and conference events (podium, poster sessions, coffee breaks).**

## FRIDAY

4:30 - 8:30 pm

**REGISTRATION and CHECK-IN – Banff Park Lodge Lobby**

7:30 pm

**Opening Reception – Glacier Salon**  
**Welcome: Dr. Michael Kallos**

## SATURDAY

7:00 – 8:00 am

**BREAKFAST – Glacier Chinook**

8:00 – 8:05 am

**Welcoming Remarks – Summit Assiniboine**  
Dr. Christopher Dennison and Dr. Roman Krawetz

8:05 – 8:45 am

**Guest Speaker #1: Dr. Gunther Siegmund, MEA Forensic Engineers & Scientists**

**Session Chairs:** Stefan Hoerzer and Giampaolo Martufi

8:45 – 9:55 am

**Student Podium Presentation Session #1**

**Session Chairs:** Eng Kuan Moo and Mohsen Maleki

- |                     |    |   |
|---------------------|----|---|
| Krysta Powers       | 01 | Force Enhancement; a Titin Achievement in Skeletal Muscle   |
| Luca Li             | 02 | Predicting the Impact of Surgery on Quality of Life and Risk Management in Patients Afflicted with Glioblastoma Multiforme                    |
| Mason Kim           | 03 | Numerical analysis of LIPUS induced mechanical stresses in dentoalveolar structure using a three-dimensional finite element model             |
| Christopher Besflug | 04 | pQCT-based Indices of Bone Strength Under Axial and Combined Loading Differentiate Older Women With and Without Recent Distal Radial Fracture |

## 15<sup>th</sup> Alberta Biomedical Engineering Conference

Elham Behradfar 05 Intracellular uncoupling in cardiac tissue accelerates impulse propagation by activating more Purkinje-myocardial junctions

Ryan Lewinson 06 Biomechanical Control Conditions for Footwear Insole and Orthotic Research

9:55 - 11:10 am

### **Poster Session #1 (ODD NUMBERED POSTERS)**

#### **COFFEE/BEVERAGE BREAK**

#### **Castle and Alpine Meadows**

**Judges:** Dr. John Bertram, Dr. Signe Bray, Dr. Brent Edwards, Dr. Anders Nygren, University of Calgary; Dr. Chris Dennison, Dr. Doug Hill, Dr. Andrew Martin, University of Alberta

- Mehdi Jamshidi 01 Validated Simulation Model for Evaluating Radial Force of New Stent Design
- Robert C. Butz 03 Novel force sensing system for studying head-helmet contact in simulated impacts
- Jaspreet Kaur 05 Fitting single cell cardiac ventricular myocyte model to biological membrane resistance and AP data reduces mean square error in voltage and membrane resistance
- Kate O'Brien 07 **Site Specific Inflammation and Cellular Composition of Synovial Tissue Within Osteoarthritic Knee Joints**
- Stefan Hoerzer 09 The Influence of Footwear on Gait Asymmetry
- A. Salari 11 AC Electrothermal Biofluid Transport, Numerical Study on the Substrate Thermal Conductivity
- S. Majid Nazemi 13 Prediction of Local Proximal Tibial Subchondral Bone Stiffness using Subject-Specific Finite Element Modeling: Effect of anisotropy inclusion
- Alyssa Mah 15 Detecting motion-corrupted data in diffusion tensor imaging data: applications for pediatric imaging
- Andres Kroker 17 Estimated Bone Strength by Finite Element Analysis at Distal Skeletal Sites Predicts Femoral Failure Load
- Zohreh Salimi 19 Investigating Validation of Physiological Cost Index for Wheelchair Users
- Svetlana Kuznetsova 21 In Situ Chondrocyte Mechanics Following Static And Dynamic Compressive Stresses
- Allison McPeak 23 Effect Of Counterface On Cartilage Boundary Lubricating Ability By Hyaluronan And Proteoglycan 4: Cartilage-Cartilage vs Cartilage-Glass

## 15<sup>th</sup> Alberta Biomedical Engineering Conference

- S. M. M. Shekarforoush 25 A research proposal about the association between the development of osteoarthritis and changes in the relative velocity of joint surfaces following Anterior Cruciate Ligament (ACL) and Medial Collateral Ligament (MCL) transection
- Fraz Anjum 27 PCL/Gelatin nanofiber mats for grafting human skin-derived precursor cells (hSKPs) into skin wounds
- Maria Engel 29 Muscle Morphology of the Spastic Mice
- Kaleena Johnston 31 An Examination of Sarcomere Length Non-Uniformities in Actively Stretched Muscle Myofibrils
- Morteza Amini 33 HR-pQCT FE derived bone strength differentiates between older women with and without recent distal radial fracture
- Nathanial K. Maeda 35 Clinically Usable Real-Time Simulation of Lumbar Spine Model
- Scott Moorman 37 Visualization of Collagen Crimp in Annulus Fibrosus using Ultra-High Field 9.4T MRI
- Michael Purdy 39 Electrical stimulation of a rat sciatic nerve using an addressable-electrode nerve conduit
- Kevin Shin 41 Integrin  $\alpha 1\beta 1$  Increases Signs of Post-traumatic Osteoarthritis in a Tissue Specific Manner
- Paniz Adibpour 43 Investigation of Factors that Impact Compressed sensing Reconstruction Resolution
- Amin Ghazanfari 45 Measurements of Anisotropy Ratio and Fiber Orientation in Cardiac Tissue Propagation
- Matthew P. McDonald 47 Validating pQCT-based Indices of Distal Radius Bone Strength under Combined Loading
- Nicolas Dietrich 49 A Novel Method for Comparison of Scan Greyscale Values Acquired Using Cone-Beam CT
- Hanieh Arjmand 51 Investigating associations between OA-related knee pain and mechanical behavior using subject-specific finite element modeling of the knee

11:10 – 12:30 pm

### **Student Podium Presentation Session #2**

**Session Chairs:** Chris Waters-Banker and Stefan Hoerzer

- Matthew Walton 07 Language Ability and White Matter Structure in Preschool Aged Children: A TBSS study

## 15<sup>th</sup> Alberta Biomedical Engineering Conference

Amirali Toossi 08 Towards human intraspinal microstimulation implants: Mechanical stability and implications for lead-wire design

N. Ghazavi 09 Knee pain is associated with osteophyte size

Katherine Evans 10 Optimizing Tactor Parameters to Improve Discrimination for Sensory Feedback in Upper Limb Amputees

Rafael Fortuna 11 Persistent muscle weakness and contractile material loss in a clinically relevant Botulinum toxin type-A (BTX-A) injection protocol

Erin Hildebrandt 12 What is the bilateral asymmetry of radius and tibia bone microarchitecture by HR-pQCT?

Milan Todorovic 13 Engineering Pseudoislets for Transplantation Applications

12:30 – 1:45 pm

**LUNCH – Glacier Chinook**

1:45 – 2:30 pm

**Industry Panel Speakers:**

**Scott Phillips**, President, Starfish Medical

**Benjamin D. Sullivan**, Chief Scientific Officer, TearLab

**Session Chairs:** Jane Desrochers and Giampaolo Martufi

2:30 – 2:35 pm

**BREAK – Group Pictures**

2:35 - 3:50 pm

**Poster Session #2 (EVEN NUMBERED POSTERS)**  
**COFFEE/BEVERAGE BREAK**

**Judges:** Dr. John Bertram, Dr. Signe Bray, Dr. Brent Edwards, Dr. Anders Nygren, University of Calgary; Dr. Chris Dennison, Dr. Doug Hill, Dr. Andrew Martin, University of Alberta

Negar Behzadi Fard 02 Monitoring of pressure during scoliosis surgery

Marcela Rodriguez 04 Comparative Study for Motion Tracking and Image Registration in Cardiac Optical Mapping

Sean Crooks 06 Muscle Fascicle Length is Reduced in Old Age Owing to Shorter Sarcomeres and Serial Sarcomere Loss

Elizabeth Imhof 08 9.4T MRI of a model of pediatric concussion shows vascular abnormalities

Russel S. Fuhrer 10 Viscoelastic Response of Mid-Palatal Suture Tissue in Finite Element Analysis

Karolina Urban 12 Measuring functional connectivity of event related optical signals by optical imaging

Paria Vakil	14	Application of fiberoptic sensor technology to detect abnormal stress on the cartilage covering the knee joint
Kotaybah Hashamoun	16	Soft Biological Tissues with Statistical Fibre Orientation: Efficient Computation of the Mechanical Properties
Warren Xu	18	Mitochondrial dynamics in the brain of an autistic mouse model (BTBR T+ tf/j) in response to a ketogenic diet
K.R. Boldt	20	Contractile Properties of Cardiac Muscle Following Increasing Doses of Chronic Exercise Training and Overtraining in Rats: MSc Research Proposal
Divya Budihal	22	The Influence of Age, Running Speed, and Running Distance on the Probability of Second Metatarsal Stress Fracture
Quinn Boser	24	Development of a Balance Assessment Tool (BAT) for a Computer-Assisted Rehabilitation Environment
Muhammad S. Noor	26	Parameters of Thalamic DBS and Motor Cortical Perfusion
Alexandra Melia	28	Clinical Validation of Center of Mass using Surface Topography in Adolescent Idiopathic Scoliosis
Mariana Leite	30	Classification of Brain White Matter Lesion on MR Imaging
Katherine Archibold	32	Evaluation of Primary Elbow Osteoarthritis using High-Resolution Peripheral Quantitative Computed Tomography: An Exploratory Study
Daniel Korchinski	34	Developing an Optical Measure of in Vivo Mitochondrial Redox Status in Rodent Brain
Sarah Sanni	36	Comparison of Two Optical Imaging Systems to Reduce Radiation in Adolescents with Scoliosis
Liqun Ning	38	Preliminary study of the Mechanical Properties of Hydrogel Substrates on Cell Viability
Vivian Wang	40	Embryonic Myosin Heavy Chain Expression In Skeletal Muscle As A Marker Of Recovery After Electrical Stimulation Damage
Asmaa Affan	42	Chondrogenic differentiation of synovial progenitors isolated from patients with hip pathologies

## 15<sup>th</sup> Alberta Biomedical Engineering Conference

- Azadeh A. T. Borojeni 44 An idealized branching airway geometry that mimics average aerosol deposition in pediatric central conducting airways
- Thomas Johnson 46 Using multimodal near-infrared spectroscopy and magnetic resonance imaging to measure in-vivo oxidative metabolism in mice
- Cam Cummings 48 Multi Muscle Patterns In Post- Surgical Total Knee Arthroplasty
- Abdullah Al-Ani 50 Micro-tissue engineering for retinal transplant
- Xue Han 52 A novel method to fabricate biodegradable stents for stroke treatment

3:50 – 5:10 pm

### **Student Podium Presentation Session #3**

**Session Chairs:** Eng Kuan Moo and John Sevick

- Brooklynn Knowles 14 Towards a New Severity Index for Assessment of Helmet Performance
- Anita Fung 15 An Approach To Examine The Effect Of Taper Angle And Threading On Periprosthetic Bone Remodeling From Bone-Anchored Amputation Prostheses
- Alexis Jones 16 History Dependence of EMG: Implications for Isometric Steady-State EMG Parameters Following a Lengthening or Shortening Contraction
- W.D. Burnett 17 Knee pain is associated with osteophyte volume and bone mineral density
- Laronna Sewell 18 Functional near infrared spectroscopy: an inexpensive, non-invasive tool to assess brain functional connections in pediatric mild traumatic brain injury patients
- Shiva Ebrahimi Nejad 19 A Model-Based Approach to Diagnosis of Arterial Stenosis
- M.J. Adam 20 Distal Radius Strain Distributions during Off-Axis Loading

6:00 – 7:00 pm

**DINNER – Glacier Chinook**

7:00 pm

**“THE GREAT CHALLENGE”**

8:00 pm

**Social – Elk and Oarsman**  
119 Banff Avenue (2nd Floor, Above The Ski Hub)

**SUNDAY**

7:15 – 8:15 am

**BREAKFAST – Glacier Chinook**

8:15 – 8:45 am

**Checkout**

8:45 – 9:25 am

**Guest Speaker #2: – Dr. Robert Bartha, Robarts Research Institute**

**Session Chairs:** Maria Engel and Muhammad S. Noor

9:25 – 10:20 am

**Student Podium Presentation Session #4**

**Session Chairs:** Chris Waters-Banker and John Sevick

Jens Herzog 21 Is Skeletal Muscle Titin an Activatable Molecular Spring?

J.S. Schofield 22 Providing Kinesthetic Sensory Feedback in Upper Limb Prostheses

Hendrik Enders 23 EEG Activity of the Cerebral Cortex during Rhythmic Lower Limb Movements

Shah Iqbal 24 The Inflammatory Profile of Lubricin

Janna Haladuick 25 Cartilage Boundary Lubricating Ability of PRG4 (Lubricin) Monomers And Multimers With Hyaluronan

10:20-10:40 am

**Poster Session #3 (FINALISTS ONLY)**

**COFFEE/BEVERAGE BREAK**

**Judges:** Dr. John Bertram, Dr. Signe Bray, Dr. Brent Edwards, Dr. Anders Nygren, University of Calgary; Dr. Doug Hill, Dr. Andrew Martin, University of Alberta

10:40 – 11:35 am

**Student Podium Presentation Session #5**

**Session Chairs:** Mohsen Maleki and Jane Desrochers

Scott Sibole 26 Getting More From Image Data: pyCellAnalyst, a 3-D Image Reconstruction and Deformation Analysis Tool

Maurice Mohr 27 High Motor Unit Synchronization between Vastii Muscles during Dynamic Movements

## 15<sup>th</sup> Alberta Biomedical Engineering Conference

- Leandro Solis 28 Identifying the loading threshold conducive to irreversible muscle damage in deep tissue injury
- Alina Ismaguilova 29 The biomechanics and histopathology of aneurysmal growth of the descending aorta post-surgical repair of the ascending aorta
- Karri Bertram 30 The function and influence of ion channels in synovial fluid derived Mesenchymal progenitor cells

11:45 – 12:30 pm

### **Final Award Presentations**

#### **Podium and Poster Prize Presentations – Sponsored by the NSERC CREATE Training Program for Biomedical Engineers for the 21<sup>st</sup> Century**

NSERC CREATE Prize presentations for Most Outstanding Student Posters

- a) Best Overall Poster, b) Most Creative Poster, c) Clearest Message Poster

NSERC CREATE Prize presentations for Most Outstanding Podium Presentations

- 1<sup>st</sup> First Prize, 2<sup>nd</sup> Second Prize, 3<sup>rd</sup> Third Prize

Canadian Society of Biomechanics/Société canadienne de biomécanique

- a) Podium Presentation Prize  
b) Poster Presentation Prize

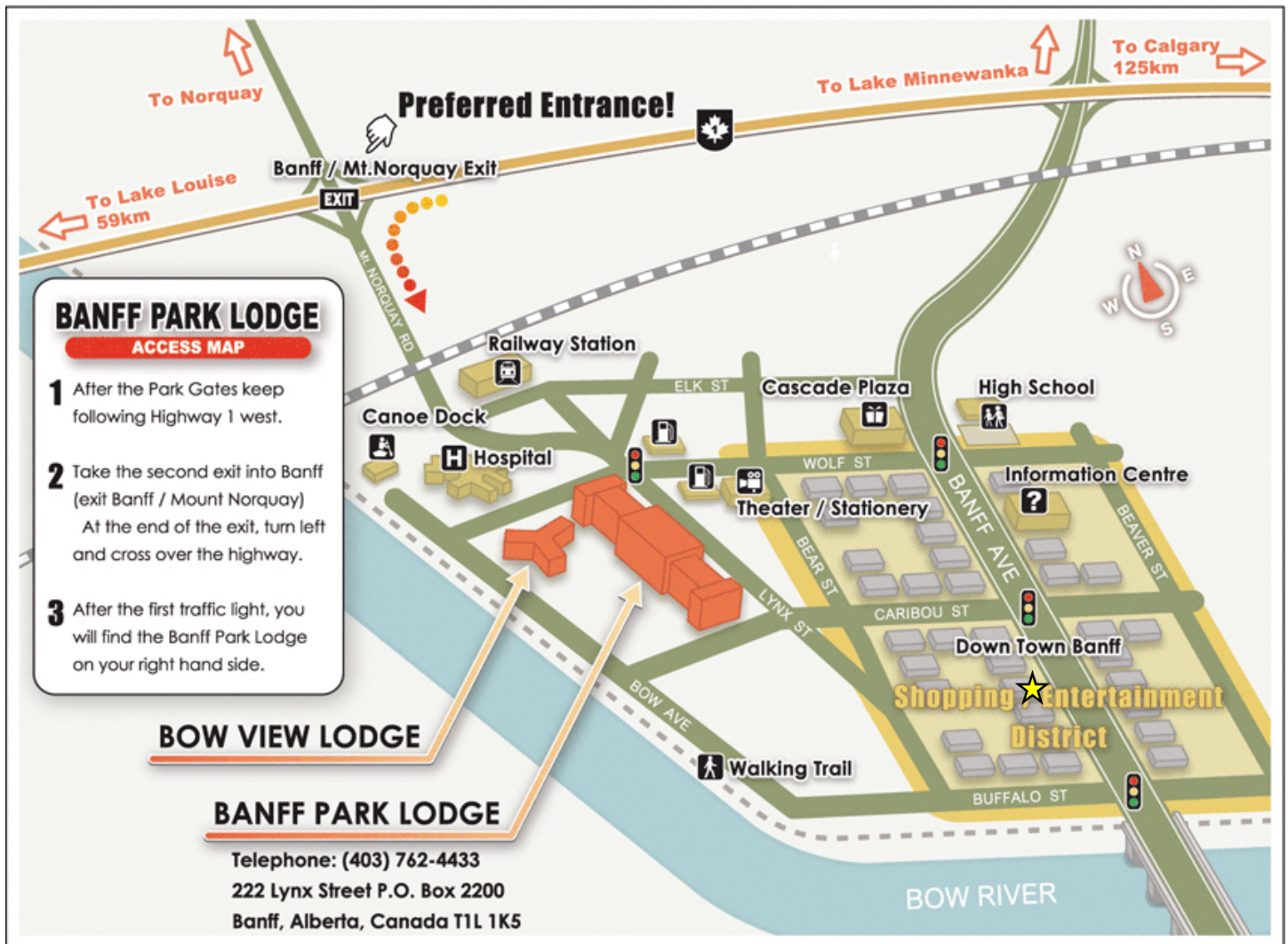
### **CLOSING REMARKS**

Maria Engel, Graduate Student Co-Chair

### **REMINDER**

Please return all name tags and judges' clipboards at end of conference.  
We thank you for your cooperation.

**Map and Meeting Location**



For Saturday night, the Elk and Oarsman (★) is at 119 Banff Avenue (2nd Floor, Above The Ski Hub), just a few blocks from the hotel.

Directions – Walk to the right out of the main hotel entrance.

Turn left onto Caribou Street (first street).

Walk up to Banff Avenue (main street).

Turn right on Banff Ave until you see the Elk and Oarsman on your right (entrance is right next to Lululemon).

Please note: the Elk and Oarsman is on the second floor.

**Guest Speaker #1 – Dr. Gunter P. Siegmund**

**Biography:**

Gunter obtained his Bachelors of Applied Science in Mechanical Engineering and his PhD in Biomechanics at the University of British Columbia. He is a licensed Professional Engineer in both BC and Ontario, and after 11 years as President, is now Director of Research at MEA Forensic Engineers & Scientists. Gunter is also an Adjunct Professor in the School of Kinesiology at the University of British Columbia and co-supervises 3 to 5 graduate students working on research related to whiplash injury, neck muscle neurophysiology and concussion. Gunter has worked on over 3500 forensic cases over 25 years and has published over 150 scientific articles and abstracts related to his research.



**Abstract:**

Whiplash injuries remain the most common and one of the least understood of all automotive injuries. While the risk of most auto-related injuries has fallen over the last few decades, the risk of whiplash injuries has either remained constant or risen. Why is this and what can we do about it? Injury prevention typically involves first understanding the mechanisms responsible for an injury and then developing interventions that attenuate or eliminate the mechanism. With whiplash injury, understanding the mechanism has proven difficult, in part because the injury is difficult to diagnose objectively and in part because the injury suffers from the misperception of being exaggerated or even faked for monetary gain. Furthermore, developing an intervention without completely understanding the mechanism is challenging.

I intend to review a number of proposed mechanisms for whiplash injury and provide some insight into how a seemingly minor collision can generate chronic pain in some individuals. I will also explore evidence of the role that muscles play in the genesis of whiplash injuries, and how we might exploit the human nervous system to help protect the neck during a rear-end crash. And finally I will discuss the introduction of anti-whiplash seats and how we might optimize these seats to mitigate and potentially prevent whiplash injuries.

**Guest Speaker #2 – Dr. Robert Bartha, Robarts Research Institute**

**Biography:**

**Dr. Robert Bartha** is Associate Professor of the Department of Medical Biophysics at Western University, with cross appointments in Medical Imaging and Psychiatry. He is also a Scientist in the Imaging Research Group at the Robarts Research Institute where his research has focused on the development of high-field magnetic resonance imaging and spectroscopy methods for the early diagnosis of disease and monitoring of treatment response; specifically related to neurodegeneration and aging. Dr. Bartha specializes in high magnetic field imaging utilizing a 7 Tesla human MRI scanner, the only one of its kind in Canada, as well as 3 Tesla human and 9.4 Tesla small animal MRI scanners at the Western Centre for Functional and Metabolic Mapping. Dr. Bartha's research is focused on identifying specific imaging biomarkers of disease progression and building novel MRI tracers that highlight pathological aspects of a disease process. His work is highly interdisciplinary involving experts in chemistry, cell biology, and medicine. These collaborations have led to the development of new contrast agents sensitive to physiological conditions such as temperature and pH, new contrast agents targeted to specific proteases upregulated in Alzheimer disease and cancer, and to validate new endogenous metabolic and anatomical biomarkers of disease progression in subjects with Alzheimer disease. Dr. Bartha heads an exciting team that includes research associates, post-doctoral fellows, technicians, and students, with expertise in imaging, physics, and biology. Most recently, the team has expanded to incorporate expertise in software design and image processing as the group focuses on development of novel anatomical biomarkers of disease progression utilizing large databases for validation such as that created by the Alzheimer Disease Neuroimaging Initiative (ADNI). Dr. Bartha is a co-author on over 80 publications, with more than 200 abstracts and numerous invited presentations. He holds funding from the Canadian Institute of Health (CIHR), National Science and Engineering Research Council (NSERC), and the Ontario Institute of Cancer Research (OICR). He was also the recipient of the Ivey BMO Financial Group Scientist in Brain Disorders Imaging research chair. In 2003, he was awarded a *Premier's Research Excellence Award* from the Province of Ontario. For further information, please visit: [www.cfmm.robarts.ca/robert-bartha](http://www.cfmm.robarts.ca/robert-bartha)



**Abstract:**

**Imaging Tissue Temperature and pH with MRI: Applications in Cancer and Stroke**

Magnetic resonance imaging (MRI) is a versatile tool that can be used to monitor brain anatomy, function, metabolism, and physiology. In biological systems including the brain, temperature and pH are tightly regulated and influential in numerous cellular processes including protein synthesis, regulation of neurotransmission, cell volume regulation, and apoptosis. Altered intra- and/or extra-cellular pH occurs in many pathological conditions particularly in cancer and stroke when metabolic demand for oxygen exceeds supply. The measurement of tissue temperature and pH with high temporal and spatial resolution has been challenging. However MRI can be made sensitive to both temperature and pH by exploiting a process known as chemical exchange saturation transfer (CEST). We will describe recent advances to utilize CEST MRI contrast in combination with new MRI contrast agents to measure tissue temperature and pH. We will also highlight a novel technique to measure absolute tissue pH using only endogenous signals. Applications in both cancer and stroke will be presented. Finally, we will demonstrate that acute modification of intracellular pH using a pharmacologic challenge can be monitored by MRI and may represent a novel paradigm for disease detection.

## Industry Panel

**Benjamin Sullivan**, Co-founder and Chief Scientific Officer of TearLab

### Biography:

Benjamin Sullivan is co-founder and Chief Scientific Officer of TearLab (NASDAQ: TEAR, TSX:TLB), co-founder and board member of Lubris LLC, and has provided founding intellectual property for Biological Dynamics LLC & Code Fluidics LLC. Prior to obtaining his Ph.D. in Bioengineering at the University of California, San Diego, Benjamin spent several years researching effects of Dry Eye Disease on molecular profiles of the tear film while at the Schepens Eye Research Institute, an affiliate of Harvard Medical School. Prior to that, he graduated from Boston University in 1997 with a B.S. in Biomedical Engineering, summa cum laude. In 2012, ExecRank named him #41 out of 5,000 of C-level scientific executives in the United States. Benjamin is currently an editor of The Ocular Surface, and has been nominated to serve on the prestigious Tear Film & Ocular Surface Society DEWS II panel.



### Company Profile:

TearLab Corporation develops and markets lab-on-a-chip technologies that enable eye care practitioners to improve standard of care by objectively and quantitatively testing for disease markers in tears at the point-of-care. The TearLab Osmolarity Test, for diagnosing Dry Eye Disease, is the first assay developed for the award winning TearLab Osmolarity System. Headquartered in San Diego, CA, TearLab Corporation's common shares trade on the NASDAQ Capital Market under the symbol TEAR and on the Toronto Stock Exchange under the symbol TLB.

Lubris, LLC is dedicated to the development and commercialization of recombinant human lubricin, a proprietary recombinant form of the human protein Lubricin to treat a wide variety of age and inflammation related conditions, including osteoarthritis, dry eye disease, dry mouth, and women's health.

## Industry Panel - Scott Phillips

### Biography:

Scott is the founder and president of StarFish Medical, the largest medical device development services company in Canada with 60 staff based in Victoria. The company focuses on developing devices with technology innovation and human-centric design aspects for entrepreneurial companies around North America. The company is ISO13485 certified and has won awards in North America and Europe for its designs. Also as the CEO of the StarFish group of companies he oversees ViVitro Labs, a leading prosthetic heart valve testing equipment and services company with customers around the world.



Scott graduated in engineering physics from UBC in 1989. Prior to starting StarFish he spent 10 years in BC and Alberta working at Moli Energy, Alberta Research Council and independently on a variety of technology-focused projects such as lithium batteries, spectroscopy instrumentation and planar magnetic audio speakers.

He is currently since on advisory boards for biomedical engineering at UBC, UVic and BCIT and is a frequent lecturer on biomedical engineering topics at universities and conferences around North America.

### Company Profile:

StarFish is a leading service provider and Medical Device Design company with a full complement of design, development, and manufacturing services. We successfully partner with innovative companies (both large and small) to create breakthrough products for a number of medical specialty areas.

Medical device product definition, technical engineering and product development use our proprietary PathFinder™ process. Prototype and volume production are delivered in an ISO 13485 certified facility with FDA registration and class 100,000 clean room capabilities.

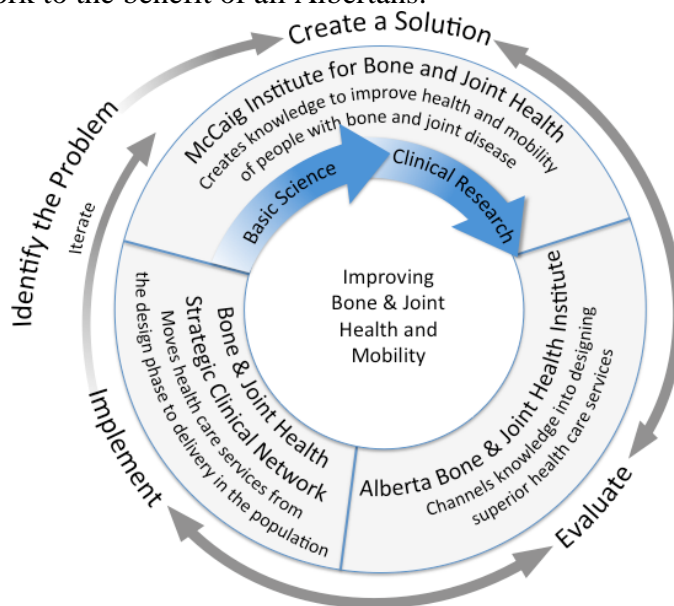
## McCaig Institute for Bone and Joint Health, Gold Sponsor

A healthy bone and joint system keeps us mobile, and thus plays a pivotal role in maintaining our overall health and well-being. The McCaig Institute is home to a multidisciplinary team of basic scientists, engineers, clinicians and health systems researchers from six faculties at the University of Calgary and four from the University of Alberta. These researchers have established high-level research programs to enhance the diagnosis, treatment and prevention of bone and joint conditions, in order to keep people moving. Much of the research is focused on osteoarthritis, rheumatoid arthritis and osteoporosis as these conditions pose some of the greatest threats to bone and joint health and rob people of their mobility and ability to live independently. The Institute is a pioneer in the multidisciplinary approach to tackling these critical conditions. Team members combine their diverse expertise to investigate questions related to all aspects of bone and joint health, from molecules to cells, to tissues, to joints, to patients, clinical populations and the way that healthcare is delivered.



**McCaig Institute**  
*for Bone and Joint Health*

Institute members were recently successful in an application to the Canada Foundation for Innovation, raising a total of over \$13 million to establish the Mobility and Joint Health Clinical Facility. This facility will create a unique capability in the province, to facilitate and accelerate the application of research findings into practice far more quickly than occurs currently (11 to 17 years). As shown in the figure, the McCaig Institute will be the research component of a triumvirate of units in the province related to bone and joint health. The clinical research facility completes the translation pipeline to enable the three units to work together seamlessly on bone and joint health issues. Members of the Strategic Clinical Network of Alberta Health Services will identify problems which need solutions: these will be conveyed to members of the McCaig Institute who will work together to formulate a solution – some problems will be short term and others involve much longer term research. The solution will be assessed by the independent Alberta Bone and Joint Health Institute, implemented by the network in a pilot fashion and assessed for efficacy, again by ABJHI. This will enable evidence-based best practice to be implemented across the network to the benefit of all Albertans.



## 15<sup>th</sup> Alberta Biomedical Engineering Conference

McCaig Institute, Gold Level Sponsor

AMIF, Silver Level Sponsor

Hotchkiss Brain Institute, Silver Level Sponsor

Institute of Engineering and Technology, Silver Level Sponsor

Libin Cardiovascular Institute, Silver Level Sponsor

Zymetrix, Silver Level Sponsor

APEGA, Bronze Level Sponsor

BOSE, Bronze Level Sponsor

Canadian Society for Biomechanics, Bronze Level Sponsor

NOTES:

NOTES:

## Force Enhancement; a Titin Achievement in Skeletal Muscle

Krysta Powers<sup>1</sup>, Gudrun Schappacher-Tilp<sup>2</sup>, Azim Jinha<sup>1</sup>, Tim Leonard<sup>1</sup> & Walter Herzog<sup>1</sup>

Human Performance Laboratory, Faculty of Kinesiology, University of Calgary<sup>1</sup>

Department for Mathematics and Scientific Computing, NAWI Graz, Karl-Franzens-University Graz<sup>2</sup>

[klpowers@ucalgary.ca](mailto:klpowers@ucalgary.ca)

### Introduction

A single theory is used to explain and predict force during shortening, lengthening and isometric muscle contractions. This theory predicts force by sarcomere length, or the number of attached cross-bridges (CBs) [1]. However, when an activate sarcomere is stretched, the actual force exceeds predicted force if CBs alone determine contractile force [2]. This property has been observed *in vivo* and down to single sarcomeres [3], prompting the development of alternative hypotheses to explain force during active stretch. It has been suggested that titin, a dynamic spring protein within the sarcomere, binds to the thin filament to increase force during active stretch (Fig. 1) [3]. In support of this hypothesis, recent observations from our laboratory show titin-based force enhancement (TFE) in actively stretched sarcomeres [3]. This study aims to determine whether TFE can be explained by titin binding to the thin filament

### Methods

Single mouse psoas myofibrils were actively stretched beyond filament overlap ( $\sim 6.0 \mu\text{m}$ ) where CBs cannot contribute to force. To determine the effect of  $\text{Ca}^{2+}$  and CBs on TFE, CB force was inhibited using previously validated methods [4]. The titin binding hypothesis was mathematically modeled and force was predicted for actively stretched sarcomeres in the absence and presence of titin binding [4].

### Results

Titin-based force increased 400% in actively stretched myofibrils. In the absence of CBs, TFE was nearly eliminated and titin force increased by only 15%, presumably due to  $\text{Ca}^{2+}$  stiffening of titin's springs [4]. TFE (300%) was predicted by the model when titin-thin filament binding was assumed during active stretch and was minimal in simulations with no binding (Fig. 2).

### Conclusions

In actively stretched sarcomeres, titin-based force is enhanced beyond any mechanism known to increase titin-based stiffness. This increase in force was nearly eliminated by preventing CB force. By assuming that titin binds to the thin filament during activation, predicted force coincided with experimental observations, while simulations performed in the absence of titin-thin filament binding coincided closely with CB-inhibited sarcomeres. Our results suggest that titin binds to the thin filament with the onset of CB cycling. This mechanism would provide the sarcomere with an additional source of force production during active stretch. With past and present studies demonstrating TFE in actively stretched sarcomeres, our understanding of contractile force should begin to expand to include the contribution of titin in actively stretched skeletal muscle.

### References

1. Huxley & Simmons (1971). *Nature*
2. Abbott & Aubert (1952). *J. Physiol.*
3. Leonard et al., (2010). *Am. J. Physiol. Cell Physiol.*
4. Powers et al., (2014). *J. Exp. Biol.*

### Figures

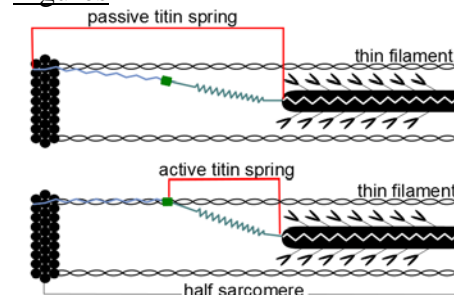


Fig. 1 Proposed mechanism of TFE

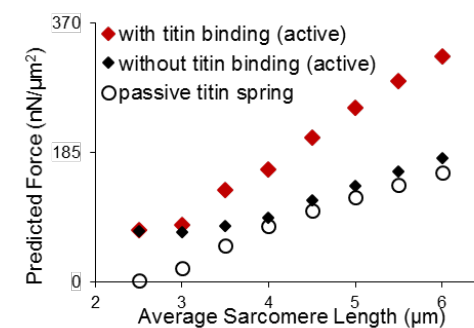


Fig. 2 Predicted sarcomere force

## Predicting the Impact of Surgery on Quality of Life and Risk Management in Patients Afflicted with Glioblastoma Multiforme

Luca Y. Li, David G. Gobbi, Jacob C. Easaw, Yves P. Starreveld

Biomedical Engineering, Clinical Neurosciences and Oncology, Hotchkiss Brain Institute, University of Calgary; and Seaman Family Centre, Calgary Image Processing and Analysis Centre (CIPAC), and Tom Baker Cancer Centre, Foothills Medical Centre, Calgary, Alberta

### Introduction

Glioblastoma multiforme (GBM) is a common malignant brain tumor with a fast rate of growth, representing 20% of brain tumors. Average survival time is 3 months if left untreated, 12-18 months with surgery and radiation and chemotherapy<sup>1</sup>. However, current treatments are not curative and GBM will typically relapse within six months, likely due to additional tumor tissue beyond the enhanced areas seen on contrast-enhanced magnetic resonance (MR) imaging requiring repeat treatment<sup>1</sup>. Present efforts focus on improving patient prognosis following an operation<sup>2</sup>. Recent evidence suggests a minimum of 78% tumor volume removal is sufficient to improve lifespan<sup>2,3,4</sup>. Current efforts aim to achieve 100% resection whenever possible, however, more aggressive surgery may harm the patient and these studies do not investigate impact on patient quality-of-life (QOL) afterwards<sup>4</sup>. This longitudinal study aims to evaluate at what percent resection the decrease in QOL outweighs the increase in life expectancy, and whether or not we can predict the outcome in order to help qualify for chemotherapy more frequently. We hypothesize that: 1) there is a threshold between 78% and 98% resection where survival time will continue to increase but functional performance score will start to decrease, 2) A lower tumor assessment scored based on anatomical location will reliably predict a lower post-operative functional score.

### Methods

Patients with GBM are selected from an ongoing study. MR imaging used a standard protocol for non-enhanced and contrast-enhanced T1 imaging. Pre/post-operative images for initial and follow up scans are then registered and used to measure change in tumor volume. Segmentation accuracy will be validated by manual measurements

done by a surgeon. Patient QOL will be represented by their pre/post-operative Karnofsky Performance Scale (KPS) score. Tumor assessment score will be calculated by deducting a point from 10 for each region of interest that has overlapping tumor tissue. A Spearman ranked correlation test will likely be used for statistical analysis.

### Results

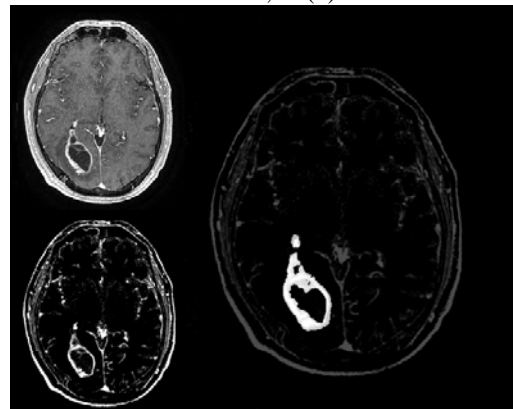
We anticipate an inflection point between 78% and 98% resection for KPS score to demonstrate more aggressive surgery may negatively impact the patient. We also expect to be able to predict post-operative KPS based on the tumors location and size on the MR image.

### Summary

This project aims to provide more quantitative data to address current gaps in knowledge concerning functional outcome following surgery, and systematic scoring of GBM lesions based on anatomical location. The results hope to provide better risk management in selecting a surgery that appropriately prioritizes lifespan vs. patient function, as well as establish anatomical location of tumor as a significant prognostic factor for survival time.

### References

1. Holland EC. PNAS 2000; 97(12): 6242-44
2. Dea *et al.* CJNS 2012; 39: 632-37
3. Bloch *et al.* JNS 2012; 117(6): 1032-38
4. Lacroix *et al.* JNS 2001; 95(2): 190-98



Isolated tumor tissue of a pre-operative patient for volume calculations using segmentation pipeline.

## Numerical analysis of LIPUS induced mechanical stresses in dentoalveolar structure using a three-dimensional finite element model

Mason Kim, Behzad Vafaeian, Tarek El-Bialy, Samer AdeeB  
Department of Civil Engineering, University of Alberta, Edmonton, Alberta

### Introduction

Orthodontically induced inflammatory root resorption (OIIRR) or simply root resorption, is the breakdown of root structure of a tooth due to orthodontic tooth movement. In previous studies, the stimulatory effects of Low intensity pulsed ultrasound (LIPUS) was reported to heal dental tissue, specifically root resorption. It has been suggested that the effect of LIPUS to enhance the healing of the tissues is power (dose) dependent, in which the power is related to the magnitude of mechanical stresses induced by the waves<sup>1,2</sup>. Computer simulation using the finite element analysis (FEA) was proposed to investigate the correlation between the ultrasound stimulatory effects and the magnitudes of mechanical stresses on the tooth root induced by LIPUS.

Previous studies using a two-dimensional (2D) model had limitations due to the simplification of the model as the 2D model lacks real situation<sup>3</sup>. The energy was trapped inside the model and the three-dimensional (3D) distribution of LIPUS induced stresses on the root surface could not be explored. In this study, a 3D model was introduced for more accurate simulation of LIPUS propagation through the dentoalveolar structure.

### Methods

Micro-CT scans of a dentoalveolar structure of a Beagle dog was used to reconstruct the geometry. The raw data was converted to a computerized model using software packages Mimics and Geomagic. The model consists of gingiva, alveolar bone, dentine, pulp and alveolar bone cavity. The FEA, solving the linear ultrasonic wave equation expressing the ultrasound propagation, was implemented by the software package Abaqus.

### Results

The FEA results of induced pressure on root surfaces were compared to the histological results of cementum thicknesses for both the LIPUS group and the control group. Correlations between the histological observation and FEA observation were found: (a) areas with the most cementum thickness increase had the highest pressure magnitudes, (b) areas with the least cementum thickness increase had the lowest pressure magnitudes, and (c) the mesial root had more cementum increase and more pressure magnitudes compared to the buccal root.

### Conclusions

This simulation demonstrates that dental tissues tend to regenerate when stimulated by mechanical stresses induced by LIPUS through correlating the histological observations with FEA observations. This approach of using FEA is a useful tool in revealing the correlation between LIPUS attenuation and its biological effect on dental tissue formation.

### References

[1] Al-Daghreer, S., et al. (2011). Archives of Oral Biology, 57(1). [2] El-Bialy, et al. (2004). American Journal of Orthodontics and Dentofacial Orthopedics, 126(2), 186-193. [3] Vafaeian, B., et al. (2012). 3rd International Structural Specialty Conference, 1031, 1-10.

### Figures

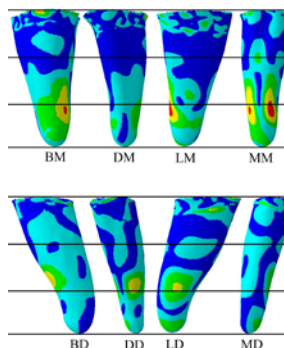


Figure 1. FEA results of LIPUS induced pressure

## **pQCT-based Indices of Bone Strength Under Axial and Combined Loading Differentiate Older Women With and Without Recent Distal Radial Fracture**

Christopher Bespflug<sup>1</sup>, James D. Johnston<sup>1</sup>, Cathy M. Arnold<sup>2</sup>, Geoff Johnston<sup>2</sup>, Saija A. Kontulainen<sup>3</sup>

<sup>1</sup> Mechanical Engineering Department, University of Saskatchewan, Saskatoon, SK, Canada

<sup>2</sup> College of Medicine, University of Saskatchewan, Saskatoon, SK, Canada

<sup>3</sup> College of Kinesiology, University of Saskatchewan, Saskatoon, SK, Canada

### Introduction

Distal radius fractures (DRF) are the most common osteoporotic fracture in women and an important predictor of other osteoporotic fractures [1]. A DRF occurs when the external forces applied to bone—usually due to fall—exceed the strength of bone (i.e., failure load). Peripheral quantitative computed tomography (pQCT) provides a potential tool for estimating DRF failure load via structural strength indices such as area (related to axial loading resistance) or area moment of inertia (related to bending resistance) [2]. Research to date has focused on axial-based indices of bone strength [3]. However, during a fall, the distal radius is subjected to a combination of axial compression and “off-axis” dorsal- and lateral-directed forces, which result in bending [4].

The objective of this study was to assess whether pQCT-based indices of bone strength under axial and off-axis loading scenarios could differentiate postmenopausal women with and without a recent distal radius fracture.

### Methods

We recruited 76 postmenopausal women (mean age 65, SD 8 years) from local clinics and through advertisement. Participants with a recent DRF (6-24 months post-fracture) (Fx, N=31) served as cases and age- and size-matched participants with no history of DRF (NonFx, N=45) as controls. We measured non-fractured wrist in cases and non-dominant wrist in controls.

We scanned distal radius (4% of radius length) using pQCT (Stratec XCT 2000). Images were analyzed using the pQCT Distribution Analysis plugin available through imageJ [5], defining bone with a threshold of 169mg/cm<sup>3</sup>. We did not use filters. The distal radius was modeled as a composite beam composed of cortical and trabecular bone. Trabecular and porous

cortical bone were converted to equivalent pure cortical bone using the equation  $BMD/1200$  [6], which normalized BMD in relation to BMD of pure cortical bone.

We derived the following strength indices using combinations of equivalent area and equivalent area moments of inertia specific to different loading conditions:

1. Axial compressive failure (vector: 0° dorsal inclination, 0° radial inclination).
2. Dorsally-directed off-axis loading resulting in dorsal compressive failure (21° dorsal inclination, 0° radial inclination).
3. Laterally-directed off-axis loading resulting in lateral compressive failure (0° dorsal inclination, 8.5° radial inclination).

The loading vector was assumed to originate at the 0% distal radius site and be aligned with the principal centroidal axes.

Differences in pQCT-based strength indices between the Fx and NonFx groups were compared using t-tests. Statistical significance was set at  $p < 0.05$ .

### Results

Pairwise comparisons showed that the group with DRF history in the past 24 months (Fx) had 9% lower strength index for axial loading ( $p=0.037$ ) and 9% lower index for laterally-directed off-axis loading ( $p=0.042$ ). The strength index corresponding with dorsally-direction off-axis loading did not differ between the groups ( $p=0.15$ ).

### Conclusions

Women with recent DRF had 9% lower resistance to axial loading and laterally directed off-axis loads. pQCT-based strength indices may help to improve the prediction of distal radius fracture risk in postmenopausal women.

### References

- [1] Cuddihy et al., 1999; [2] Kontulainen et al., 2008; [3] Pistoia et al., 2002; [4] Troy and Grabiner 2007; [5] Rantalainen et al., 2011; [6] pQCT Manual

## Intracellular uncoupling in cardiac tissue accelerates impulse propagation by activating more Purkinje-myocardial junctions

Elham Behradfar<sup>1</sup>, Anders Nygren<sup>1</sup>, Fu Siong Ng<sup>2</sup>, Edward J. Vigmond<sup>1,3</sup>

<sup>1</sup>Electrical & Computer Eng. Departemnt, University of Calgary, <sup>2</sup>Imperial College London, <sup>3</sup>Universite Bordeaux 1

### Introduction

The Purkinje system (PS) is the specialized conduction system of the ventricles, which contacts with ventricular myocytes and activates them through Purkinje-Myocardial Junctions (PMJs). There are limited data on number of PMJs, but it is known that a large portion of these junctions are not functional during normal rhythm [1]. We hypothesized that uncoupling in ventricular tissue facilitates propagation across PMJs, leading to more functional PMJs, and thereby accelerated activation of ventricles.

### Methods

The hypothesis was explored by performing experiments on perfused rabbit hearts [2] and computer simulation of uncoupling in the rabbit ventricular model [3]. The right ventricle of perfused hearts were dissected for optical mapping of right ventricle endocardium. Global ischemia was induced in hearts for 40 minutes followed by 30 minutes of reperfusion. In a detailed model of the rabbit ventricles and PS, simulations were performed with varying percentage of functional PMJs and varying tissue conduction.

### Results

In a simple model of ventricular tissue and PS, uncoupling was modeled by reduced conductivity. We found that after only 6% reduction in tissue conductivity, normally quiescent PMJs were capable of activating myocytes. In a detailed model of the rabbit ventricles and PS, simulations were performed with varying percentage of functional PMJs and varying tissue conduction. As figure 1A shows, increasing the number of active PMJs, accelerated propagation of activation over the surface and could compensate for the slowing of propagation due to reduced conductivity. Results of optical mapping of the endocardial surface revealed that the percentage of area with activation time less than 5ms increased during ischemia and returned to normal value after reperfusion (Figure 1B). We defined a parameter based on the divergence of

conduction velocity on the ventricular surface to quantify changes in the complexity of activation pattern. Divergence of velocity has large positive value at breakthrough site and large negative value at site of collision (Figure 2). The integral of absolute value of divergence over the endocardial area increased for higher percentage of functional PMJs and demonstrated occurrence of more breakthroughs and wave collisions.

### Conclusions

Our results indicate that a higher percentage of functional PMJs can speed activation of tissue and compensate for effects of uncoupling in terms of activation time of the ventricles. With more functional PMJs, propagation is more complex and integration of divergence of velocity can quantify these changes.

### References

- [1] Proc. Natl. Acad. Sci. U. S. A. 2005;102:4126–9.
- [2] Am. J. Physiol. Heart Circ. 2012; 303:753–65.
- [3] Hear. Rhythm. 2009;6: 1782–9.

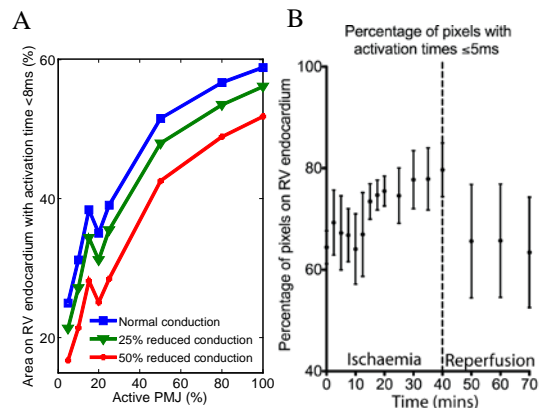


Figure 1: Variations in the activated area (A) in ventricular model (B) in perfused hearts

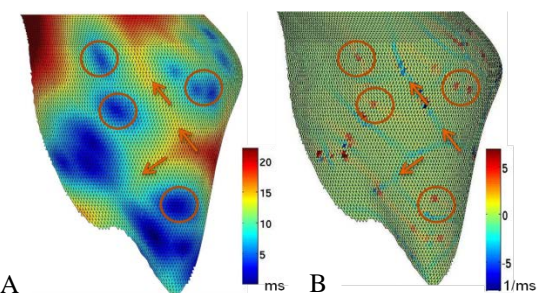


Figure 2: Sample of (A) activation time and (B) calculated divergence on the endocardial surface, with arrows pointing wave collisions and circles indicating breakthroughs.

## Biomechanical Control Conditions for Footwear Insole and Orthotic Research

Ryan T. Lewinson<sup>1,2,3</sup>, Jay T. Worobets<sup>1,4</sup>, Darren J. Stefanyshyn<sup>1,2</sup>

<sup>1</sup>Faculty of Kinesiology, <sup>2</sup>Schulich School of Engineering, <sup>3</sup>Faculty of Medicine, University of Calgary

### Introduction

Elevated peak knee abduction moments (KAMs) are implicated in joint conditions such as patellofemoral pain syndrome and medial knee osteoarthritis.<sup>1,2</sup> Commonly, footwear insoles or orthotics will be designed with a frontal plane wedge in attempt to reduce these KAMs;<sup>2</sup> however, the effect wedged insoles have on pain reduction is inconsistent across studies.<sup>3</sup> One possible explanation for this is that a wide variety of control conditions have been utilized, with the simplest method being to leave the participant's footwear unaltered from what the individual normally uses. While this approach leaves the individual's biomechanics unaltered, it does not control for any placebo effects that an experimental wedged insole/orthotic may induce. Consequently, flat insoles, standardized shoes across participants, or a combination of both have also been used as control conditions. While these strategies would control for placebo effects, it remains unknown whether these control conditions leave the individual's biomechanics – specifically the KAM – unaltered. Thus, the purpose of this study was to compare control conditions used in insole/orthotics studies to determine their influence on KAMs.

### Methods

Fifteen healthy individuals completed 5 gait analysis trials walking (1.6m/s) and 5 trials running (4m/s) with each of 4 footwear conditions (FCs) that are commonly used as placebo-control conditions in footwear insole/orthotics studies: (FC1) the participants own shoe (normal baseline biomechanics), (FC2) FC1 with a 3mm thick flat insole inserted beneath the sock liner, (FC3) a standardized running shoe (Adidas Mana), and (FC4) FC3 with a 3mm thick flat insole inserted beneath the sock liner. For each trial, 8 Motion Analysis cameras recorded the 3D trajectories of each participant's right lower extremity, and a force platform collected 3D ground reaction

force data. Kinetic and kinematic data were smoothed and a Newton-Euler inverse dynamics approach was used to calculate resultant peak KAMs for each trial.<sup>4,5</sup> The average value across trials within each FC and movement condition was then calculated and used in statistical analysis. Repeated measures ANOVAs were used to assess differences between FCs ( $\alpha=0.05$ ), and change in KAM relative to baseline (FC1) were plotted for each participant.

### Results

No significant differences in magnitude of the KAM were observed between footwear groups for both walking ( $p=0.78$ ) and running ( $p=0.59$ ). However, when examining participants individually, it was seen that, relative to baseline (FC1), a large proportion of participants experienced a change in KAM magnitude by more than  $\pm 10\%$  (40-87% of individuals depending on footwear and movement condition). This magnitude of change is similar to what wedged insoles specifically designed to alter KAMs would induce.<sup>5</sup>

### Conclusions

The proposed placebo-control conditions tested in this study are not effective control conditions. When evaluating the participant group as a whole, FC2-FC4 did not appear to induce a consistent directional influence on knee moment change; however, they did induce large, biomechanically relevant changes on an individual level. Thus, using these FCs as a placebo-control condition in footwear insole/orthotic studies does not seem warranted. Instead, it is recommended that the participant's own footwear be used as a control condition to ensure that the individual's normal gait is unaltered.

### References

1. Stefanyshyn et al. (2006). *Am. J. Sport. Med.*
2. Reeves & Bowling (2011). *Nat. Rev. Rheumatol.*
3. Parkes et al. (2013). *JAMA.*
4. Winter (2009). 4<sup>th</sup> ed., John Wiley & Sons press.
5. Lewinson et al. (2013). *Clin. J. Sport. Med.*

## Language Ability and White Matter Structure in Preschool Aged Children: A TBSS study.

Matthew Walton, Ashleigh Frayne, Deborah Dewey, Catherine Lebel,  
2888 Shaganappi Trail NW, Calgary AB, T3B 6A8

### Introduction

Early childhood is a period of rapid brain development, characterized by changes in cognition, emotion, and behavior. Between 2-4 years, typically developing children will undergo a massive growth of expressive and receptive language ability. Diffusion tensor imaging (DTI) is a specialized type of magnetic resonance imaging scan which allows for the in vivo assessment of brain white matter structure.<sup>1</sup> Parameters derived from DTI data include fractional anisotropy (FA), mean diffusivity (MD), radial diffusivity (RD), and axial diffusivity (AD). Improved white matter integrity is generally thought to be represented by increases in FA/AD and decreases in MD/RD.<sup>1</sup> Very few studies have investigated language ability and brain structure in children under the age of 5, though brain structure is known to correlate with language abilities in older children.<sup>2</sup> The goal of this study is to analyze the language aptitude of typically developing children aged 2.5-4.5 years and see if there is a relationship with white matter structure as shown through DTI measures. It is hoped this study will identify early brain markers of language ability, which could result in improved diagnosis and treatment of language impairments in young children.

### Methods

37 subjects (3.58y  $\pm$  0.39y, 23 Male) underwent language testing using the Phonological Processing subtest of the NEPSY-II and brain scanning on a GE 3T MR750w system (GE, Waukesha, WI) using a 32-channel head coil. DTI data was acquired using single shot spin echo echo-planar imaging with 30 diffusion encoding gradient directions at  $b=750\text{s/mm}^2$ , and 5 at  $b=0\text{ s/mm}^2$ . DTI data was quality checked, and underwent motion correction using in house, Matlab-based software, as well as eddy current correction, fitting of diffusion tensors, and tract based spatial statistics (TBSS) using FSL software.<sup>3</sup> TBSS projects

all subjects' diffusion data onto a mean white matter tract skeleton, before applying voxelwise cross-subject statistics.<sup>3</sup> Using a general linear model, standardized phonological processing scores were correlated with FA, MD, RD, and AD while controlling for gender.

### Results

TBSS analysis revealed MD to be negatively correlated with phonological processing scores within several white matter tracts in the left hemisphere ( $p=0.025$ ). These included the superior longitudinal, inferior fronto-occipital, uncinate, and arcuate fasciculi, as well as the anterior limb of the internal capsule. No significant results were found for FA, AD, or RD.

### Conclusions

These findings suggest that an important relationship exists between language ability and white matter brain structures in young children. Four out of five of the white matter tracts we found to be significant have also been shown to be correlated with language ability in older children and adults.<sup>4</sup> Decreased MD measures may represent a higher degree of myelination or greater axonal density in known language pathways. By identifying this structural-functional relationship at such a young age, we may be able to recognize earlier impairments in normal language function and begin to provide faster, more effective interventions.

### References

1. Le Bihan D., Mangin J.F., Poupon C. Diffusion tensor imaging: concepts and applications. 2001. *J Magn Reson Imaging*. 13, 534-54.
2. Hubertus A., Klinger C.M., Prescher A. Fibre anatomy of dorsal and ventral language systems. 2013. *Brain and Language*. 127, 192-204.
3. Smith S.M., Jenkinson M. Tract-based spatial statistics: voxelwise analysis of multi-subject diffusion data. 2006. *Neuroimage*. 15:31, 1487-1505.
4. Dick A., Tremblay P. Beyond the arcuate Fasciculus: consensus and controversy in the connectonal anatomy of language. 2012. *Brain*. 135, 3529-3550.

## Towards human intraspinal microstimulation implants: Mechanical stability and implications for lead-wire design

Amirali Toossi<sup>1</sup>, Austin Azar<sup>2</sup>, Dirk G. Everaert<sup>3</sup>, Christopher R. Dennison<sup>2</sup>, Vivian K. Mushahwar<sup>1,3</sup>  
 1Center for Neuroscience, 2Department of Mechanical Engineering and 3Division of Physical Medicine & Rehabilitation, University of Alberta

### Introduction

The overall goal of this study is to develop a mechanically stable design for chronically implanted intra-spinal electrodes. One of the most important functions lost after spinal cord injury (SCI) is the ability to stand and walk. Our lab has developed a novel electrical stimulation approach for restoring standing and walking, called intraspinal microstimulation (ISMS). This technique involves implantation of microwires in the spinal cord, targeting the neurons responsible for activating limb muscles. Low electrical currents (<0.1 mA) delivered through these electrodes produce coordinated movements of the legs [1]. Extensive testing in animals [2] demonstrated that the implant remains stable and functional chronically. These results suggest that ISMS may be a viable clinical approach for restoring leg movements in people with SCI. Implementation of ISMS in people requires certain design adjustments to accommodate human anatomy. Of utmost importance is the mechanical stability of the implant, which is largely determined by the behavior of the leads connecting the electrodes to the stimulator.

### Methods and Results

To determine the mechanical forces leading to electrode dislodgment, in-Fiber Bragg Grating (FBG) sensors were used [3]. These sensors are small (125µm in diameter) and light, and can be mounted in line with the microwires (50µm in diameter). The FBG sensors were calibrated using weights ranging from 0.1-200g. Initially, tofu and gelatin were used as surrogate models for the cord in bench-top testing. The electrodes were made of Pt/Ir (80% Pt) microwires with a 90° bend between electrode tip and lead wire. The 4.7 mm long electrode tip was implanted in the cord with the lead wire flush with the cord. Force was applied in-line with the lead wire. The average dislodgment forces were  $0.07 \pm 0.003\text{N}$  in tofu (10 trials) and  $0.032 \pm 0.003\text{N}$  in gelatin

(30 trials). The same procedure was applied to 3 freshly extracted pig spinal cords in which 18 trials were conducted. The average dislodgment force was  $0.028 \pm 0.019\text{N}$ . The dislodgment forces were also measured *in-situ* in the lumbar cord of a fresh pig carcass. The average measured forces were  $0.077 \pm 0.018\text{N}$  (5 trials). Elongation of the lumbar spinal cord under physiological movements was also measured in 3 fresh pig carcasses. Overall cord elongation during maximal spine flexion was  $8.1 \pm 1.8\text{mm}$ . In order to prevent the implant from dislodgment under these conditions, a strain relief mechanism such as a coil, is required to be able to extend with forces below the dislodgment thresholds. Therefore, coils with different parameters were characterized. Our preliminary results suggest that coils with wire diameter of 30 µm, coil diameter >300 µm and length >1cm fulfill the requirements.

### Conclusions

The forces that result in electrode dislodgment are minute, corresponding to a weight of 3 to 7 grams. The maximal elongation of the lumbar cord due to physiological movements was < 1 cm in pig carcasses. In order to prevent the implant from dislodgment under these conditions, the use of a coiled lead wire is proposed.

### Acknowledgements

This work was supported by NIH, CIHR, DoD-SCIRP, Vanier CGS, AIHS-sponsored Project SMART and NSERC.

### References

- [1] V. Mushahwar and K. Horch, "Muscle recruitment through electrical stimulation of the lumbo-sacral spinal cord," IEEE Trans. on Rehab. Eng., vol. 8, pp. 22-29, 2000.
- [2] V. Mushahwar, D. Collins, and A. Prochazka, "Spinal cord microstimulation generates functional limb movements in chronically implanted cats," Exp. Neurol., vol. 163, pp. 422- 429, 2000.
- [3] C. Dennison, P. Wild, D. Wilson, M. Gilbert, "An in-fiber Bragg grating sensor for contact force and stress measurements in articular joints", Meas. Sci. Technol. 21 115803, 2010.

## Knee pain is associated with osteophyte size

Ghazavi, N<sup>1</sup>; Bessflug, CJ<sup>1</sup>; Burnett, WD<sup>1</sup>; Kontulainen, SA<sup>1</sup>; McLennan, CE<sup>2</sup>;

Hazel, D<sup>2</sup>; Talmo, C<sup>2</sup>; Hunter, DJ<sup>3</sup>; Wilson, DR<sup>4</sup>; Johnston, JD<sup>1</sup>

1. University of Saskatchewan, Saskatoon, SK; 2. New England Baptist Hospital, Boston, MA;

3. University of Sydney, Sydney, NSW; 4. University of British Columbia, Vancouver, BC

### Introduction:

Osteoarthritis (OA) is a debilitating disease distinguished by changes in joint cartilage and subchondral bone. The source of pain is not well understood [1]. Osteophytes are bony outgrowths of cartilage at the margins of the joint, and one of the main features used to diagnose OA [2]. There is a disagreement about the relationship between pain and osteophytes with some evidence linking osteophytes to pain [3, 4], while others reporting no relationship [5-7]. This disagreement could be a result of limited osteophyte visualization, typically acquired using 2D x-ray imaging where osteophytes are only observed in one view (typically coronal). This issue could be solved using computed tomography (CT) to view osteophytes in coronal, transverse, and sagittal views, as well as at different image slices throughout the structure.

The objective of this study was to assess relationships between OA knee pain and osteophyte size, as viewed in serial CT images.

### Methods:

CT was used to scan the preoperative knee of 52 OA patients (23 men, 29 women, mean age  $64 \pm 9.4$  years). Pain was assessed using the Western Ontario and McMaster Universities Arthritis Index (WOMAC) [8]. A score between 0-5 was assigned to the pain experienced while walking, sitting, lying, at night in bed, up/down stairs, and standing. Total pain was defined as the sum of individual scores.

Using shareware software (MRIcro), serial CT images were reviewed to evaluate osteophyte size [9]. The size of an osteophyte was given a score of 0-5 at the lateral, central, and medial regions of the tibia and femur. Osteophytes were evaluated in coronal, sagittal, and transverse views with size scored at medial-lateral midpoints. Images were independently scored by two

readers (NG and CB). Final scores were agreed upon by consensus.

Relationships between individual and total WOMAC pain scores and regional osteophyte size were evaluated using Spearman's rank correlation coefficients (SPSS 21), with level of statistical significance of  $p < 0.05$ .

### Results:

Tibial lateral osteophyte size was positively associated with total WOMAC pain ( $r_s = 0.334$ ,  $p = 0.031$ ) and pain at night ( $r_s = 0.413$ ,  $p = 0.007$ ). Tibial central osteophyte size was positively associated with total WOMAC pain ( $r_s = 0.354$ ,  $p = 0.031$ ) and pain at night ( $r_s = 0.344$ ,  $p = 0.026$ ). Femoral central osteophyte size was positively associated with total WOMAC pain ( $r_s = 0.321$ ,  $p = 0.038$ ) and pain while standing ( $r_s = 0.375$ ,  $p = 0.015$ ).

### Conclusion:

Our findings suggest a relationship between OA knee pain and osteophyte size as measured by CT at the proximal tibia and distal femur. This study is the first to assess osteophyte size using serial CT images. This research may provide new targets for investigations to improve our understanding of the role of osteophytes in OA pain pathogenesis.

### References:

[1] Hunter, BMJ, 2006; [2] Altman, Arthr Rheum, 1986; [3] Cicuttini, Osteoarth Cartil, 1996; [4] Lanyon, Ann Rheum Dis, 1998; [5] Kornaat, Radiol, 2006; [6] Sengupta, Osteoarth Cartil, 2006; [7] Neogi, BMJ, 2009; [8] Bellamy, Rheum, 1988; [9] Rorden, Behavioural Neurology, 2000.

## Optimizing Tactor Parameters to Improve Discrimination for Sensory Feedback in Upper Limb Amputees

Katherine R. Evans<sup>1</sup>, Michael R. Dawson<sup>2</sup>, Dr. Jacqueline S. Hebert<sup>2,3</sup>, Dr. Jason P. Carey<sup>1</sup>

<sup>1</sup>Department of Mechanical Engineering, University of Alberta; <sup>2</sup>Glenrose Rehabilitation Hospital; <sup>3</sup>Faculty of Medicine, University of Alberta

### Introduction

Myoelectric prostheses use muscle signals from the residual limb or chest of an amputee to move the joints of the robotic limb, yet control is difficult as these prostheses lack sensory feedback [1]. Targeted reinnervation surgery relocates sensory nerves into skin on the residual limb or chest so that when touched, the patient feels as though they are being touched on their missing limb. Our group has shown that this restored hand map can be harnessed to provide feedback to the patient such that when they grip something with a prosthetic hand, a small object, termed *tactor*, pushes into their reinnervated skin, and they feel as if they are gripping the object directly [2]. This study aims to optimize tactor system parameters by investigating the ability to discriminate between the contacts of two tactors while maximizing comfort.

### Methods

The reduced profile horizontal tactor (Fig.1) is capable of providing up to 13 N of force at varying excursion distances, with a mass between 18 to 40 g, at a cost less than \$200. The tactor head and motor can be distanced from each other to conserve real estate on the residual limb. An investigation of tactor head optimization in terms of tactor head shape, size, and applied force was conducted with ethics approval. Five able-bodied and two transhumeral amputee participants were recruited. Participants were blindfolded with hearing occluded, and asked to report on two-point discrimination and comfort for each tactor combination. Monofilament sensation and clinical two-point discrimination were measured across trials. All measurements were repeated.

### Results

Results indicate that discrimination and comfort vary significantly between participants, at different locations, and over time. Normalizing data by these parameters

shows there is a significant difference in discrimination between tactor head shapes ( $p < 0.05$ ), where the domed head shape is optimal (Fig. 2). Size and force variables are not significant. None of the variables have a significant effect on comfort ( $p > 0.05$ ). Observation of the means plots indicates that further study into the optimization of tactor heads is warranted, as further significance may be achieved by increasing the sample size. Tactor discrimination is not significantly different from clinically measured discrimination ( $p > 0.05$ ), indicating that tactor placement can be determined in the clinic using existing tools.

### Conclusions

A cable driven tactor has been designed that is suitable for future amputee testing using functional tasks, where a domed head shape is optimal. This will lead to improved sensory feedback for upper limb amputees.

### References

[1] J.S. Schofield, et al. *Expert Rev. Med. Devices*. 2014. [2] J. S. Hebert, et al. *IEEE Trans. Neural Syst. Rehabil. Eng.* 2013.

### Figures

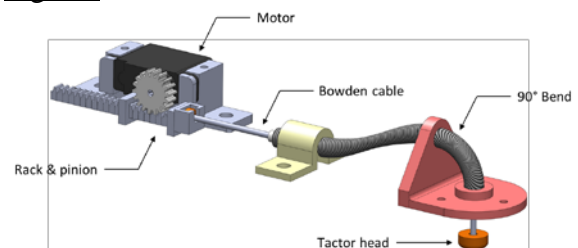


Fig. 1. Design of cable driven tactor

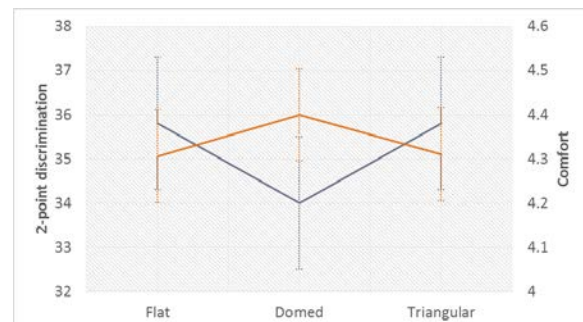


Fig. 2. Graph demonstrating that two-point discrimination and comfort vary by tactor head shape

## Persistent muscle weakness and contractile material loss in a clinically relevant Botulinum toxin type-A (BTX-A) injection protocol

Rafael Fortuna<sup>1</sup>, Andrew Sawatsky<sup>1</sup>, Marco Aurelio Vaz<sup>2</sup>, Walter Herzog<sup>1</sup>

Faculty of Kinesiology, University of Calgary, Calgary, Alberta, Canada

School of Physical Education, Federal University of Rio Grande do Sul, Porto Alegre, Brazil

Email: rfortuna@kin.ucalgary.ca

### Introduction

Botulinum toxin type-A (BTX-A) is a common therapeutic treatment to relax spastic muscles by preventing acetylcholine release at the motor nerve endings. Although considered safe and FDA approved, our previous studies have shown persistent muscle weakness and contractile material loss after BTX-A intervention using an aggressive injection protocol<sup>1</sup> that did not reflect clinical BTX-A treatment practice. The purpose of this study was to evaluate possible changes in muscle strength and contractile material in a clinically relevant BTX-A injection protocol. All experiments were performed using the quadriceps femoris musculature of New Zealand white (NZW) rabbits.

### Methods

Twenty-one ( $n=21$ ) NZW rabbits were divided into four groups as follow: Control saline injections ( $n=5$ ); Single BTX-A injection (1-BTX-A;  $n=6$ ); Two BTX-A injections (2-Botox;  $n=6$ ); and Three BTX-A injections (3-Botox;  $n=6$ ). BTX-A experimental group animals received an injection (3.5U/kg) unilaterally into the quadriceps femoris. Repeat injections were separated by a three months interval. Animals were evaluated six months after the last BTX-A injection. The primary outcome measures were knee extensor strength and the percentage of contractile material in the BTX-A injected muscles compared to the Control muscles. Muscle strength was assessed by measuring the maximal isometric knee extensor strength obtained by femoral nerve stimulation. The percentage of contractile material was determined histologically as the area fraction of contractile material relative to the total muscle cross-section area. A one-way ANOVA was performed at  $\alpha=0.05$ .

### Results

Six months following a single BTX-A injection, muscle strength (not shown) and contractile material (Fig. 1) were significantly reduced to 45% and 59%, respectively, when compared to Control group muscles. Interestingly, there was no additional loss in strength and contractile material in muscles receiving 2 or 3 repeat injections compared to muscles receiving a single injection.

### Conclusions

Our results suggest that muscle strength and contractile material do not fully recover within 6 months of a clinically relevant BTX-A injection protocol, suggesting that BTX-A has long lasting adverse effects which may compromise function. Furthermore, multiple injections have an increased treatment effect without additional adverse effects, thereby allowing for prolonged reduction of spasticity without penalty to the muscle.

### References

1 - Fortuna et al (2011). J. of Biomech **44**:39-44

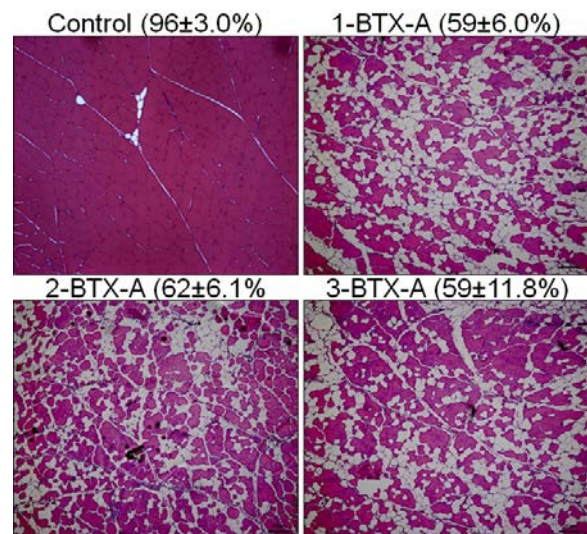


**Fig1.** Histological image showing the percentage of contractile material (H&E – red staining) and non-contractile material (white color – assume to be primarily fat and connective tissue).

**What is the bilateral asymmetry of radius and tibia bone microarchitecture by HR-pQCT?**Erin M. Hildebrandt<sup>1,2</sup>, Sarah L. Manske<sup>1,2</sup>, David A. Hanley<sup>2</sup>, Steven K. Boyd<sup>1,2</sup><sup>1</sup> Department of Radiology, Cumming School of Medicine, University of Calgary, Calgary, Alberta, Canada.<sup>2</sup> McCaig Institute for Bone and Joint Health, University of Calgary, Calgary, Alberta, Canada.Introduction

Asymmetry is well established in human long bones on a macro scale. For example, bone area by x-ray imaging has been shown to be significantly larger in dominant hands compared to non-dominant, presumably from an increase in mechanical loading.<sup>1-2</sup> Dual x-ray absorptiometry (DXA) and peripheral quantitative computed tomography (pQCT) imaging studies have found significantly higher bone macro architecture (including bone area (BA) and bone mineral content (BMC)) at the dominant forearm compared to the non-dominant.<sup>3-5</sup> Studies assessing bone health often select the dominant or non-dominant limb to scan, but not both, for efficiency reasons. In cases where fractures have occurred, the opposite limb is selected for scanning to avoid artifacts. The importance of selecting a dominant or non-dominant limb for relatively new 3D technology high-resolution pQCT (HR-pQCT) studies is not clear because little is known about dominance effects on bone microarchitecture. Using HR-pQCT, the aim of this study is to investigate the effect of limb dominance on bone microarchitecture.

Methods

Healthy participants (N=70) (average age 32.4 yrs, 43 women, 27 men) were recruited from Calgary and surrounding area and scanned at both radii and tibiae using HR-pQCT (XtremeCT, Scanco Medical). Dominance for hand and foot was determined by participant self-report. Scans were assessed using the manufacturer's standard protocol. Results were analyzed using a Two-Way ANOVA of sex and limb dominance effects.

Results

The majority of participants were right hand dominant (92.8%) and right foot dominant (94.3%). In the whole cohort, cortical area (Ct.Ar) was significantly greater at the

dominant radius (Ct.Ar, 2.99%, p=0.013). At the tibia, the dominant foot had significantly less Ct.Ar (-1.19%, p=0.028) and thickness (Ct.Th, -1.62%, p=0.021). For females, there were no differences at the radius, but at the tibia the dominant side had greater trabecular (Tb.Ar, 1.91%, p=0.010) and total area (Tt.Ar, 1.49%, p=0.008). At the radius, male's dominant side had greater Ct.Ar (6.52%, p=0.001), Ct.Th (6.49%, p=0.010) and total bone mineral density (Tt.BMD, 4.27%, p=0.032). Additionally, at the dominant tibia males had significantly greater trabecular thickness (Tb.Th, 3.43%, p=0.028) and less Ct.Ar (-2.52%, p=0.007), Ct.Th (-2.24%, p=0.042), and trabecular number (Th.N, -4.15% p=0.023).

Conclusions

Our data suggest that dominance has a small, yet significant effect on macro and microarchitecture at both the ultradistal radius and tibia. These data are similar to studies from DXA and pQCT demonstrating differences in BA, BMC and BMD for both total and cortical bone.<sup>3-5</sup> The dominance effect differed for males and females, which is potentially due to hormonal or growth patterns based on sex.<sup>6</sup> This work emphasizes that it is important to be consistent in the selection of either dominant or non-dominant limbs for HR-pQCT cohort studies, however in the case where the opposite limb needs to be scanned, it can be considered a suitable alternative. The differences detected were few, yet continued scanning of the non-dominant limb is a prudent approach, especially in cross-sectional studies.

References

1. Roy, et al. *Am J Phys Anthropol.* 1994 94:203.
2. Kazakia, et al. *Bone.* 2014 63:132.
3. Min, et al. *J Clin Dens* 2007 10:184.
4. Walters, et al. *J Clin Dens* 1998 1:359.
5. MacIntyre, et al. *J Clin Dens* 1999 2:413.
6. Kim, et al. *JBMR* 2003 18:150.

## Engineering Pseudoislets for Transplantation Applications

Milan Todorovic, Yang Yu, Mark Ungrin  
The Ungrin Lab, HMRB 322, Foothills Campus

### Introduction

Diabetes type I affects more than 300,000 [1] Canadians and can shorten life expectancy by up to 15 years [1]. The Edmonton protocol for islet transplantation is the current preferred treatment for achieving long-term exogenous insulin independence. However, only 15% of patients retain complete glucose homeostasis 5 years following the procedure [2]. This paper investigates means of improving the protocol's efficiency and efficacy through the use of novel tissue-engineered "pseudoislet" constructs.

### Methods

Native islets were dissociated using TrypLE and the obtained single cells were aggregated into pseudoislets at 400 cells/aggregate using AggreWell plates, a microwell-based forced-aggregation technology. Native islets were used as controls. The islets were cultured in CMRL1066 media at 37°C and 20% oxygen. Sample sizes ranged from n=3 to n=6 per condition based on available cell numbers. Statistical significance was evaluated using the t-test unless otherwise specified. Islet insulin secretion capacity was evaluated every 48 hours using glucose stimulated insulin secretion (GSIS) assays, with 2.5 mM and 16.7 mM glucose solutions simulating low (basal) and high (stimulated) glucose environments, respectively. Metabolic activity was tracked using the alamar blue (resazurin) fluorescent dye during basal glucose, while viability was calculated by analyzing the DNA content of lysed cell samples using PicoGreen at the end of each experiment and comparing it with that of samples set aside on day 0. FDA-PI live/dead staining imaging was also used to compare viabilities of pseudoislets relative to native islets.

### Results

FDA-PI live/dead staining images showed pseudoislet viability superiority compared to native islets as a result of altered shape and size. Resazurin assays showed a 3.5-fold increase ( $p=0.02$ ) in metabolic activity of pseudoislets aggregated after a 6-day longer native islet pre-incubation period. GSIS assays indicated a doubling in pseudoislet insulin secretion after the longer pre-incubation period as well, both at basal ( $p=0.013$ ) and stimulated ( $p=0.001$ ) condition. GSIS assays also showed highest insulin secretion at pseudoislet size of approximately 100 cells/aggregate ( $p<0.05$ , chi-square). Finally, GSIS assays of pseudoislets supplemented with the ROCK inhibitor Y-27632 showed up to a 6-fold increase in pseudoislet insulin secretion capacity relative to native islets ( $p<0.01$ ), while pseudoislets supplemented with both Y-27632 and one of the following: emricasan, fasudil, and ibuprofen, demonstrated similar insulin secretion capacities relative to those supplemented with only Y-27632 ( $p<0.05$ ).

### Conclusions

The goal of this research was to enhance the Edmonton protocol for islet transplantation by altering islet shape, size, pre-incubation time, and chemical composition. The obtained promising results validate the need for conducting additional research in order to ultimately develop a more efficient, effective, and affordable treatment for diabetes type I patients. Future directions might entail investigating the importance of ECM and altered islet composition on islet function and viability, followed by finding a way to shield the pseudoislets from the immune response.

### References

- 1 Canadian Diabetes Association, "An economic tsunami: the cost of diabetes in Canada," 2009.
2. Ryan, E. A. *et al.* Five-year follow-up after clinical islet transplantation. *Diabetes* 54, 2060–2069 (2005).

## Towards a New Severity Index for Assessment of Helmet Performance

Brooklynn Knowles<sup>1</sup>, James Newman<sup>2</sup>, Craig Good<sup>3</sup> and Christopher R. Dennison<sup>1</sup>

<sup>1</sup>Biomedical Instrumentation Lab, Department of Mechanical Engineering, University of Alberta; <sup>2</sup>Newman Biomechanical Engineering Consulting Inc., Edmonton AB; <sup>3</sup>Collision Analysis Ltd., Calgary AB

### Introduction

Worldwide, standards organizations that are concerned with certifying helmet performance are moving towards certification metrics that consider biomechanical measures of head injury risk. Current helmet standards assess a helmet's capacity to dissipate energy by dropping a helmeted headform onto a surface. The pass/fail metric, the metric used to convey impact severity, in most helmet standards (CSA, ASTM) is the peak acceleration at impact. However, since the 1960s, we have known that for a given head acceleration, increasing head velocity change over the impact leads to increasing risk of injury [1]. Methods established to compare acceleration-based injury assessment functions used in automotive testing for heads of differing mass, require scaling by cube root of mass ratio. There is currently no pass/fail criterion that incorporates all of these variables. Our objective is to investigate a new impact severity index, NSI, that scales severity based on headform mass using principles applied for other injury assessment functions while also scaling based on peak head acceleration ( $a_m$ ), and head velocity change ( $\Delta V$ ) [2]:

$$NSI = \left( \frac{m_h}{4.7} \right)^{1/3} \left( \frac{a_m \Delta V}{250V_i} \right) \leq 1.0$$

### Methods

In this preliminary work we simulated head impact using MADYMO multi-body dynamics software for a Hybrid III head-neck being struck by an impactor at 20 m/s and 22 m/s [3]. Angular velocity ( $\omega$ ) and linear ( $a$ ) and angular ( $\alpha$ ) acceleration were used to determine NSI and were input into the Simulated Injury Monitor (SIMon) brain FE model to compute tissue deformation thought to scale with injury risk (Cumulative Strain Damage Measure (CSDM)). Linear regressions were conducted for NSI, several kinematics, and CSDM to assess NSI's ability to scale with CSDM. We also performed impact experiments using

commercially available bike and hockey helmets and the UofA helmet test bed.

### Results

Table 1: Coefficients of Determination

$R^2$	CSDM	$\Delta V$
$a_m$	0.2029	-
$\Delta V$	0.4589	-
$\Delta\omega$	0.7746	0.5537
$a_m*\Delta V$	0.2832	-

Figure 1 shows: a) SIMon brain model showing deformation fringes; b) scatter plot of  $a_m*\Delta V$  and CSDM from SIMon; c) scatter plot of  $\Delta\omega$  and  $\Delta V$ .

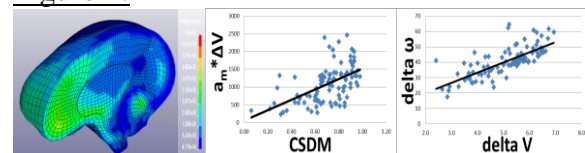
### Discussion and Conclusions

For NSI to be a useful pass/fail criterion,  $a_m*\Delta V$  must scale linearly with CSDM. As shown,  $a_m*\Delta V$  has moderate linearity with CSDM. The primary cause is poor linearity of  $a_m$  with CSDM. However, in recent work with impacts more similar to helmet drop tests than our simulations,  $\Delta\omega$  was found to scale linearly with  $a_m$  [4]. Work leading to other brain injury criteria has shown that  $\Delta\omega$  is the single best correlate to CSDM in head impact [5]. From our simulated results we found moderate linearity between  $\Delta\omega$  and  $\Delta V$ . These facts suggest that in our future work with more helmet-like impacts,  $a_m$  and  $\Delta V$  may both scale linearly with CSDM and as a result  $a_m*\Delta V$  and NSI. Future work will test this hypothesis. NSI could be the first pass/fail criterion uniting variables relevant to injury risk in a manner compatible with helmet certification tests.

### References

[1] Gurdjian et al., J. Trauma (1964); [2] Newman, ASTM F08-53 submission (2007); [3] Good et al., Proc. 20<sup>th</sup> Canadian Multidisciplinary Road Safety Conference (2010); [4] Ivarsson et al., J. Biomech. Eng. V.125 (2003); [5] Takhounts et al., STAPP V.57 (2013).

Figure 1:



a.

b.

c.

# AN APPROACH TO EXAMINE THE EFFECT OF TAPER ANGLE AND THREADING ON PERIPROSTHETIC BONE REMODELING FROM BONE-ANCHORED AMPUTATION PROSTHESES

Anita Fung<sup>1</sup> and W. Brent Edwards<sup>2</sup>

<sup>1</sup>Biomedical Engineering Program, University of Calgary, <sup>2</sup>Faculty of Kinesiology, University of Calgary

## Introduction

Recently, intraosseous transcutaneous amputation prostheses (ITAP) have been developed as an alternative to standard socket prostheses for amputees to bypass problems associated with the loading of soft tissue [1]. A current shortcoming of ITAP is the change in the local mechanical loading at the bone-implant interface leading to bone resorption. The clinical consequences of this bone loss are increased risks of bone fracture and implant loosening [2]. The purpose of this study was to develop a finite element modeling approach to examine the effect of ITAP fixture threading and taper angle on femoral bone remodeling.

## Methods

An intact femoral geometry was generated using Mimics software from CT scans obtained from the VAKHUM database [3]. Six threaded and six unthreaded ITAP implants of varying taper angles were designed using SolidWorks. Implants were registered and aligned within the femoral diaphysis, and the implant-femur assembly was meshed with quadratic tetrahedral elements; elements at the bone-implant interface shared identical nodes to represent full osseointegration. Bone elements were assigned inhomogeneous linear-elastic material properties based on CT Hounsfield units. Implant material was modeled as titanium alloy Ti6Al4V ( $E=114$  GPa,  $\nu=0.3$ ), which is commonly used for prostheses due to its superior strength and biocompatibility.

Boundary conditions and loads applied to the finite element models were taken from Tomaszewski et al. [4], which were linearly scaled to correspond to an individual with a mass of 70.1 kg and a height of 170 cm. All models were solved using ABAQUS Standard v6.1. Strain energy density was calculated for each implanted femur and compared to those of an intact femur.

## Results

Considerable energy was transferred to the ITAP (Figure 1). Consequently, the periprosthetic cortical bone in the implanted femur had a significantly lower strain energy density than that of the intact femur (Figure 1).

## Conclusions

It is critical that implant geometry is optimized to decrease periprosthetic bone resorption and reduce the incidence of bone fracture and implant loosening. Changes in strain energy density following prosthetic implantation is a driving stimulus for bone remodeling, and our future work will incorporate adaptive bone remodeling algorithms into our simulations. such as [5]:

$$\frac{dE}{dt} = C_e(U - U_n)$$

where  $E$  is the elastic modulus of the bone element,  $C_e$  is a constant that determines the rate of bone remodeling,  $U$  is the local strain energy density of the implanted femur, and  $U_n$  is the corresponding local strain energy density of the intact femur.

## References

- [1] Hagberg (2001). *Prosthet Orthot Int.* 25:186-94.
- [2] Xu (2008). *Ann Biomed Eng.* 36:435-43.
- [3] <http://www.ulb.ac.be//project/vakhum/>
- [4] Tomaszewski (2010). *Ann Biomed Eng.* 38:2418-27.
- [5] Huiskes (1987). *J Biomech.* 20:1135-50.

## Figures

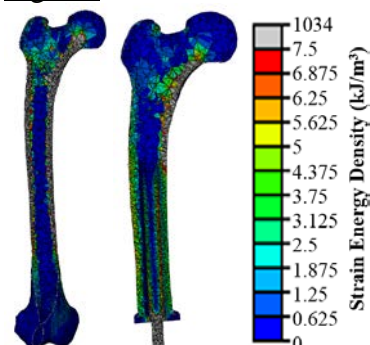


Figure 1: Strain energy density distribution of an intact femur (left), and of a femur implanted with a threaded, untapered fixture (right).

## History Dependence of EMG: Implications for Isometric Steady-State EMG Parameters Following a Lengthening or Shortening Contraction

Alexis Jones, Geoffrey A. Power, Walter Herzog  
Faculty of Kinesiology, Human Performance Laboratory, University of Calgary  
2500 University Dr. NW, Calgary, AB, Canada, T2N 1N4

### Introduction

Residual force enhancement (RFE) and residual force depression (RFD) refer to an increased or decreased force following active lengthening or shortening, respectively, relative to the isometric force produced at the same activation and muscle length [1]. Differing electromyographic (EMG) properties are observed during lengthening and shortening contractions compared to isometric [2]. Following active lengthening, EMG amplitude is reduced compared to a purely isometric reference contraction and active shortening leads to an increased EMG owing to higher motor unit discharge rates while force is depressed [3,4,5]. The altered sarcomere mechanics produced by the mechanisms underlying RFE and RFD may lead to divergent EMG amplitude and power spectral density than that shown in a purely isometric contraction. Our purpose was to determine whether specific EMG characteristics of lengthening or shortening contractions will be maintained in the isometric force enhanced or depressed state.

### Methods

EMG of the adductor pollicis was recorded at 0, 3 and 6s following active lengthening / shortening, and were compared with the purely isometric reference contractions at 40 and 100% of maximal voluntary force. Root mean square EMG amplitude ( $EMG_{RMS}$ ), median frequency (MF), and neuromuscular efficiency, defined as a ratio of normalized force/normalized  $EMG_{RMS}$ , were analyzed. A three-way (contraction type x contraction intensity x time) repeated measures ANOVA was performed. The level of significance was set at  $P \leq 0.05$ .

### Results

Normalized force was enhanced following lengthening (15, 6 and 9% at 0, 3 and 6s) ( $P < 0.001$ ) and was depressed by 19% at 0s

and 12% at both 3 and 6s after shortening ( $P < 0.001$ ).  $EMG_{RMS}$  and MF were not different for RFE, RFD and the isometric conditions ( $P > 0.05$ ). Neuromuscular efficiency was decreased for shortening ( $P < 0.05$ ), but did not show a significant difference following lengthening ( $P = 0.092$ ).

### Conclusions

Prior lengthening or shortening did not produce changes in the neuromuscular activation of the force enhanced or depressed state relative to an isometric contraction. RFD reduced neuromuscular efficiency, thus there may be implications for everyday human movement control.

### References

1. Abbott & Aubert. (1952). *J. Physiol.*
2. Duchateau et al., (2014). *J. Appl. Physiol.*
3. Garner et al., (2008). *J. Electro. Kinesiol.*
4. Rousanoglou et al., (2007). *J. Biomech.*
5. Oskouei et al., (2005). *J. Appl. Physiol.*

### Figure

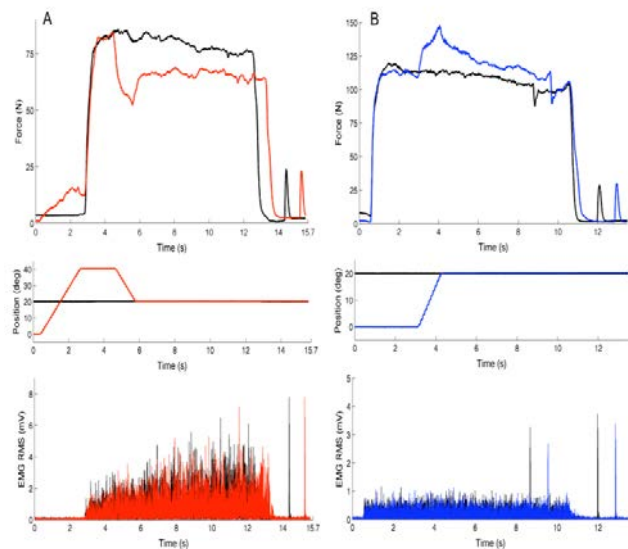


Figure 1. Typical force trace and EMG for a force depression (A.) and enhancement (B.) experiment. The black line represents the isometric reference contraction.

## **Knee pain is associated with osteophyte volume and bone mineral density**

Burnett, WD<sup>1</sup>; Bessflug, CJ<sup>1</sup>; Ghazavi, N<sup>1</sup>; Kontulainen, SA<sup>1</sup>; McLennan, CE<sup>2</sup>;

Hazel, D<sup>2</sup>; Talmo, C<sup>2</sup>; Hunter, DJ<sup>3</sup>; Wilson, DR<sup>4</sup>; Johnston, JD<sup>1</sup>

1. University of Saskatchewan, Saskatoon, SK; 2. New England Baptist Hospital, Boston, MA;

3. University of Sydney, Sydney, NSW; 4. University of British Columbia, Vancouver, BC

**Introduction:** Osteoarthritis (OA) is a painful debilitating joint disease marked by changes in cartilage and bony tissues surrounding the joint surface [1]. Osteophytes, or bony outgrowths along the joint margin, are one of the main radiographic features of OA [2]. Although osteophytes are one of the primary radiographic markers for diagnosing OA, studies reporting relationships between osteophytes and pain, the primary symptom of OA [1], are conflicting. Some studies show relationships between osteophytes and pain [3, 4] while others show no relationships [5-7]. These discrepancies may be due to limitations in 2D imaging techniques used to assess OA and osteophytes. As osteophytes are a 3D structure, it is possible to use 3D imaging tools, like computed tomography (CT), to quantify osteophyte size and composition. This information may aid our understanding of the role of osteophytes in OA progression and pain. The objective of this study was to explore associations between reported knee pain in patients with knee OA and CT-based osteophyte metrics, including volume and bone mineral density (BMD).

**Methods:** The preoperative knee of 52 patients scheduled for total knee replacement (23 men, 29 women, mean age  $64 \pm 9.4$  years) was scanned using quantitative CT (QCT), and participants were scored for pain using Western Ontario and McMaster Universities Arthritis Index (WOMAC) [8]. Serial CT-images of the tibia and femur were semi-automatically segmented using commercial software (Analyze 10.0, Mayo Foundation) to build two imaged volumes, one with and one without osteophytes. Osteophyte volume was obtained by subtracting the volume without osteophytes from the volume with osteophytes. We divided the tibia and the femur volumes into three equally spaced regions along the medial-lateral axis for

analysis of the medial, central, and lateral regions. Outcomes include total and regional osteophyte volume, and total and regional mean osteophyte BMD. Spearman's rank correlation was used to determine associations between WOMAC scores and regional osteophyte volume and BMD.

**Results:** Tibial lateral osteophyte volume was positively associated with total WOMAC pain ( $r_s=0.350$ ,  $p=0.023$ ) and pain at night ( $r_s=0.343$ ,  $p=0.026$ ). There were no significant associations between pain and femoral osteophyte volume.

Tibial medial osteophyte BMD was negatively associated with total WOMAC pain ( $r_s=-0.417$ ,  $p=0.007$ ) and pain at night ( $r_s=-0.358$ ,  $p=0.022$ ). Tibial central osteophyte BMD was associated with pain while going up/down stairs ( $r_s=0.401$ ,  $p=0.009$ ) and femoral lateral osteophyte BMD was negatively associated with pain while walking ( $r_s=-0.309$ ,  $p=0.047$ ). There were no significant associations between WOMAC scores and osteophyte BMD at other regions.

**Conclusions:** Tibial lateral osteophyte volume and tibial medial osteophyte BMD were related to knee pain, particularly pain at night. This was the first study to report tibial and femoral osteophyte volume and BMD and assess potential relationships with OA-related pain. This study provides new targets for studies to improve our understanding of the role of osteophytes in OA-related pain pathogenesis.

### References

- [1] Hunter, BMJ, 2006; [2] Altman, Arthr Rheum, 1986; [3] Cicuttini, Osteoarth Cartil, 1996; [4] Lanyon, Ann Rheum Dis, 1998; [5] Kornaat, Radiol, 2006; [6] Sengupta, Osteoarth Cartil, 2006; [7] Neogi, BMJ, 2009; [8] Bellamy, Rheum, 1988.

## **Functional near infrared spectroscopy: an inexpensive, non-invasive tool to assess brain functional connections in pediatric mild traumatic brain injury patients**

Laronna Sewell, Karolina J. Urban, Karen M. Barlow, Jon J. Jimenez, Bradley G. Goodyear, Jeff F. Dunn  
Experimental Imaging Center, Alberta Children's Hospital Research Institute, Hotchkiss Brain Institute, Faculty of Medicine, University of Calgary

### Introduction

Currently, severity of mild traumatic brain injury (mTBI) and recovery are assessed using coarse, subjective clinical scales. Cognitive impairment as a result of mTBI may be associated with reductions in the functional communication between brain regions. Functional connectivity assesses this communication by examining the synchronization of spontaneous activity between brain regions. Functional connectivity can be measured non-invasively using functional near infrared spectroscopy (fNIRS), which detects changes in oxy- and deoxy-hemoglobin (Hb) associated with brain activity. In comparison with fMRI, fNIRS is inexpensive and has greater temporal resolution. In this study, we hypothesized that functional connectivity is reduced in mTBI patients and is measurable using fNIRS.

### Methods

Seventeen mTBI patients (age  $15.4 \pm 1.5$  yrs, 8 males) and eight healthy controls (age  $14.0 \pm 0.8$  yrs, 5 males) participated in the study. The fNIRS unit (CW5, Techen, Inc.) consisted of 28 source-detector pairs embedded in a head cap, and utilized near infrared light at wavelengths of 690 and 830 nm. The head cap was placed over the motor cortex, and fNIRS was recorded as subjects performed a finger tapping task consisting of a five-minute resting state followed by five minutes of alternating periods of 30 seconds of tapping and 15 seconds of rest. Changes in oxy- and deoxy-Hb were calculated from absorbance values using HoMer software (1). For functional connectivity, the source-detector pair in the left hemisphere that exhibited the largest response to the tapping task was chosen as the reference seed for analysis. Coherence analysis, which assesses signal synchronization in the frequency domain, was performed between the reference seed and all other source-detector

pairs, over the range of 0.04-0.1Hz (2,3). Left hemisphere coherence was calculated as the average of coherence over the three source-detector pairs closest to the seed, and right hemisphere coherence was calculated as the average of coherence over the four source-detector pairs that matched the anatomical location of the left-hemisphere pairs (3). Comparison between the left and right hemispheres and participant groups was done using a two-way ANOVA, for each of the tapping and rest conditions.

### Results

There was no difference in the magnitude of activation during tapping between mTBI patients and control subjects, as measured by oxy-Hb. There was no difference in coherence between condition (tapping or rest) and hemisphere in controls. There was a reduction in coherence between hemispheres in mTBI patients using oxy-Hb during the resting state (left  $0.56 \pm 0.16$ , right  $0.33 \pm 0.26$ ,  $p < 0.01$ ) and task activation (left  $0.55 \pm 0.16$ , right  $0.30 \pm 0.24$ ,  $p < 0.01$ ). There was a reduction in coherence between hemispheres in mTBI patients using total-Hb during the resting state (left  $0.65 \pm 0.16$ , right  $0.37 \pm 0.27$ ,  $p < 0.05$ ) and task activation (left  $0.57 \pm 0.18$ , right  $0.38 \pm 0.21$ ,  $p < 0.05$ ).

### Conclusions

fNIRS successfully demonstrated there are significant reductions in functional connectivity between hemispheres associated with mTBI. fNIRS thus has the potential to become an objective measure of mTBI severity that can advise treatment and monitor recovery.

### References

- [1] Huppert TJ et al. (2009) Appl Opt 48: 280-298.
- [2] Franceschini MA et al. (2006) J Biomed Opt 11
- [3] Varshney VP et al. (2012) J. Europ. Opt. 7: 12047

## A Model-Based Approach to Diagnosis of Arterial Stenosis

Shiva Ebrahimi Nejad<sup>1</sup>, Karla Telidetzki<sup>2</sup>, Jin-Oh Hahn<sup>3</sup>, M. Sean McMurtry<sup>4</sup>, Jason Carey<sup>1</sup>

<sup>1</sup>: Department of Mechanical Engineering, University of Alberta, AB, Canada, <sup>2</sup>: Institute of Aerospace Studies, University of Toronto, ON, Canada, <sup>3</sup>: Department of Mechanical Engineering, University of Maryland, MD, USA, <sup>4</sup>: Department of Medicine, University of Alberta, AB, Canada.

### Introduction

Arterial stenosis is one of the most common arterial disease processes. Progression of arterial stenosis can be life-threatening, and its early detection and diagnosis can help patients to take appropriate treatment.

The most widely accepted low-cost test to detect peripheral arterial stenosis today is the ankle-brachial index (ABI). ABI is defined as the ratio between systolic pressure in the ankle and that in the brachial artery. ABI decreases as arterial stenosis in the lower extremity develops. Empirically, a value of 0.9 or less is diagnostic of arterial stenosis in the lower extremity<sup>1</sup>.

However, the reliability of this method has been questioned since in some cases (e.g., in case of simultaneous arterial stenosis and stiffening), the value of ABI is not sensitive to arterial stenosis<sup>2</sup>.

In this paper, a model-based approach to diagnosis of arterial stenosis is presented as a potential alternative to today's empirical way to detect arterial stenosis.

### Methods

The proposed model-based approach is based on the tube-load model, which is a mathematical model to describe blood pressure propagation in the arterial tree. The model is based on a few physical parameters, namely:  $\eta_1$ ,  $\eta_2$  and pulse transit time (PTT), each of which depends on peripheral resistance ( $R_T$ ), peripheral compliance ( $C_T$ ) and characteristic impedance ( $Z_C$ ) of the tube as shown below<sup>3</sup>.

$$\eta_1 = \frac{2Z_C + R_T}{2Z_C R_T C_T} \quad (1)$$

$$\eta_2 = \frac{R_T}{2Z_C R_T C_T} \quad (2)$$

The presence of arterial stenosis increases  $R_T$  and decreases  $C_T$ . However, the change in  $R_T$  due to arterial stenosis is not expected to be large since  $R_T$  is mainly attributed to arterioles. Thus, it was hypothesized from

(1) and (2) that  $\eta_1$  and  $\eta_2$  would increase with the progression of arterial stenosis.

To test these hypotheses, a high-fidelity arterial tree simulator was used to produce the arterial waveform data associated with varying degree of arterial stenosis, thereby collecting 60 simulated arterial stenosis of class B and C of TASC classification. Then, the data were fitted to the tube-load model to derive  $\eta_1$  and  $\eta_2$  for each of the simulated arterial stenosis. Finally, the trends of  $\eta_1$  and  $\eta_2$  with respect to severity of arterial stenosis were examined.

### Results

The results supported the hypothesis:  $\eta_1$  and  $\eta_2$  increased as the degree of arterial stenosis got severe (in terms of length, area and wall stiffness; see Figure 1).

### Conclusions

Across all the arterial stenosis simulated, ABI was bigger than 0.9 in only one case (thus not effective in detecting arterial stenosis). In contrast, the tube-load model parameters ( $\eta_1$  and  $\eta_2$ ) could not only detect all the arterial stenosis, but also responded proportionally to its severity (Figure 1).

### References

- [1]: CARTER, STEFAN A. "Indirect systolic pressures and pulse waves in arterial occlusive disease of the lower extremities." *Circulation* 37.4 (1968): 624-637.
- [2]: McLafferty, Robert B., et al. "Ability of ankle-brachial index to detect lower-extremity atherosclerotic disease progression." *Archives of Surgery* 132.8 (1997): 836-841.
- [3]: Rashedi, Mohammad, et al. "Comparative Study on Tube-Load Modeling of Arterial Hemodynamics in Humans." *Journal of biomechanical engineering* 135.3 (2013): 031005.

### Figures

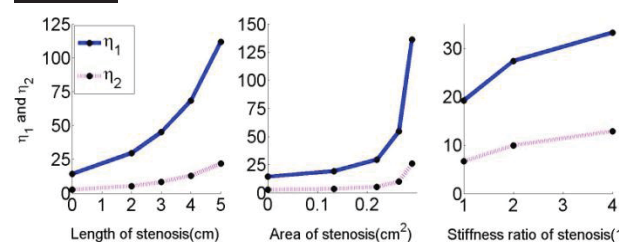


Figure 1: Effect of arterial stenosis on  $\eta_1$  and  $\eta_2$

## Distal Radius Strain Distributions during Off-Axis Loading

M.J. Adam<sup>1</sup>, M. Amini<sup>1</sup>, G. Johnston<sup>2</sup>, S.A. Kontulainen<sup>3</sup>, J.D. Johnston<sup>1</sup>

1. Division of Mechanical Engineering, University of Saskatchewan, Saskatoon, Canada

2. College of Medicine, University of Saskatchewan, Saskatoon, SK, Canada

3. College of Kinesiology, University of Saskatchewan, Saskatoon, Canada

### Introduction

Distal radius fractures (DRF) are the most common osteoporotic fracture in women and an important predictor of other osteoporotic fractures [1]. Bone fracture occurs when the external forces applied to bone—usually due to fall—exceed the strength of bone (i.e., failure load). Non-invasive imaging tools, such as peripheral quantitative computed tomography (pQCT), high resolution pQCT (HR-pQCT), and subject-specific finite element (FE) modeling provide useful means for estimating the strength of the distal radius. Research to date, however, has primarily modeled the distal radius as being in pure axial compression [2]. However, during a fall, the distal radius is subjected to a combination of axial compression and “off-axis” dorsal- and lateral-directed forces, which result in bending [3]. As well, palmar ligament forces and an offset contact point between the carpal bones and distal radius could result in further bending [4]. Though, since the contact location is located near the distal end of the radius, resulting bending moments may be small in relation to the axial force, rendering the axial compressive assumption valid.

Using mechanical testing representing a fall onto the outstretched hand, we aimed to characterize principal longitudinal strain at the palmar, dorsal and lateral sites, and fracture load of the distal radius.

### Methods

Three embalmed intact cadaver forearm specimens [min/median/max: 77/84/89 years] from 2 males and 1 female were acquired from the U of S College of Medicine. Mechanical testing was performed at 0°, 15°, 22.5°, and 30° of dorsal inclination and 3-6° of radial inclination. In 50N increments, the wrist was loaded up to 300N [5]. Tri-axial strain gauges measured strain at palmar, dorsal, and lateral surfaces during testing.

After strain data was gathered, the specimens were mounted at 15° of dorsal angulation and a smooth loading plate was compressed at 30mm/min onto the palm of the intact cadaver hand until failure was observed [2]. Force and strain data were gathered for each specimen.

### Results

On the palmar side, principal longitudinal strains were in tension. On the dorsal side, principal longitudinal strains were in compression. Strains appeared higher with increasing dorsal inclination. Absolute principal strains were ~67% higher on the dorsal (compression) side than the palmar (tension) side.

Specimens loaded until fracture resulted in two transverse fractures (822N & 375N) of the distal radius and one dislocation of the carpal bones. Distal radius fracture patterns were consistent with the classification of Colles' fracture: transverse metaphyseal region, 25-40mm proximal to carpal joint, dorsal angulation of fragment, and palmar tilt [6].

### Conclusions

The axial assumption did not appear valid when modeling the distal radius during a fall onto the outstretched hand. This finding was supported by observing lower palmar tensile strains than dorsal compression strains, as well as failure loads much lower than that observed with pure axial compression tests (1870-3410N) [7,8]. This research suggests that off-axis loading contributes to distal radius failure. Future pQCT, HR-pQCT and FE modeling approaches may benefit from modeling off-axis boundary conditions.

### References

- [1] Cuddihy et al., 1999, [2] Pistoia et al., 2002; [3] Troy and Garbinger 2007, [4] Wagner et al., 2012; [5] Edwards and Troy 2012; [6] Goldfarb et al., 2001; [7] Eckstein et al., 2002; [8] Lochmuller et al., 2002

## Is Skeletal Muscle Titin an Activatable Molecular Spring?

Jens Herzog<sup>1</sup>, Tim Leonard<sup>2</sup>, Azim Jinha<sup>2</sup>, Walter Herzog<sup>2</sup>

<sup>1</sup>Mount Allison University, <sup>2</sup>Human Performance Lab, University of Calgary

### Introduction

Titin is a viscoelastic spring protein that provides 95% of the passive force in single myofibrils (1). There is evidence that titin changes its mechanical properties when a muscle is activated. Specifically, titin is thought to bind calcium with muscle activation (3, 4) and attach to actin thereby increasing its spring stiffness by decreasing the stretched length (5). If this is the case, titin's contribution to force in an active muscle should be much greater than in a passive muscle. However, this has never been tested for dynamic muscle contractions. Therefore, the purpose of this study was to determine titin's force contribution to active and passive muscles. This was done by stretching active and passive single myofibrils to beyond actin-myosin filament overlap where titin is known to be the only contributor to force (1, 2).

### Methods

Rabbit psoas muscles were harvested, the connective tissue chemically digested, and individual myofibrils were mechanically separated (2). Myofibrils (n=11) were then mounted on a motorized glass lever that controlled myofibril length and a silicon nitrate lever that measured myofibril force. Myofibrils began at sarcomere lengths of 3.0 $\mu$ m and were stretched actively and passively to sarcomere lengths of ~4.5-5.0 $\mu$ m. Activated and passive myofibrils were then subjected to ten shortening-stretch cycles of 0.5 $\mu$ m/sarcomere, and then returned to their starting length. All stretches were performed at a speed of 0.1 $\mu$ m/sarcomere/second.

### Results

Actively stretched myofibrils (Figure 1, label A) had much greater force contributed by titin (compare forces at sarcomere lengths greater than 4.0 $\mu$ m) than passively stretched myofibrils (Figure 1, label B). Active myofibrils had greater hysteresis and

greater reductions in peak forces (Figure 1, label 2) during the ten shortening-stretch cycles compared to the passive myofibrils (Figure 1, label 3). The exemplar results shown in figure 1 for single actively and passively stretched myofibrils were the same for all myofibrils tested in this study.

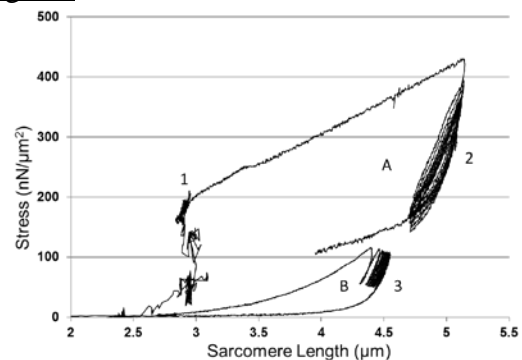
### Conclusions

The dramatically increased forces in the region beyond actin-myosin filament overlap (sarcomere lengths >4.0 $\mu$ m) in the activated compared to the passive myofibrils is exclusively attributable to titin. This result unequivocally indicates that titin is "activated" in some unknown manner during muscle contraction, thereby vastly increasing its force contribution in active compared to passive muscle. The increased hysteresis and peak force reduction during the repeat shortening-stretch cycles suggest that this activation is associated with an engagement of titin's Ig domains in the active myofibrils. The molecular details of this newly found dynamic "activation" of titin requires further study to uncover the molecular details of titin's force regulation upon muscle activation.

### References

1. M. S. Z. Kellermayer, et al., Science 276, 1112 (1997).
2. J. A. Herzog, et al., J. Biomech. 45, 1893 (2012).
3. Labeit D, et al., PNAS 100:13716-13721 (2003).
4. Joumaa V, et al., Am J Physiol 294:C74-C78 (2008).
5. Herzog W. J Appl Physiol 116:1407-17 (2014).

### Figures



## Providing Kinesthetic Sensory Feedback in Upper Limb Prostheses

Schofield J.S, Hebert J.S, Carey J.P

6-23 MecE Building, University of Alberta, Edmonton AB. T6G 2G8 (jsschofi@ualberta.ca)

### Introduction

Dexterous hand movement is dependent on efferent motor output and afferent sensory feedback. This is drastically altered in those with upper limb (UL) amputation as sensations of touch and movement are inherently lost. This absence impedes prosthetic control by forcing reliance on vision and increasing the required attention. Approximately 25% of UL prosthetic users reject their device and lack of sensory feedback is often identified as a major factor<sup>1</sup>. A unique approach to address this challenge is targeted reinnervation (TR) surgery, which reroutes residual nerves which once innervated a patient's amputated limb to chest or residual limb muscles. This restores sensation in the missing limb and aids in intuitive control of prostheses<sup>2</sup>. While literature reports return of cutaneous sensations<sup>3</sup>, movement (kinesthetic) sensibility has yet to be investigated.

This work explores the kinesthetic illusion in TR amputee subjects as a mechanism to restore kinesthetic sensation and establish feedback from the prosthesis to the user.

### Methods

Four unilateral, above elbow amputees who have undergone TR surgery were recruited. Our approach exploited the kinesthetic illusion; a phenomenon whereby vibration of musculotendinous regions of a limb induces sensations of limb movement<sup>4</sup>. It was hypothesized that strategic vibration of our participants' reinnervated muscle groups would induce sensations of hand movement in their missing limbs.

Initial vibration of the reinnervated muscle groups was performed to identify locations most consistently eliciting strong hand movement illusions. If a location was identified, varying combinations of vibration amplitude and frequency were systematically introduced. These tests were aimed to quantify the effect of altering vibration parameters on kinesthetic illusions. Participants reported on the strength of illusion and movement sensations.

Limb matching experiments demonstrated the use of the kinesthetic illusion in a prosthetic system. A prosthetic hand was linked to the vibration system such that when the prosthesis actuated, vibration was introduced to the reinnervated muscle in time with the prosthetic movement (Fig. 1). The participant was asked to pantomime sensations of movement with their intact side, and movements were recorded.

### Results

With vibration of reinnervated muscles, all 4 participants were able to experience hand close sensations and 2 participants reported hand open sensations in their missing limb. Vibration feedback at 90 Hz frequency and 0.5 mm amplitude most consistently elicited the strongest sensations of hand movements.

Results from the limb matching experiments suggest that participants were able to accurately interpret the kinesthetic illusion and these sensations could be readily matched to prosthetic movement.

### Conclusions

This work presents encouraging data suggesting a method to access kinesthetic sensations in an amputee's missing limb for use in communicating prosthetic movement. Follow up work is currently underway to develop systems capable of being incorporated in functional prostheses for evaluation of clinical and long term utility.

### References

- [1] Biddiss E, et al. Disabil Rehabil Assist Technol. 2007 [2] Hebert JS, et al. Crnt Srg Rprts 2014 [3] Kuiken TA, et al. Proc Natl Acad Sci. 2007 [4] Goodwin GM, et al.. Brain. 1972

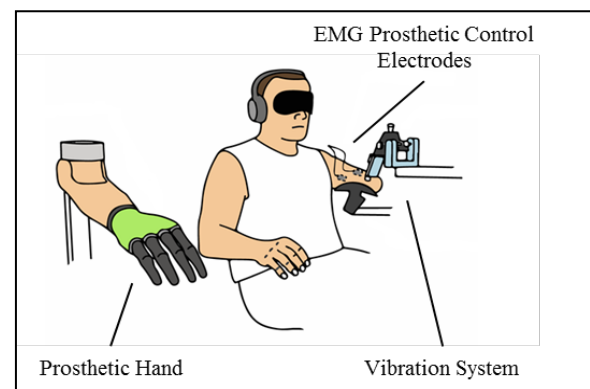


**Fig. 1** Limb matching experimental setup

## EEG Activity of the Cerebral Cortex during Rhythmic Lower Limb Movements

Hendrik Enders, Filomeno Cortese, Andrea B. Protzner, Benno M. Nigg

Human Performance Laboratory, University of Calgary, 2500 University Drive NW, Calgary AB, T2N 1N4

### Introduction

Coordinated movement is a complex process required for daily living, work and personal enjoyment. For individuals suffering from neurological disorders, coordinated movement can be difficult if not impossible. Prosthetics and neuro-rehabilitation devices have been developed in order to improve movement for those with disability. It is critical to understand how a healthy brain functions during exercise in order to develop a device that can mimic healthy human movement. However, real-time brain activity during movement has rarely been assessed due to the difficulty of collecting noise-free data during dynamic tasks. Recent advances in hardware and software now allow researchers to image the brain in real time during dynamic situations [1]. Therefore, the purpose of this study was to investigate the time-frequency patterns of electrical brain activity during rhythmic movements in healthy individuals.

### Methods

Ten healthy individuals were cycling at a constant intensity while real-time cortical activity was recorded using a 64-channel electroencephalography (EEG). Independent component analysis (ICA) was used to remove eye artifacts and non-cortical noise components [2]. Source analysis was performed to locate the origin of neural activity in brain space [3]. We used a k-means clustering algorithm to group the identified sources of neural activity across subjects. Time-frequency patterns of cortical activity were visualized as event-related spectral perturbations (ERSP) in order to quantify the oscillatory behavior of neural sources located in 3D brain space. Cluster-based permutation statistics were used to test if the ERSP data showed significant spectral perturbations from baseline ( $P < 0.05$ ).

### Results

Neural sources were spatially localized to Brodmann area (BA) 9 (left and right frontal

cortex), BA 4 (primary motor cortex), BA 6 (Premotor cortex) and BA 31 (posterior cingulate cortex) (Figure 1). The ERSP showed significant changes in spectral power across the pedaling cycle with the strongest activity being present in the premotor cortex cluster, followed by activity in the frontal lobe and the primary motor cortex. The temporal evolution of neural activity was initiated in the frontal cortex and followed by activity in the premotor and primary motor areas.

### Conclusions

To the best of our knowledge this is the first study reporting intra-trial fluctuations of brain activity localized to specific cortical areas during cycling. Based on our results we suggest a cortical network model of cycling that includes executive brain centers (frontal cortex), the premotor area for movement planning and the primary motor area for descending motor commands and integration of sensory afferent feedback. Providing this knowledge to engineers and medical professionals is critical for improved prosthetics, neuro-rehabilitation devices and treatment strategies.

### References

- [1] Gramann, K., et al. *Rev Neurosci*, 2011.
- [2] Jung TP., et al. *Psychophysiology* 2000.
- [3] Gwin J., et al. *Neuroimage* 2011.

### Figures

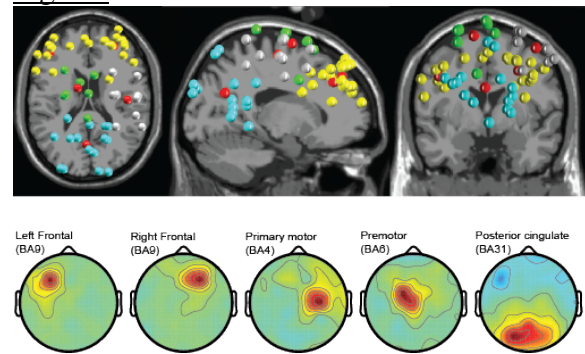


Figure 1: Clusters of neural sources localized in 3D brain space (top) and corresponding topographical scalp projections (bottom).

## Cartilage Boundary Lubricating Ability of PRG4 (Lubricin) Monomers And Multimers With Hyaluronan

Janna Haladuck<sup>1</sup>, Saleem Abubacker<sup>2</sup>, Tannin Schmidt<sup>1,2,3</sup>

<sup>1</sup>Faculty of Kinesiology, <sup>2</sup>Biomedical Engineering Graduate Program, <sup>3</sup>Schulich School of Engineering University of Calgary

### Introduction

Proteoglycan 4 (PRG4), or lubricin, is a glycoprotein that exists in synovial fluid (SF) as monomeric and disulfide-bonded multimeric forms [1,2]. PRG4 functions as a critical boundary lubricant on the surface of articular cartilage [1,3]. Hyaluronan (HA) is another lubricant that lubricates at a cartilage-cartilage interface alone, and synergistically with PRG4 to reduce friction levels near that of SF [4]. Previously PRG4-multimers (PRG4-multi) have been shown to lubricate considerably better than PRG4 monomers (PRG4-mono) in an *in vitro* model [5]. However, it is unknown if the difference in structure of PRG4-multi/-mono affects the synergism with HA. Therefore, the objective of this study was to evaluate the cartilage boundary lubricating ability of PRG4-multi & PRG4-mono with HA.

### Methods

PRG4 was purified from media conditioned by mature bovine cartilage explants [4]. PRG4 multi/mono was prepared via size exclusion chromatography [5].

Lubricants of interest were assessed using an *in vitro* cartilage-cartilage friction test [6]. Briefly, bovine osteochondral samples (n=8) were incubated with test lubricants overnight, compressed, allowed to stress relax then rotated at an effective velocity of 0.3 mm/s with pre-sliding durations (Tps) of 1200, 120, 12, and 1.2s. Phosphate buffered saline (PBS) and bovine SF served as negative and positive controls, respectively. All samples were prepared at a physiological concentration [4]; PRG4 at 450 µg/mL and HA (1.5 MDa, Lifecore Biomedical) at 3.33 mg/mL, in PBS. *Test sequence*: PBS, PRG4-mono+HA, PRG4-multi+HA, PRG4 (unseparated)+HA, SF.

Static ( $\mu_{\text{static,Neq}}$ ) and kinetic ( $\langle\mu_{\text{kinetic,Neq}}\rangle$ ) friction coefficients were calculated [4,6]. ANOVA was used to assess the effect of lubricant and Tps, as a repeated factor, on

$\mu_{\text{static,Neq}}$  and  $\langle\mu_{\text{kinetic,Neq}}\rangle$ , with Tukey post-hoc on  $\langle\mu_{\text{kinetic,Neq}}\rangle$  at Tps=1.2s (as values were similar to Tps=1200s; 13.0±2.7%).

### Results

PRG4-mono/-multi+HA, functioned as effective friction-reducing cartilage boundary lubricants. However, they did not lubricate as well as PRG4+HA or SF.  $\mu_{\text{static,Neq}}$  values increased with Tps; highest in PBS and lowest in SF, with PRG4-mono/-multi+HA, and PRG4+HA, being intermediate (**Fig.1A**).  $\langle\mu_{\text{kinetic,Neq}}\rangle$  values for PRG4-mono+HA and PRG4-multi+HA were similar (p=0.96). PRG4+HA and SF were similar (p=0.53). All other combinations were significantly different from each other (p<0.05) (**Fig. 1B**).

### Conclusions

Previous studies have shown that PRG4-multi lubricates better than PRG4-mono [5]. However these results show that PRG4-mono/-multi with HA lubricate in a similar manner. Interestingly, PRG4+HA lubricates better than PRG4-mono/-multi+HA, and close to that of SF. These differences could be due to a potential PRG4+HA “link molecule” [7] being purified from the PRG4-mono/-multi preparation.

### References

<sup>1</sup>Swann+ JBC'81, <sup>2</sup>Schmidt+ BBA'09, <sup>3</sup>Jay+ Curr Opin Ortho'04, <sup>4</sup>Schmidt+ A&R'07, <sup>5</sup>Abubacker+ Trans ORS'13, <sup>6</sup>Schmidt+ OAC'07, <sup>7</sup>Flannery+ Trans ORS'10

### Figures

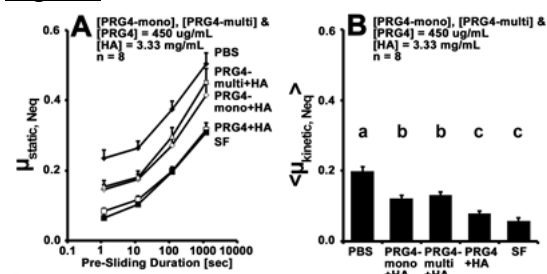


Figure 1:  $\mu_{\text{static,Neq}}$  (A) and  $\langle\mu_{\text{kinetic,Neq}}\rangle$  (B) for PBS, PRG4-multi+HA, PRG4-mono+HA, PRG4+HA, and SF (n=8). Mean±SEM. Different letters represent significance (p<0.05).

## Getting More From Image Data: pyCellAnalyst, a 3-D Image Reconstruction and Deformation Analysis Tool

Scott C. Sibole, Azim Jinha, Salvatore Federico, Walter Herzog  
Human Performance Laboratory, University of Calgary, Calgary Alberta

### Introduction

Advancements in three-dimensional (3-D) imaging modalities have greatly enhanced the observational scope of many areas of science. These 3-D images are extremely rich in data, albeit often difficult to quantify. For the case of cartilage, confocal laser scanning microscopy provides a means to visualize microstructures such as cells or collagen fibres in the intact tissue. By obtaining microscopy images both when the tissue is at rest and deformed, the resulting microstructural deformation can be determined.<sup>1</sup>

For chondrocytes, the sole cell type in cartilage, traditional analysis techniques approximate the cells as ellipsoids and consider measurements that do not fully characterize the deformation, such as volume change or change in the ellipsoid approximation's width, depth, and height.<sup>1</sup> Therefore, the objective of this work is to provide a new tool capable of operating on the non-simplified cellular geometries and returning the complete strain tensor describing the cells' deformation.

### Methods

A software framework, pyCellAnalyst, was developed in the Python programming language employing the popular C++ libraries, *Visual Toolkit (VTK)* and *Insight Toolkit (ITK)* (Kitware, Inc.). pyCellAnalyst, can be imported into any Python script, where it can be used alongside other modules, allowing for high extensibility.

For reconstruction of chondrocyte geometries, an *ITK* level set segmentation algorithm was employed.<sup>2</sup> Once cells have been reconstructed in a reference and deformed configuration, deformation analysis can be performed on the geometries. By determining the affine transformation that best maps the reference geometry to the deformed geometry, the full Green-Lagrange strain tensor can be determined, with the assumption of uniform deformation. An

iterative optimization algorithm included in *VTK* is used to determine this transformation.

### Results

pyCellAnalyst was capable of reconstructing cellular geometries from image data. The code was verified using a data set containing reference and deformed geometries in which the applied deformations were known. It was able to nearly exactly calculate these known strains. Likewise, it was capable of calculating the cellular strains from experimental data (Figure 1).

### Conclusions

A software framework to reconstruct geometries of chondrocytes from 3-D microscopy data, and analyse the deformation of these structures has been developed. While previous analysis methods have reduced the cellular geometries to ellipsoids, this software operates on the reconstructed shapes without any additional simplification. Furthermore, the full Green-Lagrange strain tensor is calculated providing, for the first time, a more complete description of the deformation, including all normal and shear strains. The software is open source and hosted at [github.com/siboles/pyCellAnalyst](https://github.com/siboles/pyCellAnalyst).

### References

1. Madden et al. *J Biomech*. 2013.
2. Mosaliganti et al. *Insight Journal*. 2009.

### Figures

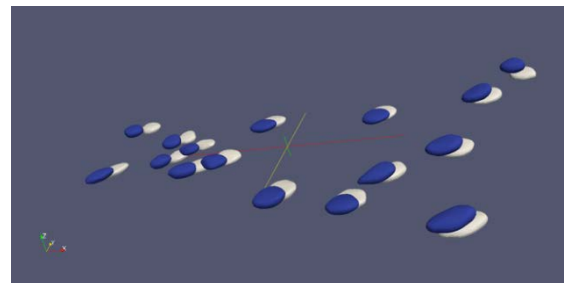


**Figure 1:** pyCellAnalyst can calculate the Green-Lagrange strain tensor from cells reconstructed in the reference (blue) and deformed (white) configurations.

## High Motor Unit Synchronization between Vastii Muscles during Dynamic Movements

Maurice Mohr<sup>1</sup>, Marius Nann<sup>2</sup>, Vincent von Tscharnner<sup>1</sup>, Benno M. Nigg<sup>1</sup>

<sup>1</sup>Human Performance Lab, University of Calgary, <sup>2</sup>University of Erlangen-Nuremberg  
mmaurice@ucalgary.ca

### Introduction

Motor unit (MU) synchronization between individual quadriceps muscles, as a result of a common excitatory motor input has generally been investigated and identified for isometric contractions [1]. It has been suggested that MU synchronization between knee extensors has implications for dynamic control and healthy loading of the knee joint [2]. However, in order to derive functional interpretations, intermuscular MU synchronization must be investigated during more natural, dynamic movements. Therefore, the purpose of this study was to compare the synchronization of MUs between two quadriceps muscles during isometric and dynamic squats. We hypothesized that the increasing complexity of a dynamic movement demands a higher degree of MU synchronization.

### Methods

Healthy, male and female subjects (n=9; 25±4 years) completed an isometric squat and a series of dynamic squats. A recently developed current amplifier [3] was used to record monopolar surface electromyograms (EMGs) from the *vastus lateralis* (VL) and *medialis* (VM). As a measure of synchronization, coherence spectra between the raw EMGs of VL and VM were calculated between 15–100 Hz and averaged across subjects. For comparison, random coherence spectra between two similar but unrelated signals were computed. Statistical differences between coherence spectra were determined using a one-way repeated measures ANOVA and Bonferroni corrected post-hoc tests ( $\alpha=0.05$ ).

### Results

Mean coherence between VL and VM was significantly higher for dynamic squats compared to isometric squats ( $p=0.006$ ) with

a distinct peak at frequencies between 35–45Hz. Coherence for both the dynamic and isometric squats was significantly higher ( $p<0.001$ ) than coherence of unrelated signals (Fig. 1).

### Conclusions

The significant increase in coherence for dynamic squats compared to isometric squats suggests a higher degree of MU synchronization between VL and VM. In particular, the distinct increase in MU synchronization at 40 Hz might reflect the enhancement of a common rhythmic excitatory input originating from the motor cortex at frequencies between 30 – 60 Hz [4]. An enhanced common and rhythmic MU input across synergistic quadriceps muscles might represent a basic strategy of the central nervous system to execute and control complex, dynamic knee movements. The results of this study underline the importance of investigating MU synchronization during dynamic movements rather than isometric contractions. Future research has to further elaborate implications of common rhythmic quadriceps activation for healthy knee joint loading.

### References

- 1 Boonstra et al. (2008). *J. Electromyogr Kines.*
- 2 Mellor & Hodges (2005). *J Pain.*
- 3 Von Tscharnner et al. (2013). *J Electromyogr Kines.*
- 4 Brown (2000). *Prog. Neurobiol.*

### Figures

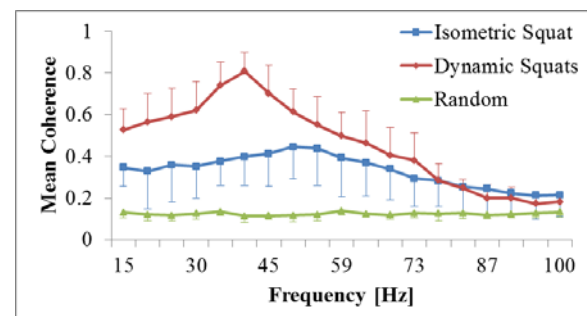


Figure 1: Coherence spectra (mean±SD, n=9)

## Identifying the loading threshold conducive to irreversible muscle damage in deep tissue injury.

Leandro R Solis, Vincent Tan, Vivian K Mushahwar.

Division of Physical Medicine and Rehabilitation, Faculty of Medicine and Dentistry. University of Alberta

### Introduction

Deep tissue injury is a type of pressure ulcer that commonly afflicts those with reduced mobility and/or sensation. Wheelchair users, particularly those with spinal cord injury, are particularly at risk of developing them. Deep tissue injury is caused by the prolonged loading of muscles, which causes muscle breakdown due to excessive mechanical deformation in its early stages, and later on due to the effects of ischemia and reperfusion. It has been suggested<sup>1</sup> that there exists a loading threshold that determines whether muscle damage can reverse itself naturally once the external loading is removed, or if damage continues to progress after the muscle is unloaded. The goal of this study is to establish this damage threshold.

### Methods

Experiments were conducted in 9 groups of Sprague Dawley rats. All rats underwent a spinalization surgery at the level of the T8 vertebra. Two weeks after spinalization surgery the rats were placed in a muscle loading apparatus to induce a deep tissue injury in one hind limb. Under inhalation anesthesia, the triceps surae muscles in one limb of each rat were externally loaded for 2 hrs. The level of loading utilized was equivalent to 38% of body weight (BW), 44% of BW, or 50% of BW. After this single loading session, muscle injury was assessed 1 day later, 3 days later, or 7 days later. Muscle damage was assessed using T<sub>2</sub> weighted Magnetic Resonance Imaging and confirmed post-mortem via a histological analysis.

### Results

All rats exhibited similar extents of muscle damage, of ~36% of the muscle, after 1 day post loading regardless of the amount of loading utilized (Figure 1). For the rats loaded to 38% of BW, damage was reduced 3 days post loading, with damage decreasing from 35% to 24%. After 7 days post loading,

muscle damage had almost completely disappeared in this group, with only 6% of the muscle exhibiting signs of damage. In comparison, for both the 44% BW and 50% BW group of rats, damage progressively increased as the time post loading increased. Three days post loading the extent of muscle damage had nearly doubled from its 1 day post loading level, increasing from 37% to 70%. By the 7<sup>th</sup> day post loading time point, the extent of muscle damage had further increased to 78% of the muscle.

### Conclusions

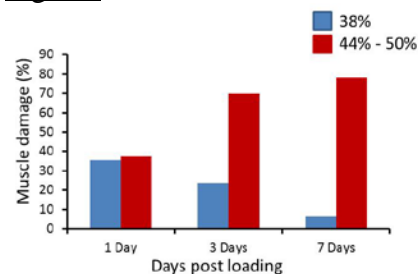
The results of this study suggest that the loading threshold for irreversible muscle damage lies in the range between 38% of BW and 44% of BW. This relatively small range is significant because the average load around the ischial tuberosities of wheelchair users falls within this range. In addition to this, understanding the exact threshold beyond which further muscle damage becomes irreversible, even upon the removal of external loading is critical for any potential intervention. Identifying a damage threshold could prove decisive when determining when an intervention should take place or which intervention is the most advisable.

### References

#### References

1. Loerakker S, Stekelenburg A, Strijkers GJ, Rijpkema JJ, Baaijens FP, Bader DL, Nicolay K, Oomens CW. *Temporal effects of mechanical loading on deformation-induced damage in skeletal muscle tissue*. Annals of Biomedical Engineering. 38(8): 2010

### Figures



## The biomechanics and histopathology of aneurysmal growth of the descending aorta post-surgical repair of the ascending aorta

Alina Ismaguilova, Giampaolo Martufi, Eric J. Herget, Jason K. Wong, Angela Franko, Amy B. Bromley, Jehangir J. Appoo, Elena S. Di Martino  
University of Calgary, Calgary, Canada

### Introduction

A thoracic aortic aneurysm (TAA) is recognized as the focal dilatation of any segment of the thoracic aorta caused by the loss of structural integrity of the arterial wall. Further enlargement of a TAA and subsequent wall thinning can lead to severe complications such as vessel rupture or the development of a tear in the intimal wall referred to as a dissection. Variable incidences of aneurysmal growth in the descending aorta following the surgical repair of acute Stanford Type A aortic dissection have been observed. The current basis for monitoring aneurysmal expansion is via determining the change in maximum aneurysmal diameter over time. This method, however, only monitors aneurysmal growth at one cross-section, thus areas of fast growth in other areas of the aneurysm will be missed and axial growth cannot be quantified (Martufi et al. 2014). With the use of three-dimensional remodeling techniques and histochemical analysis of surgical samples, it is possible to develop a more quantitative, non-invasive method of risk assessment of TAA growth in patients that have undergone surgical resection of the ascending aorta.

### Methods

The descending aorta of 30 patients (21 male and 9 female) was systematically reconstructed from CTA data (A4clinics, VASCOPS) to monitor three-dimensional growth over time. Inclusion criteria for this study involves Type A dissection patients with at least 1 year of follow-up and the availability of at least two sufficiently high-resolution CTA scans that allowed an accurate three-dimensional reconstruction. Aneurysm growth was monitored at 100 cross-sections perpendicular to the centerline per single reconstruction. Histological colorimetric analysis was done on surgically removed specimens from the dissection site in the ascending aorta to

measure the amount of proteoglycans, smooth muscle, and elastin, and to quantify medial thickness, degree of cystic medial degeneration, and inflammation.

### Results

The results indicate that the descending aorta grows haphazardly at various locations along its length with areas of fast diameter expansion as well as, remarkably, areas of shrinkage (Fig. 1). More specifically, maximum aneurysmal growth does not necessarily correspond to maximum diameter. When compared with aortas showing diffuse inflammation, cases with focal cystic medial degeneration (CMD) in the ascending aortic segment exhibited the highest maximum growth in the descending aorta.

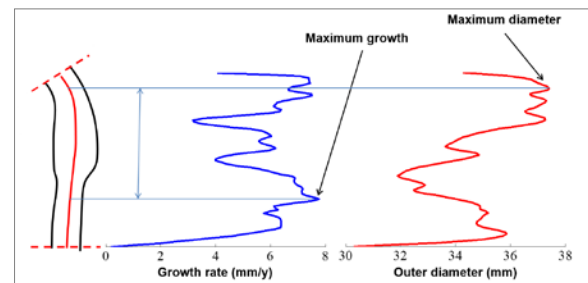


**Fig. 1.** Comparison between growth rate (mm/year) and outer diameter (mm) of a descending TAA.

### Conclusions

Due to the heterogeneous nature of vessel dilatation, localized spots of fast diameter growth can be detected through multiple centerline-based diameter measurements over the whole aneurysm sac, further reinforcing the quality of aneurysm surveillance. There also exists a correlation between wall degeneration and aneurysmal growth of the descending aorta following a Type A dissection.

### References

Martufi G, Gasser TC, Appoo JJ, Di Martino ES. Mechano-biology in the thoracic aortic aneurysm: a review and case study. *Biomech Model Mechanobiol.* 2014. DOI: 10.1007/s10237-014-0557-9

## The function and influence of ion channels in synovial fluid derived Mesenchymal progenitor cells

Karri Bertram  
Karri.bertram@ucalgary.ca

### Introduction

Osteoarthritis (OA) is a chronic disease characterized by progressive articular cartilage degeneration<sup>1</sup>. Normally, the synovium plays a role in maintaining health of articular cartilage. Resident synovial fluid mesenchymal progenitor cells (sfMPCs) have the ability to differentiate into bone, fat, and cartilage<sup>2</sup>. In OA, sfMPCs have greater proliferative but reduced chondrogenic capacities<sup>3</sup>. The physiological environment of the joint may play a role in the regenerative capacity of the sfMPCs present. It has been shown by our lab and others that the osmolality of OA joints is significantly lower (~280mOsm) compared to healthy joints (~400mOsm)<sup>4</sup>. Our lab has also demonstrated that both normal and diseased cells differentiate best in similar osmotic environments as they were in vitro<sup>4</sup>. Yet, with the change in osmotic environment cell volume does not change. Therefore, there must be ion channels responding to osmotic changes. The purpose of my research has been to determine which ion channels play a role in regulating cell volume in these sfMPCs in response to changes in the osmotic environment. Ultimately, understanding the differences in diseased and normal sfMPC physiology can lead to novel regenerative therapies.

### Methods

Synovial fluid samples were taken from the knee joints of OA (n=2) and normal (n=2) human patients. Samples were purified for sfMPCs using a magnetic bead technique. sfMPCs were then cultured and differentiated. A variety of ion channel genes and proteins were measured using quantitative PCR, flow cytometry and patch clamp.

### Results

Quantitative PCR results indicated that almost all gene expression of ion channels studied is upregulated in OA sfMPCs

compared to normal. The gene KCNMB1, a calcium activated potassium channel, was down regulated in OA cells compared to non-diseased cells. However, patch clamp results showed that OA sfMPCs showing detectable inward rectifier current (54% vs. 79% in non-diseased cells) and the amplitude of this current (measured at -80 mV) are significantly reduced compared to non-diseased sfMPCs. Flow cytometry results showed a significant decrease in TRPV4 in OA sfMPCs compared to non-diseased cells. The results for the potassium inward rectifier channel (KCNJ12) and the calcium activated potassium channel (KCNMB1) show very little change between OA and non-diseased cells in both sets of patients.

### Conclusions

These results indicate that although gene expression is upregulated in OA cells there is a translational suppressant preventing the genes to form functional proteins. Further studies must be done to determine what this translational suppressant may be. Uncovering more about the why proteins are being suppressed in OA sfMPCs may lead to novel treatments for Osteoarthritis in the future.

### References

1. L.S. Lohmander. What can we do about osteoarthritis? *Arthritis Res.*, 2 (2000), pp. 95–100
2. De Bari C, Dell'Accio F, Tylzanowski P, Luyten FP. [Multipotent mesenchymal stem cells from adult human synovial membrane](#). *Arthritis Rheum.* 2001 Aug;44(8):1928-42. PubMed PMID: 11508446.
3. RJ Krawetz et al. Synovial Fluid Progenitors Expressing CD90+ from Normal but Not Osteoarthritic Joints Undergo Chondrogenic Differentiation without Micro-Mass Culture. *PLoS One.* 2012; 7(8): e43616.
4. Bertram KL, Krawetz RJ. [Osmolarity regulates chondrogenic differentiation potential of synovial fluid derived mesenchymal progenitor cells](#). *Biochem Biophys Res Commun.* 2012 Jun 8;422(3):455-61. doi: 10.1016/j.bbrc.2012.05.015. Epub 2012 May 10. PubMed PMID: 22579684.

## Validated Simulation Model for Evaluating Radial Force of New Stent Design

Mehdi Jamshidi, Dr. Bahareh Vafadar,  
Dr. U Sundararaj, Dr. Alim Mitha  
University of Calgary

### Introduction

Stents are tubular meshes, typically made from metal that are navigated into the diseased blood vessel using catheters and provide a rigid structure to improve blood flow (in the case of a blocked or narrowed blood vessel) or to divert blood flow away from an aneurysm, causing it to clot off [1].

Radial force (RF) and flexibility are the most important factors of stent design. While RF is an important mechanical property used in designing stents, high RF is associated with some complications such as in-stent restenosis, an exuberant inflammatory response or thrombosis due to aggressive healing response of the artery [1]. In contrast, low RF leads to poor support of artery which may increase the risk of thrombosis and stent migration in the artery [2].

Since there are no standards which determine the maximum and minimum RF for designing the stent, best references as a criterion are commercial stents. Thus, the aim of this study is to establish a validated simulation method for evaluating the RF of commercial stents. This study can be employed in future studies in order to decrease cost of the designing process.

### Methods

Three self-expandable intracranial (Neuroform (open-cell), Enterprise (close-cell), and Solitaire (close-cell)) and two balloon-expandable cardiac (Integrity and Multi-Link) stents were selected for RF testing. Stents were scanned using micro CT and DICOM images were obtained. Three dimensional finite element models were then constructed using Simpleware software. The RF was simulated by compression of the stent between two plates using ABQUS software.

Simulation results of self-expandable stents were verified by experimental testing using ElectroForce® Load Frame Systems 3200 products machine.

### Results

The RF (in Newton, N) of the Neuroform, Enterprise, Solitaire stents was determined to be 0.142 N, 0.150 N, 0.196 N, respectively, by compression between two plate for 50% of the stent diameter experimentally. By comparison, the simulation results demonstrated the RF to be 0.140 N, 0.151 N, 0.195 N and for Integrity and Multi-Link1 to be 15.3 N and 13.86 N, respectively. The simulation results of radial force correlated with the experimental test.

When comparing balloon-expandable vs. self-expandable stents, the balloon expandable stents had a much higher RF. When comparing self-expandable open-cell and closed-cell stents, the closed-cell had a slightly higher RF.

### Conclusions

These studies have shown that simulation results of radial force testing are in excellent agreement with experimental results for self-expandable stents. Furthermore, balloon-expandable stents have a higher RF compared with self-expandable stents. Among self-expandable stents, the closed-cell design has higher radial force compared to open-cell design stents. Knowledge of the RF between these different types of stents and correlation with clinical outcome can aid in the purposeful design of stents for the cardiac and intracranial circulations.

### References

1. Julian Bedoya et al., Journal of Biomechanical Engineering, 2006, 128:757-765.
2. A. García, E. Peña and M.A. Martínez, Journal of the Mechanical Behavior of Biomedical Materials, 2012, 10:166-175.

# Monitoring of pressure during scoliosis surgery.

Negar Behzadi Fard , Aleksandra Krajacic, Francois D. Roy, Sarah Southon, Kajsa Duke

**Introduction:** Tingling, numbness and redness in lateral femoral cutaneous nerve (LFCN) occurs in 20% of the patients who have scoliosis surgery<sup>1</sup>. In this study, the intraoperative pressure is monitored by Force Sensing Array (FSA) pressure sensing mats (Vista medical, Winnipeg). Somatosensory evoked potential (SSEP) is also measured during the operation. The results from FSA and SSEP are used to determine the correlation (if any) between intraoperative pressure and the incidence of LFCN injury.

Figure 1:  
Redness after surgery



**Material and Methods:** A set of three pressure mats (FSA, Vista Medical, Winnipeg) were placed on the Jackson frame before positioning the patient. The average and maximum of pressure for chest, left/right thigh was calculated by data collected during the whole surgery from start to closing for 9 patients. Since any increase or decrease in SSEP signals can cause dysfunction, the LFCN SSEP was tested by stimulating the anterolateral thigh and recording the evoked potentials over the somatosensory cortex. After surgery, the patients were asked if they have numbness or tingling in their thighs. Light touch sensation testing was also performed. Moreover, the appearances of the redness of the front iliac crests are documented to be compared to the thigh condition.

**Results:** Data collection was monitored continuously except the time for electrocautery since the noise interrupts the pressure mats. The maximum and average are

shown in Table 1. The pressure increased over time. The changes in pressure were monitored during different surgical procedures such as opening, x-rays, screw insertion, rod rotation and closing. Duration of the surgery was noted to see the relation between the amount of pressure and the surgical time. The max pressure during screw insertion occasionally rose to the max amount that can be measured by each pressure mat which is 310 mmHg for soft pressure mat and 517 mmHg for the hard one. The average of pressure on the chest was measured on one cushion under the chest and once on two cushions, as this was the surgeon’s preference. The pressure on the left chest was higher on than the right chest. Four out of 9 patients had redness and blisters on the anterior thigh after surgery. Two if those four patients had a loss of sensation. SSEP data was inconclusive.

Table 1: Results

Case	chest		Left hip		Right hip		Duration (hours)
	Average (mmHg)	Max	Average (mmHg)	Max	Average (mmHg)	Max	
1	51	310	23	175	22	357	5
2	42	220	29	303	34	371	5
3	68	310	29	199	27	313	4
4	51	291	18	240	26	319	5
5	49	148	26	222	21	517	4
6	25	146	20	282	16	285	5
7	19	310	28	136	25	100	6
8	47	310	36	319	21	163	5
9	90 (Left)	310 Left	32	517	27	187	9
	22 (Right)	243 Right					

**Conclusions:** Continuous pressure monitoring was achieved during surgery and changes were noticed over time. More data is needed to determine the correlation between LFCN injury and pressure.

References: 1) Mirovsky Y, Neuwirth M. Injuries to the lateral femoral cutaneous nerve during spine surgery. Spine, 2000 May 15; 25(10):1266-9

## Novel force sensing system for studying head-helmet contact in simulated impacts

Robert C. Butz and Christopher R. Dennison

Biomedical Instrumentation Lab, Department of Mechanical Engineering, University of Alberta

### Introduction

Helmets have virtually eliminated fatal head/brain injury in many sports [1]. However, mild traumatic brain injury (mTBI) persists. Head/brain FE models suggest transient impact force location on the head could be predictive of mTBI [2]. As a result, some research groups are investigating helmet performance through head/helmet contact forces. These groups apply commercially available sensors that have known issues of poor accuracy [3] and inadequate bandwidth for impact research [4]. Our group is developing a novel force sensor to integrate with helmet test headforms. This force sensor has bandwidth in excess of 10kHz, exceeding industry requirements and far exceeding that of currently applied force sensors. Unlike commercially available sensors, our sensor can be configured for tri-axis force sensing of normal and shear forces, which is important in head rotation kinematics, thought to be an mTBI predictor. This sensor system will be used to test whether forces correlate with mTBI indicators in brain FE models that we apply in our ongoing research on head injury biomechanics.

### Methods

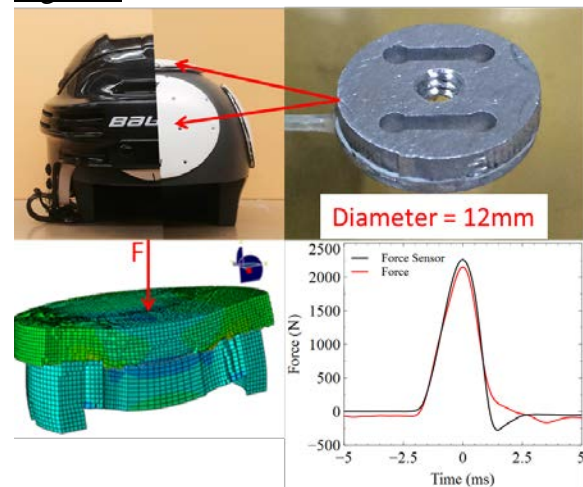
Forces applied to the sensor (Fig.1) create strains in a fixed-fixed beam that are measured using an optical fiber Bragg grating (FBG) sensor. Strain causes optical wavelength shift, which can be detected as a function of applied forces (sensitivity, nano-m/N). We used ABAQUS to: predict sensor resonances, size the sensor such that it can withstand typical impact forces, and predict its sensitivity (verified through calibration).

### Results and Conclusions

Modal analysis predicted first resonance at 70 kHz, which ensures appropriate bandwidth for studying impacts. Predicted

force sensitivity was  $6 \times 10^{-4}$  nm/N. Impact calibration predicted average sensitivity of  $8.25 \times 10^{-4} \pm 0.45$  nm/N (mean and SD), which is 27% greater than ABAQUS predicted. As shown in Fig.1, the sensor is capable of measuring impact forces of magnitude and timescale typical of helmet impact. In the next phase of this work we will embed an array of sensors into a custom plastic skin (San-Splint) that covers the headform (Fig.1) and validate the array. Upon validation, these force sensors will be capable of resolving force transients and experimentally testing emerging hypotheses of head protection: that force transient magnitude and distribution can be predictive of diffuse brain injury.

Figure 1



Top Left: Test headform. Top Right: Force sensor. Bottom Left: ABAQUS model. Bottom Right: Calibration data from sensor.

### References

- [1] Mueller et al, Clinical Sports Medicine. 17(1), 1998.
- [2] Viano et al, Concussion in professional football: part 9, Neurosurgery, 57(5), 2005.
- [3] Ouckama and Pearsall, Journal of Sports Engineering and Technology, 226(3/4), 2012.
- [4] SAE J211-1, Instrumentation for Impact Test—Part 1, SAE International, 2007.

## Comparative Study for Motion Tracking and Image Registration in Cardiac Optical Mapping

Marcela Rodriguez<sup>1</sup> and Anders Nygren<sup>1,2</sup>

<sup>1</sup>Dept. of Electrical & Computer Engineering and <sup>2</sup>CBRE, University of Calgary

### Introduction

Removal of motion artifacts in cardiac optical mapping videos would allow the technique to overcome a major disadvantage and be used as a reliable technique to evaluate action potentials (APs) in whole heart experiments. This would enhance the ability of the technique to provide data that permits the effective evaluation of electrophysiological parameters such as action potential durations (APDs).

We believe image registration would contribute toward reducing the pixel misalignment in the recorded fluorescence video frames helping to reduce the shape distortion of APs.

Motion tracking of the video frames would provide the registration step with valuable information to calculate the correct transformation to be used. Two approaches for motion tracking are evaluated here, including preliminary results for landmark-based image registration.

### Methods

Two approaches were used to track the motion of the fluorescence images throughout the video. SIFT descriptors [1] were used to calculate and track a limited number of landmarks and optical flow (OF) [2] was used to calculate the motion of every pixel in the images. A landmark-based rigid registration algorithm was used to register the images. The effectiveness of motion tracking with the proposed approaches was assessed based on the APD recovered from registered datasets.

### Results

Two types of simulated datasets were used to test the viability and effectiveness of OF and SIFT algorithms for landmark tracking in cardiac fluorescence images. Simulated data with known APD values allowed direct comparison between algorithms. Both types of datasets were created using one experimentally recorded fluorescence image as the base (first) frame of the video. Subsequent frames were created by adding

motion to the base frame in one of two ways 1) simulating real artifacts encountered in experimentally recorded data using a combination of transformations in random amounts added to a base motion and 2) by applying different motion patterns, ranging from simple individual translations to a combination of translation, rotation, shearing and scaling transformations.

Recovered APs obtained from SIFT landmark-based registration yielded APDs closer to the expected value (true APD<sub>90</sub> = 51.66 ms) and APs showed to have a better correction, see Fig. 1. APs were recovered from 18 different locations over the surface; statistics are shown in Table I.

TABLE I. STATISTICS FOR APD<sub>90</sub> IN REGISTERED DATASETS

	SIFT	OF
Mean	49.86	60.94
SD	7.69	30.41

Motion tracking with SIFT landmarks showed better results in the presence of affine transformation compared to the results of OF; however, the recovered datasets after landmark registration using OF information resulted in smoother APs.

Registered experimentally recorded datasets were visually evaluated. Consistent with the results obtained with simulated datasets, landmark-based registration with SIFT landmarks yielded better correction.

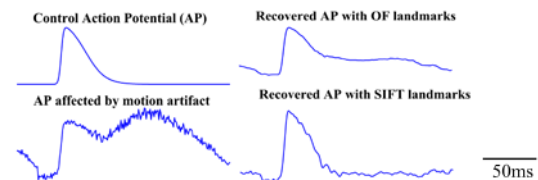


Fig.1 Example of simulated APs with motion artifact and the Recovered APs with SIFT and OF landmark-based registration.

### Conclusions

Motion estimation in cardiac optical images is feasible using both OF and SIFT, however the accuracy of SIFT makes it preferable. Preliminary landmark-based registration results are encouraging for gross motion artifacts removal.

### References

- [1] CVPR, 2432:2439,2010
- [2] AIJ, Vol. 17, 185:233, 1981

## Fitting single cell cardiac ventricular myocyte model to biological membrane resistance and AP data reduces mean square error in voltage and membrane resistance

Jaspreet Kaur<sup>1</sup>, Anders Nygren<sup>1</sup>, Edward J. Vigmond<sup>1,2</sup>

<sup>1</sup>University of Calgary, Canada, <sup>2</sup>Université de Bordeaux, France

### Introduction

The standard procedure to fit parameter sets of non-linear equations in cardiac single cell ionic models to reproduce experimental data is to adjust maximum conductances to fit an action potential (AP) waveform. However, different sets of parameters can produce similar APs [1], and even with similar APs in single cell simulations, the APs in tissue simulations may be different. We hypothesize that this uncertainty can be reduced by also fitting membrane resistance ( $R_m$ ). We have previously demonstrated the feasibility of this approach using simulations (model-to-model fits). Here, we extend this work to experimental data sets.

### Methods

To investigate the importance of  $R_m$ , we developed a multi-objective parallel genetic algorithm (GA) approach [2]. Two protocols were used for fitting: 1) fitting AP only, 2) fitting both AP shape and  $R_m$ . The MATLAB global optimization toolboxes and parallel computing toolbox were used. The first objective function is to minimize the normalized mean square error (MSE) difference in the APs and the second is to minimize the normalized absolute difference in  $R_m$  at  $n$  different  $V_m$  values during the AP. The GA finds a pareto set of solutions. We fit a rabbit ventricle single cell ionic model [3] to two different sets of experimentally recorded rabbit APs and  $R_m$  values provided by Dr. K.W. Spitzer, Univ. of Utah (unpublished data). The AP in data set 1 was similar to the baseline AP of the rabbit ventricle model, whereas the AP for data set 2 was significantly different.

### Results

In our previous work, MSE in  $V_m$  and  $R_m$  for fitting one human ventricle model to another, decreased by 94.9% and 96.5% respectively by including  $R_m$  as an objective function. For data set 1, including  $R_m$  as an objective function resulted in small improvements in MSE in  $V_m$  and  $R_m$  of 4.2% and 11.2%, respectively. For data set 2, the corresponding improvements were

more substantial at 75.5% and 98.5%, respectively (Fig. 1). Importantly, for both data sets, the variability in  $G_{Na}$ ,  $G_{Kix}$ ,  $G_{tos}$ ,  $G_{tof}$ ,  $G_{NaK}$  was reduced at least by 97%, and for  $G_{Kr}$ ,  $G_{Ks}$  and  $G_{Ca}$  by 10-66%. This reduction in parameter variability is comparable to the 40-95% observed in model-to-model fits in our previous work.

### Conclusions

As in our earlier model-to-model fitting study, AP+ $R_m$  fit (compared to AP only fit) reduces variability in parameter values across the set of pareto optimal solutions when applied to experimental data. AP+ $R_m$  fit also improves MSE in  $V_m$  and  $R_m$ . The extent of the improvement in MSE depends on how similar the data is to the model. If the data is similar to the baseline model, the MSE improvement is modest (data set 1). However, when the data is very different from the model (data set 2), larger MSE improvements are possible.

### References

- 1) Sarkar A. X. et. al (2010) PLoS Comput Biol 6(9): e1000914.
- 2) Kaur J et. al (2014) PLOS One (in press).
- 3) Mahajan A. et. al. (2008), Biophysical journal 94: 392–410.

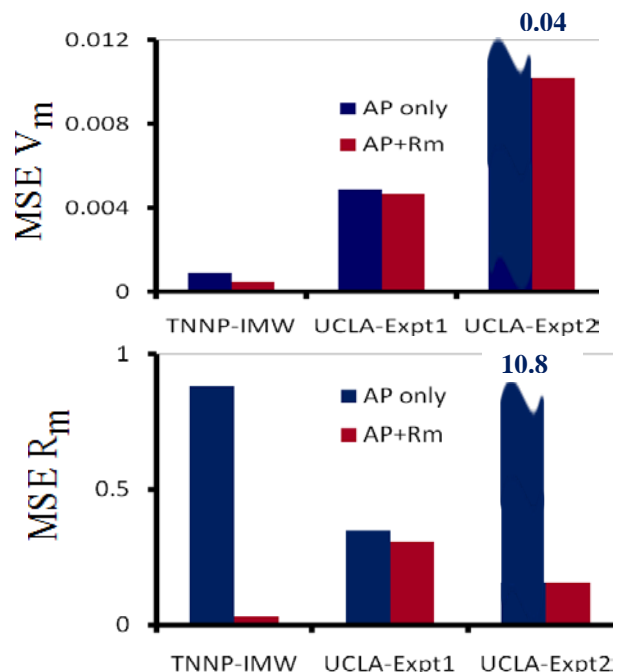


Fig. 1: MSE in  $R_m$  and  $V_m$

## Muscle Fascicle Length is Reduced in Old Age Owing to Shorter Sarcomeres and Serial Sarcomere Loss

Sean Crooks, Geoffrey A. Power, Walter Herzog

Human Performance Laboratory, University of Calgary, 2500 University Drive NW, Calgary, AB, Canada T2N 1N4

fewer sarcomeres in series when compared to young,  $p < 0.001$ .

### Introduction

With natural human aging, there are alterations to the structural components of the muscular system that result in impaired contractile function and decreased performance in activities of daily life.<sup>1</sup> Despite reductions in active force, passive force is often reported to be greater in muscles from older adults compared with young.<sup>2</sup> A potential unexplored mechanism for increased passive force in old age could be decreased fascicle lengths owing to a decrease in sarcomeres number in series.

The purpose of this study was to compare muscles of young and old rats to determine fascicle length, sarcomere numbers and the sarcomere length at which peak force is obtained (i.e. plateau of the force-length (FL) relationship;  $L_0$ ).<sup>3</sup> It was hypothesized that fascicle length would be shorter owing to less sarcomeres in series.<sup>4</sup>

### Methods

A young ( $\approx 20$  human yrs.) ( $n=9$ ) and old cohort ( $\approx 75-80$  human yrs.) ( $n=8$ ) of rats were used. The medial gastrocnemius muscle (MG) from the right leg was surgically isolated and attached to a force transducer. For muscle activation, the tibial nerve was electrically stimulated and  $L_0$  was determined by performing a standard FL relationship. The animals were sacrificed and the MG muscle was fixed at  $L_0$ . Next, the muscles were digested in acid and fascicles isolated for sarcomere length measurement by laser diffraction. Fascicle length measurements were taken using pixel counting software. Serial sarcomere numbers were calculated by dividing the fascicle length by the average sarcomere length. In total, 340 fascicle length and 1700 sarcomere length measurements were taken.

### Results

A reduction in fascicle length of  $\sim 14\%$  was observed in the old rats when compared to young,  $p < 0.001$ . There was a reduction in average sarcomere length of  $\sim 4\%$  in the old rats versus the young,  $p < 0.001$ . The MG of old rats showed  $\sim 10\%$

### Conclusions

The reduction in fascicle length was associated with a lower sarcomere number in series for the old age cohort. Serial sarcomere number is important when considering the FL relationship.<sup>3</sup> For example, if the limbs of young and old were at matched joint angles such as what occurs *in vivo*, the shorter fascicles in the old would suggest the sarcomeres would be stretched to longer lengths. This would mean that older adults may be operating further on the descending limb of the FL relationship contributing to muscle weakness. Additionally, as sarcomeres in aged muscle are being pulled to longer lengths, passive force producing elements such as titin may play a larger role in the increased passive tension in older adult muscle.<sup>1</sup>

The results of this study were in accordance with the hypothesis that in muscle fascicles from aged muscle, not only are sarcomeres lost in parallel, but are also in series, resulting in shorter fascicles. But quite unexpectedly average sarcomere length was shorter at  $L_0$  in the old compared with young. These results may help to explain increased stiffness and passive force of muscles of older individuals.

### References

1. Power, Dalton & Rice. *J Sport Health Sci.* **2**:215-226, 2013.
2. Burkholder & Lieber. *J Exp Biol.* **204**:1529-1536, 2001.
3. Hill, *Proc R Soc Lond B Biol Sci.* **141**:104-117, 1953.
4. Hooper. *J Gerontol.* **27**:121-126, 1981.

## Site Specific Inflammation and Cellular Composition of Synovial Tissue Within Osteoarthritic Knee Joints

By: Kate O'Brien; Supervisor: Roman Krawetz  
2500 University Dr. NW, Calgary AB, CANADA, T2N 1N4

### Introduction

Osteoarthritis (OA) is a degenerative joint disorder which affects every tissue present within the synovial joint. Signs of OA include alterations in articular cartilage composition, structure and function; symptoms include joint pain and stiffness. Cartilage degeneration and accelerated bone turnover are causal elements in the progression of OA. Risk factors include age, weight and previous joint trauma, however the interaction of these factors is unknown. It is this lack of knowledge surrounding the pathogenesis of OA which makes diagnosis of the disease at its earliest stages extremely challenging. The current diagnostic gold standard is imaging, however these tools can only indicate OA once irreversible cartilage degeneration has already occurred. OA is the leading cause of disability in Canada, and costs an estimated \$33 billion per annum. It is apparent that we are in need of a tool to better understand and diagnose/treat OA prior to the onset of cartilage damage.

### Methods

The current study examines human synovium biopsies taken from early OA patients at the time of arthroscopic knee surgery and compares them to normal tissue biopsies harvested from cadaveric donations. Synovium is removed from two to four sites within each joint. Histological analysis (hematoxylin and eosin (HE)); immunohistochemistry (IHC) is performed on each biopsy to determine inflammatory score and identify cellularity. Sections are analysed for inflammatory score, presence of CD90/CD271 (mesenchymal progenitor cells (MPC)), CD68/CD14 (macrophages) and CD177 (neutrophils). Results are compared between early OA and normal joints and within joint to determine joint heterogeneity.

### Results

Preliminary results show that early OA joints have significantly more synovial inflammation than synovium from normal joints. Early OA joints also appear to have increased numbers CD90, CD271, CD68 and CD14 positive cells than normals. There is significant within joint heterogeneity of inflammation and cell types. Further analysis will reveal if this heterogeneity is directly correlated to cartilage pathology.

### Conclusions

It appears that there is a significant difference in the inflammation and number of cells positive for MPC and macrophagic cells between early OA and normal synovium. Additionally, significant within joint heterogeneity is observed in early OA joints. The identification of these cells and trends provides insight into the pathogenesis and potential targets for treatment for OA at its earliest stages.

### References

- Arthritis Facts & Figures (2014). The Arthritis Society. Retrieved on September 6, 2014 from [www.arthritis.ca/facts](http://www.arthritis.ca/facts)
- Felson, D.T. (2006). Osteoarthritis of the Knee. *The New England Journal of Medicine*. 354, 841-848.
- Lane, N.E. (2007). Osteoarthritis of the Hip. *The New England Journal of Medicine*. 357, 1413-1421.
- Scanzello C.R., Goldring S.R. (2012). The role of synovitis in osteoarthritis pathogenesis. *Bone*, 51(2), 249-257.

## 9.4T MRI of a model of pediatric concussion shows vascular abnormalities

Imhof E<sup>2,3,4</sup>, Esser M<sup>1,3,4</sup>, MacMillan CJ<sup>2,3,4</sup>, Mychasiuk R<sup>1,4</sup>, Dunn JF<sup>2,3,4</sup>

<sup>1</sup>Alberta Children's Hospital Research Institute, <sup>2</sup>Hotchkiss Brain Institute, <sup>3</sup>Faculty of Medicine, <sup>4</sup>U. of Calgary

### Introduction

Mild traumatic brain injury (mTBI), sometimes referred to as concussion, is the most common form of brain injury in Canada. mTBI is caused by traumatic biomechanical forces [1]. Currently, no CT or MRI methods have been shown to be sensitive enough for diagnosis or monitoring of mTBI. Little is known regarding the pathophysiological changes in mTBI, particularly in children. A growing body of literature suggests that the pediatric brain may be more susceptible to injury than the adult brain [2], and that there may be sex-differences in outcomes [3]. We used high resolution MRI to assess structural and functional changes associated with mTBI in juvenile, male and female rats

### Methods

Male and female juvenile Sprague-Dawley rats underwent a novel modified closed-head impact acceleration to induce mTBI [4]. Behavioural studies include time to right, as well as a beam walking test. mTBI (female n=5; male n=4) and control rats (female n=2; male n=1) were imaged 24h post-injury with a 9.4T MRI. Sequences used were multi-echo T2, T2w, RARE, diffusion-weighted imaging, and arterial spin-labeling. Regions of interest (ROIs) were drawn on the hippocampus, prefrontal cortex, basal ganglia, and corpus callosum.

### Results

Behavioural studies showed impaired righting response and foot slips in mTBI animals post-injury. Anatomical MRI showed enlargement in the large vessels, including the sagittal sinus and transverse sinuses (Fig. 1). The transverse sinuses (TS) showed enlarged vessel areas in mTBI (n=9) (right:  $0.14\text{mm}^2 \pm 0.06$ ; left:  $0.15\text{mm}^2 \pm 0.06$ ) compared to controls (n=3) (right:  $0.07\text{mm}^2 \pm 0.02$ ; left  $0.08\text{mm}^2 \pm 0.01$ ). The sagittal sinus in some animals was enlarged

as well. No differences were observed in either T2, T1, CBF or ADC.

### Conclusions

The measurable changes in vessel size indicate cerebrovascular dysregulation, consistent with what is seen in patients with mTBI. Adults and children have been shown to exhibit cerebrovascular dysregulation post-mTBI, including altered venous outflow and vascular reactivity impairment, respectively [5,6]. Headache is a common symptom post-mTBI and may be associated with decreases in cerebral blood flow [7]. Distention of the large draining veins supports the concept that there is vascular injury in mTBI.

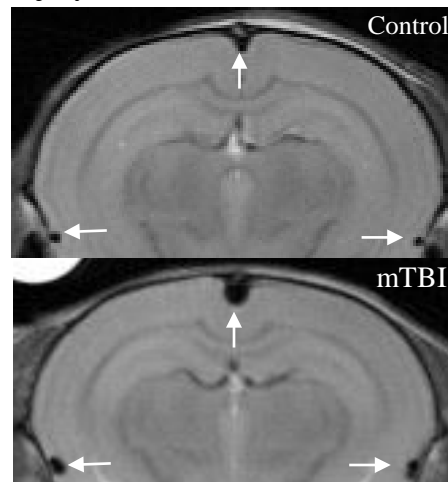


Fig. 1. RARE MRI of a control and mTBI animal 24h post injury. Visible enlargement of the sagittal and transverse sinuses.

### References

- [1] Borich MR., Cheung KL., Jones P., Khranova V., Gavriloff L., Boyd LA., Virji-Babul N. J Neurological Physical Therapy. 2013; 37:133-139.
- [2] Kirkwood MW, Yeates KO, Wilson PE. Pediatrics. 2006; 117(4):1359-71
- [3] Broshek DK, Kaushik T, Freeman JR, Erlanger D, Webbe F, Barth JT. J Neurosurg. 2005; 102:856-863
- [4] Mychasiuk R, Farran A, Esser MJ. J Neurotrauma. 2014; 31(8):749-57
- [5] Pomschar A, Koerte I, Lee S, Laubender RP, Straube A, Heinen F, Ertl-Wagner B, Alperin N. PLoS One. 2013; 8(2):e55447
- [6] Choe MC, Babikian T, DiFiori J, Hovda DA, Giza CC. Curr Opin Pediatr. 2012; 24(6):689-95
- [7] Gilkey SJ, Ramadan NM, Aurora TK, Welch KM. Headache. 1997; 37(9):583-7.

## The Influence of Footwear on Gait Asymmetry

Stefan Hoerzer<sup>a</sup>, Peter A. Federolf<sup>b</sup>, Christian Maurer<sup>a</sup>, Jennifer Baltich<sup>a</sup>, Benno M. Nigg<sup>a</sup>

<sup>a</sup>Human Performance Laboratory, Faculty of Kinesiology, University of Calgary, Canada

<sup>b</sup>Department of Neuroscience, Norwegian University of Science and Technology NTNU, Norway

### Introduction

Previous research on elderly people has suggested that footwear may improve neuromuscular control of motion, which may be clinically relevant in the prevention of falls<sup>1</sup>. If this is true, then such an improvement might already be present in young, healthy adults. A feature that is used to assess neuromuscular control is the level of gait asymmetry<sup>2</sup>. One challenge when assessing gait asymmetry changes caused by external boundary conditions (e.g. footwear) is that such changes apply to several body segments and that these may be smaller than the inherent variability of the movement.

Thus, the objectives of the study were to develop a comprehensive asymmetry index (CAI) that is capable of detecting changes caused by external boundary conditions, and to use CAI to investigate the influence of footwear on gait asymmetry during running in a healthy, young cohort. It was hypothesized that footwear decreases gait asymmetry as compared to barefoot running.

### Methods

Kinematics and kinetics were collected for both legs of 15 healthy subjects (7f/8m; age:  $25.4 \pm 4.4$  yrs). Subjects performed five barefoot and five shod (standard running shoe) over-ground running trials. Thirty continuous gait variables at the hip, knee, ankle joint and ground reaction forces were computed bilaterally from the raw data. The differences between variables for the right and left leg were calculated. Using this data, a difference vector for each subject and running condition (i.e. barefoot and shod) was obtained. The difference vector quantified all measured aspects of asymmetry of the subjects' gait. Based on the difference vectors a principal component analysis (PCA) was computed to obtain the CAI. It was expected that the PCA would increase sensitivity of the CAI by filtering out asymmetry artifacts that are due to the natural variability of the movement.

### Results

Figure 1 shows the subject-specific CAI. Averaged across all participants, the CAI for barefoot running was  $155.7 \pm 39.5$  (mean  $\pm$  SD) and for shod running was  $131.2 \pm 48.5$ . The difference between the two conditions was significant ( $p=0.041$ ). Comparing barefoot and shod running using an asymmetry index based on the raw difference vectors without PCA revealed no significant difference (barefoot:  $177.7 \pm 33.7$ , shod:  $157.9 \pm 39.1$ ;  $p=0.067$ ).

### Conclusions

This study had two main outcomes. First, a novel CAI was proposed that combined asymmetries in multiple gait variables and had an increased sensitivity for detecting changes in gait asymmetry. The CAI may, therefore, have important clinical applications such as monitoring the progress of neuromuscular diseases with respect to gait asymmetry. Second, the CAI confirmed the hypothesis that in healthy, young adults gait asymmetry is reduced when running in shoes compared to running barefoot. Changes in the afferent sensory feedback to the neuromuscular control system may be an explanation for this observation<sup>3</sup>.

### References

1. Koepsell, T. D., et al. *J Am Geriatr Soc.* 52: 1495-1501, 2004.
2. Patterson, K. K., et al. *Gait Posture.* 31: 241-246, 2010.
3. Alfuth, M. & Rosenbaum, D. *Footwear Sci.* 4: 1-22, 2012.

### Figures

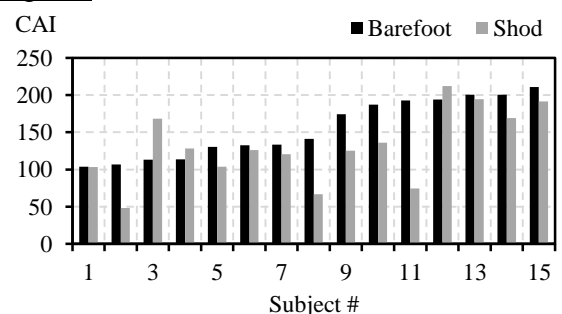


**Figure 1:** Subject-specific comprehensive asymmetry index (CAI).

## Viscoelastic Response of Mid-Palatal Suture Tissue in Finite Element Analysis

Russel S. Fuhrer<sup>1</sup>, Daniel L. Romanyk<sup>2</sup>, Jason P. Carey<sup>1</sup>

1. Department of Mechanical Engineering, University of Alberta, Edmonton AB T6G 2G8;
2. Department of Dentistry, University of Alberta, Edmonton AB T6G 1C9

### Introduction

Maxillary Expansion (ME) is a skeletal type orthodontic treatment that generates mid-palatal suture separation by expanding the maxilla arch and can be performed on children aged 7-15 [1,2] to correct improper bite, nasal respiratory problems, and sleep apnea [3]. Understanding the effect that soft tissue material responses have on the movement of the maxilla during treatment is required to work toward improved treatment efficiency and increased quality of life for patients undergoing ME. This study works towards creating a Finite Element (FE) modelling method to incorporate non-linear creep and viscoelastic material relationships in order to approximate the non-linear response of the maxillary suture during ME.

### Methods

Customized material response subroutines utilizing one dimensional (1-D) material constitutive models developed by Romanyk et al [4] were incorporated into FE simulations. The customized creep material models were encoded in a modified implicit subroutine for ANSYS v14.5 using FORTRAN77 with an Intel 11.1 FORTAN compiler. The FE models in ANSYS utilized the same cross-sectional suture geometry and dimensions as in Romanyk et al. To evaluate the tissue response of the creep subroutine, the FE models were subjected constant tensile forces of 0.49N, 0.98N, and 1.96N for a simulated period of six weeks. The results were then compared to the strains and stresses anticipated from the 1-D constitutive model.

### Results

FE model results show a greater than anticipated tissue creep under constant applied load. Figure 1 shows the final deformed results of a 6 week FE creep simulation that utilized three dimensional (3-D) non-linear brick elements for the suture. For the near incompressible suture material, visible necking can be seen as the suture elongates. Figure 2 shows the differences in stretch between the near incompressible 3-D suture, a suture made with bar elements with constant cross section during tensile

deformation, and the anticipated 1-D results over the course of 6 weeks simulated time under a constant 1.96N load.

### Conclusions

The 2-D bar elements with rigid cross sections and the 3-D brick element simulation results correlate well with the expected creep trends from literature [4] in the FE simulations, while the incompressible 2-D bar element simulation shows acceleration of creep rate towards failure, deviating from the expected creep trend. As such, future full skull FE simulations will be generated using the 3-D bricks and/or 2-D rigid cross section approaches to replicate treatment results for a randomly selected patient using pre- and post-treatment computed tomography images. A validated ME treatment FE model with accurate tissue response can be used to predict treatment outcomes, to design improved ME appliances and treatment protocols.

### References

- [1] Kumar S.A., et al., *J Clinical and Diagnostic Research* 5(4), 906-911;
- [2] Romanyk D.L., et al., *J Dental Biomechanics* 1(1), 496906;
- [3] Weissheimer A., et al., *American J Orthodontics and Dentofacial Orthopedics* 140(3), 366-376;
- [4] Romanyk D.L., et al., *J Biomechanics* 46(10), 1618-1625;

### Figures:

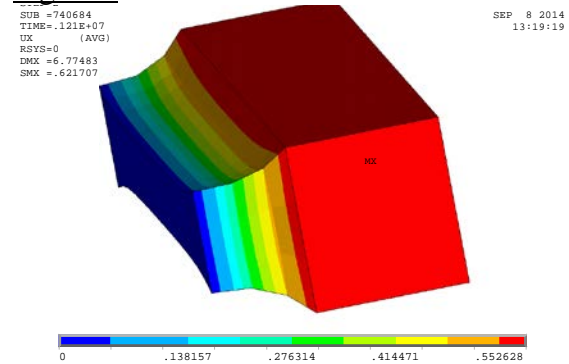


Figure 1: Deformed Creep Simulation. (200g Load, 6 weeks)

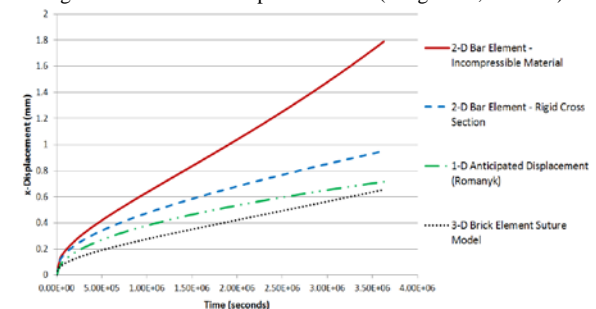


Figure 2: Displacement vs. Time Results (200g Load, 6 Weeks)

## AC Electrothermal Biofluid Transport, Numerical Study on the Substrate Thermal Conductivity

A. Salari<sup>1</sup>, M. Purdy<sup>2</sup> and C. Dalton<sup>1</sup>

<sup>1</sup>Department of Electrical and Computer Engineering, University of Calgary, Calgary, Alberta T2N 1N4, Canada

<sup>2</sup>Biomedical Engineering Program, University of Calgary, Calgary, Alberta T2N 1N4, Canada

### Introduction

AC electrothermal (ACET) micropumps are suitable for applications involving high conductivity fluids ( $>0.1 \text{ S/m}$ ), such as pumping biological fluids. ACET is a multiphysic phenomenon containing electrostatics, fluid dynamics, and heat transfer. Therefore, thermal characteristics of the system such as fluid thermal coefficient can affect the pumping performance. Silicon (130 W/mK), glass (1.1 W/mK), and Polydimethylsiloxane (PDMS) (0.16 W/mK) are among the most common used substrate materials for fabrication of ACET micropumps. In this paper, in order to study the effect of abovementioned substrate thermal conductivities on the pumping performance, an assumed substrate with thermal conductivity in the range of 0.1-15 W/mK is numerically investigated.

### Method

The ACET phenomenon was modeled using a 3D simulation of finite element software COMSOL Multiphysics. A single pair of microelectrodes with the dimensions taken from [1] placed on the top and bottom of two fluidic microchannels with the cross section of circular and rectangular shapes were used, in which the hydraulic diameters of the two channels were the same. Electrostatics of the system was first solved to determine the electric field distribution throughout the system. The generated Joule heating plays the role of heat source in the biofluid causing permittivity and conductivity gradients in the bulk of the fluid, which consequently generate electrothermal force. Navier Stokes equations was then solved having the electrothermal force as the external body force.

### Results

Fig. 1 shows that how electrothermal velocity field is generated throughout the fluidic microchannel. The curvature

observed in streamlines show the ACET vortices at that point, which is near to the surface of the thin electrode. Also, higher velocities are observed at the center area of the microchannel far from the walls. Fig. 2 shows that increasing the thermal conductivity can decrease the ACET flow rate. For the modeled micropump, substrates with thermal conductivities  $>5 \text{ W/mK}$  seem not to have significant effect on the ACET flow rate. Also, the rectangular fluidic channel is capable of generating higher flow rates than the circular one.

### Conclusions

The effect of thermal conductivity changes of the substrate material on the ACET flow rate was investigated. The results showed higher flow rates for smaller values of thermal conductivity.

### References

[1] A. Salari, R. Zhang, C. Dalton, *BME Conference, Banff, Canada* (2013).

### Figures

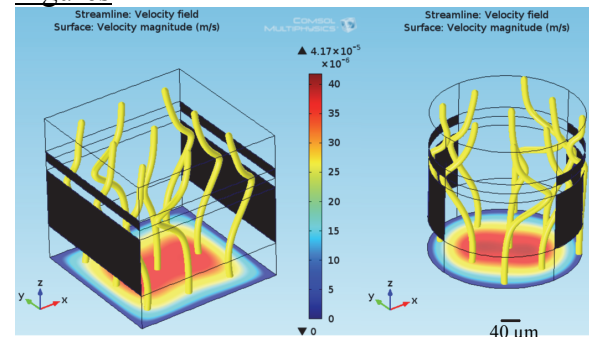


Fig. 1 ACET flow generated for the substrates with  $k=15 \text{ W/mK}$ . Black areas show the actuated microelectrodes; thin one is actuated at  $V_{\text{rms}}=7$ , and wide one is grounded.

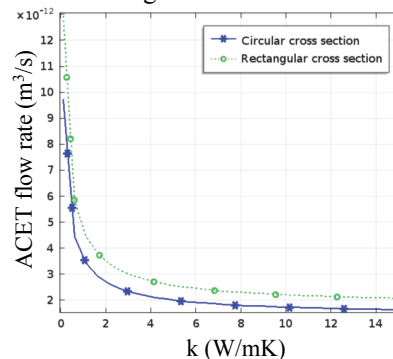


Fig. 2 ACET flow rate versus the thermal conductivity of the substrate material.

## Measuring functional connectivity of event related optical signals by optical imaging

Urban K.J.<sup>1,2,3</sup>, K.M. Barlow<sup>2,3</sup>, B. Goodyear<sup>3</sup>, L. Sewell<sup>3</sup>, and J.F. Dunn<sup>1,2,3</sup>

<sup>1</sup>Experimental Imaging Center, <sup>2</sup>Alberta Children's Hospital Research Institute, <sup>3</sup>Hotchkiss Brain Institute, Faculty of Medicine, University of Calgary

### Introduction

Functional Near Infrared Spectroscopy (fNIRS) may have the ability to detect the event related optical signals (EROS) corresponding to neuronal activation. fNIRS is typically used to measure the magnitude of task activation and functional connectivity through low frequency oscillations [1]. These measurements are based the slow response to neuronal activation as increased cerebral blood flow, increase in oxy-hemoglobin (Hb) and decrease in deoxy-Hb [1,2,3]. It has been suggested that neuronal activation causes high frequency changes in scattering due to cellular conformational changes [4]. Currently there is mixed opinion on whether fast optical reflect neuronal activation. [5,6]. The aim of this study was to be the first to explore functional connectivity in a range of high frequency bands as a marker of high frequency optical signals.

### Methods

Pediatric controls (age 12.5±0.6) completed a 5 minute resting state and a 5 minute tapping task (30s rest, 15s tapping). The head cap was placed over motor cortex based on anatomical area. The CW5 NIRS system records the absorption of near infrared light wavelength of 690nm (deoxy-Hb) and 830nm oxy-Hb. Coherence analysis used a reference seed from the left side, ipsilateral, fiber pair showing the maximum response to finger tapping in the right hand. Comparisons were made between 3 source-detector pairs closest to reference fibre pair from left, and 4 corresponding pairs from the contralateral hemisphere. Coherence was completed in 0.04-0.1 Hz, 0.1-1 Hz, 1-2 Hz, 2-3 Hz, 3-4 Hz, 4-8 Hz, 8-10 Hz and 10-50Hz frequency ranges. A two way analysis of variance (ANOVA) and tukey multiple comparisons was completed for frequency, and task (p=0.05). Each test was performed for both hemisphere, oxy-Hb and deoxy-Hb.

### Results

Oxy-Hb: Left and right hemisphere coherence was greatest in the 0.04-0.1Hz range, and decreased with increasing frequency until reaching the high frequency ranges of 8Hz. There was a significant difference in coherence between resting state and task activation in the ipsilateral hemisphere at 8-10Hz (p=0.04) and 10-50Hz (p=0.01) frequencies. In the contralateral

hemisphere there was also an increase at 8-10hz (p=0.05) and 10-50Hz (p=0.05).

Deoxy-Hb: There was no significant difference between resting state and tapping for left or right hemisphere in coherence.

### Conclusions

This study is the first to use EROS to study coherence in the pediatric population. This study shows evidence of interregional brain communication occurring at a high frequency.

### References

- [1] Varshney VP et al. (2012) J. Europ. Opt. 7: 12047
- [2] Franceschini MA et al. (2006) J Biomed Opt 11
- [3] Huppert TJ et al. (2009) Appl Opt 48: 280-298.
- [4] Yao X et al. (2005) BioPhys J: 88(6).
- [5] Radhakrishnan (2009) Neuroimage: 45, 410-419.
- [6] Gratton G (2010) Front. Hum. Neurosci:4(52)

### Figure:

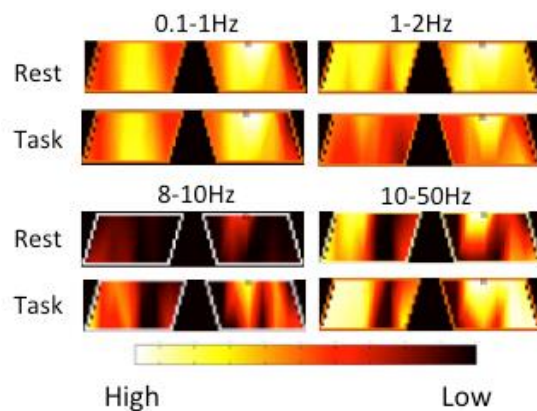


Fig. 1. Oxy-Hb Coherence during resting state (top) and tapping (bottom) for 0.01-1 Hz, 1-2Hz, 8-10Hz, and 10-50Hz frequencies from one subject. This example illustrates the increase in coherence during tapping and coherence in higher frequencies.

## Prediction of Local Proximal Tibial Subchondral Bone Stiffness using Subject-Specific Finite Element Modeling: Effect of anisotropy inclusion

S. Majid Nazemi<sup>1</sup>, S. A. Kontulainen<sup>2</sup>, D. R. Wilson<sup>3</sup>, James D. Johnston<sup>1</sup>

<sup>1</sup> Mechanical Engineering Department, University of Saskatchewan, Saskatoon, SK, Canada

<sup>2</sup> College of Kinesiology, University of Saskatchewan, Saskatoon, SK, Canada

<sup>3</sup> Department of Orthopedics and Centre for Hip Health and Mobility, UBC, Vancouver, BC, Canada

### Introduction

Quantitative Computed Tomography (QCT) based subject-specific finite element (FE) modeling has potential to clarify the role of subchondral bone alterations in knee osteoarthritis (OA) pathogenesis. Calculation of bone elastic moduli (E) from image data is a basic step when constructing QCT-FE models. However, different relationships between E and bone mineral density (BMD) have been reported in the literature [1]. The results of our previous study suggest application of Goulet's equation (with a normalized root mean squared error of 17.6%, expressed in relation to maximum stiffness (RMSE%)) for QCT-FE prediction of local proximal tibial subchondral bone stiffness [2]. This QCT-FE model used an isotropic elastic modulus, whereas, tibial trabecular bone has been found to be at least orthotropic in anisotropy [3]. The objective of this study was to investigate the effect of accounting for bone's anisotropy on the accuracy of QCT-FE in prediction of local stiffness at the tibial subchondral surface using four orthotropic material models developed based on existing density-moduli relationships.

### Methods

Using in-situ macro-indentation testing, stiffness was measured at the subchondral surface of 13 individual medial:lateral proximal tibial compartments (from 1 female and 7 male donors of age ranging from 51 to 88 years old). In total, 48 indentation points were acquired. Using commercial image processing (Analyze) and reverse engineering software (Geomagic), QCT images of the potted samples were converted to FE models of each sample (Abaqus). QCT-based measures of bone mineral density were converted to bone elastic moduli in Anterior-Posterior (1), Medial-Lateral (2) and Superior-Inferior (3)

directions using four published nonlinear density-moduli relationships (Models 1: Rho et al., 2: Keyak et al., 3: Hodgkinson and Currey and 4: Goulet et al.) [4-7]. The only existing tibial specific relationship linking shear moduli and density was used for all four models [3]. For all models, Poisson's ratios were considered as  $\nu_{12}=0.427$ ,  $\nu_{13}=0.234$  and  $\nu_{23}=0.257$  [8]. For isotropic models, only the elastic modulus in Superior-Inferior direction and a Poisson's ratio of 0.3 was considered [2]. Elastic properties were then mapped to corresponding FE models using custom algorithms (Matlab). FE-based proximal tibial stiffness values were compared to experimentally measured stiffness values using RMSE%.

### Results

Accounting for bone's anisotropy reduced RSME% in case of all evaluated density-modulus equations (from a range of 17.6%-141.6% for isotropic models to a range of 16.2%-58.4% for orthotropic models). The orthotropic material model based on Goulet et al. E-BMD relationships yielded the least error between measured and predicted stiffness values (16.2%).

### Conclusions

Accounting for bone's anisotropy improves the accuracy of QCT-FE for predicting local stiffness at the proximal tibial subchondral surface. Further improvement may be achieved by 1) accounting for trabecular bone's local anisotropy and orientation in and 2) calculating orthotropic elastic properties using fabric in addition to density.

### References

[1] Helsen B et al. (2008), [2] Nazemi S M et al., WCB2014, [3] Ashman R B et al. (1989), [4] Rho J Y et al. (1995), [5] Keyak J H et al. (1994), [6] Hodgkinson R and Currey J D (1992), [7] Goulet R W et al. (1994), [8] Gray H A et al. (2008).

## Application of fiberoptic sensor technology to detect abnormal stress on the cartilage covering the knee joint

P. Vakil<sup>1</sup>, M. Atarod<sup>1</sup>, Y. Achari<sup>1</sup>, C. R. Dennison<sup>2</sup>, C. B. Frank<sup>1</sup> and N. G. Shrive<sup>1</sup>

1. McCaig Institute for Bone and Joint Health, University of Calgary, Calgary,

2. Biomedical Instrumentation Lab, Department of Mechanical Engineering, University of Alberta

**Introduction:** Knee joint injuries involving rupture of the anterior cruciate ligament (ACL) and/or meniscal tears often lead to the development of post-traumatic osteoarthritis (PTOA). Osteoarthritis (OA) is a debilitating and often painful chronic disease which has severe impact on the mobility of the affected individual. Abnormal joint motions resulting from such severe knee injuries possibly initiate PTOA and contribute to disease progression. Patients with ACL tears are advised to undergo reconstructive surgery aimed at restoring normal joint function. However, despite successful reconstruction of the ACL there is evidence that such patients still develop OA in that joint.

Different techniques have been used to capture the alterations in knee joint motions and tissue loads following injury or surgery. The non invasive techniques use skin surface markers but are limited in terms of accuracy and motion specificity while invasive techniques have the potential to alter natural joint mechanics. Recently, fiber-optic techniques have been proposed for biomechanical applications as they are small and biocompatible [1].

We have developed a novel testing platform combining an instrumented spatial linkage for *in vivo* kinematic assessments and a unique 6 degrees of freedom, parallel robotic system for accurate reproduction of *in vivo* joint motions and measurement of *in situ* joint/tissue loads [2, 3]. We have determined the load-carrying characteristics of different tissues within the ovine knee joint during normal gait [3]. We are now poised to determine the deviations in cartilage stress due to changes in surface interactions following injury or surgery.

**Hypothesis:** We hypothesize that alterations in relative surface configuration affect contact stresses on the articulating surfaces of the knee joint and play a role in PTOA

pathogenesis. To identify the location and magnitude of these changes in the early stages of disease we aim to apply fiber-optic sensor technology in conjunction with the parallel robot. The paradigm that we are testing is that the cartilage is unable to adapt to a large change in stress and will begin to degrade in a process exacerbated by continued application of the abnormal stress.

**Methods:** The ovine model of early joint degeneration following knee joint injuries or ACL reconstructive surgery has been well established [4]. Initially, the fiber-optic sensors will be installed at the joint surfaces. The joint will be loaded and tested on the parallel robot system and the locations of the high stresses and joint loads determined. Later, we will determine the changes in stress in relation to areas of focal damage in the cartilage.

**Results:** The technique of using the fiber-optic system will be unique in determining the altered joint loads resulting from even subtle changes in joint motion. Once the technique is established, we will determine the changes in shear and normal stress in the knee joint after transection of the ACL and relate these to the damage observed to the cartilage of those joints in the ovine model.

**Conclusions:** The observations from these studies will determine whether changes in stress initiate PTOA, or drive its progression, thus leading us towards potential therapies for the early stages of the disease.

**References** 1: Dennison CR, et al. (2008). *Spine*,1;33(17):E589-94. PMID: 18670326.  
2: Atarod M, et al. (2014). *Ann Biomed Eng.*;42(5):1121-32. PMID: 24519725.  
3: Atarod M, et al.(2013). *Ann Biomed Eng.*;41(10):2067-76. PMID: 23673654  
4: Heard BJ, et al. (2011). *J Orthop. Res.*;29(8):1185-92. PMID: 21387397

## Detecting motion-corrupted data in diffusion tensor imaging data: applications for pediatric imaging

Alyssa Mah<sup>1</sup>, R. Marc Lebel<sup>2</sup>, Catherine Lebel<sup>3</sup>

<sup>1</sup>Biomedical Engineering Program, University of Calgary; <sup>2</sup>General Electric Healthcare; <sup>3</sup>Department of Radiology, University of Calgary

### Introduction

Magnetic resonance imaging (MRI) is a non-invasive imaging modality that allows for in vivo assessment of brain white matter [1]. There are few MRI studies pertaining to healthy brain development in young children because MRI requires participants to remain motionless for the duration of the entire protocol (approximately 30 to 45 minutes) – naturally a difficult task for young children. Anesthesia or sedation can be used to ensure subject compliance in clinical imaging, but it is not possible for research.

Diffusion tensor imaging (DTI) is an MRI technique that captures parameters important for quantitatively assessing white matter integrity, and DTI data can be used to virtually reconstruct neural pathways, a method known as tractography. However, subject motion during DTI acquisition can lead to corruption of data.

A novel application was designed to automatically detect and remove motion-corrupted volumes of DTI data, and re-calculate DTI parameters from only the good volumes (corrected data). It is a simple and quick method to salvage DTI data when there is corruption due to subject motion.

### Methods

DTI data was collected from 11 healthy children, aged 2–4 years. Diffusion weighted images were collected (single spin echo, slice thickness=2.2 mm, 30 directions  $b = 750 \text{ s/mm}^2$ , 5  $b = 0 \text{ s/mm}^2$ , 4:12 min:sec, 35 volumes total) on the 3 T system (Discovery MR750w; General Electric; Waukesha, WI) using a 32-channel head coil at the Alberta Children's Hospital.

Processing time is approximately 3 min per subject. Motion-corrupted volumes of data were determined by using a high pass filter to detect substantial edges in volumes of data. An example of removing motion-corrupted data on the re-calculation of

fractional anisotropy (FA) maps is shown in Figure 1. Paired t-tests were used to compare measurements between uncorrected and corrected data sets in three selected white matter pathways.

### Results

Of the 11 subjects, 8 had some motion-corrupted data. In the whole set 0 – 9 volumes were removed, and the use of our application led to significant volume increases in corrected mean total fiber ( $p=0.035$ ) and mean inferior fronto-occipital fasciculus ( $p=0.042$ ) compared to uncorrected data. A trend was observed in corrected mean superior longitudinal fasciculus volume ( $p=0.061$ ). No significant increases were observed for the genu of the corpus callosum.

### Conclusions

Our application demonstrates improved tractography results (larger tract volumes) in young children. The application is currently being installed and will be tested on the MRI scanner for immediate online reconstruction by removing motion-corrupted data. The use of the application could increase feasibility and efficiency of non-sedated MRI in young children by reducing time needed in the scanner.

### References

[1] C. Lebel, L. Walker, A. Leemans, L. Phillips, and C. Beaulieu, "Microstructural maturation of the human brain from childhood to adulthood," *Neuroimage*, vol. 40, pp. 1044-55, Apr 15 2008.

### Figures

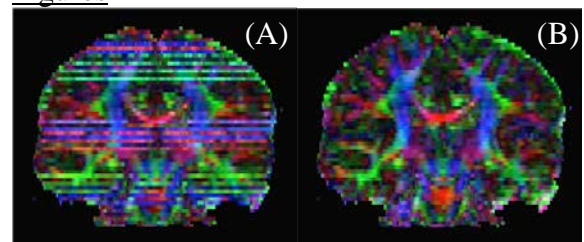


Figure 1 (A) Uncorrected FA map, (B) corrected FA map from 9 volumes of data removed.

## Soft Biological Tissues with Statistical Fibre Orientation: Efficient Computation of the Mechanical Properties

Kotaybah Hashamoun<sup>1</sup>, Alfio Grillo<sup>2</sup>, Salvatore Federico<sup>3</sup>

<sup>1</sup> Graduate Programme in Mechanical Engineering, The University of Calgary, Canada

<sup>2</sup> DiSMA G. Lagrange, Politecnico di Torino, Italy

<sup>3</sup> Department of Mechanical and Manufacturing Engineering, The University of Calgary, Canada

### Introduction

The constitutive functions describing the mechanical properties of soft biological tissues with statistical fibre orientation (e.g., articular cartilage) are evaluated by means of averaging integrals over the set of all possible directions in space<sup>[1]</sup>. In general, it is not possible to evaluate these integrals once and for all as the integrand (which could be an elastic potential, a stress, an elasticity tensor, a permeability, etc.) depends on both deformation and fibre direction. Rather, numerical integration is necessary at each deformation increment in a Finite Element (FE) [1]. However, for the case of polynomial functions, a once-and-all, exact integration, performed at the beginning of the simulation, is possible. The aim of this work is to introduce and test a method based on the Taylor expansion of a given function.

### Methods

Given a fibre constitutive function, e.g., the elastic potential  $W_1$ , the Taylor expansion about a structure tensor  $\mathbf{A}^* = \mathbf{M}^* \otimes \mathbf{M}^*$ , where  $\mathbf{M}^*$  is a given direction, is

$$W_1(\mathbf{A}, \mathbf{C}) = \sum_{n=0}^{\infty} \frac{1}{n!} \left\langle \frac{\partial^{(n)} W_1}{\partial \mathbf{A}^{(n)}} (\mathbf{A}^*, \mathbf{C}) \left| \otimes^n (\mathbf{A} - \mathbf{A}^*) \right. \right\rangle$$

where  $\otimes^n (\mathbf{A} - \mathbf{A}^*) = (\mathbf{A} - \mathbf{A}^*) \otimes \dots \otimes (\mathbf{A} - \mathbf{A}^*)$ . With a suitable truncation, the directional averaging integral of this polynomial in  $\mathbf{A}$  can be evaluated directly. Once the overall potential  $W$  has been retrieved as

$$W(\mathbf{C}) = \phi_{0R} W_0(\mathbf{C}) + \phi_{1R} \int_{\mathbb{S}^2 \mathcal{B}_R} \psi(\mathbf{A}) W_1(\mathbf{A}, \mathbf{C})$$

where the probability  $\psi$  could be, e.g., a von Mises distribution [2], the Cauchy stress is evaluated as

$$\boldsymbol{\sigma} = J^{-1} \mathbf{F} \left( 2 \frac{\partial W}{\partial \mathbf{C}} \right) \mathbf{F}^T$$

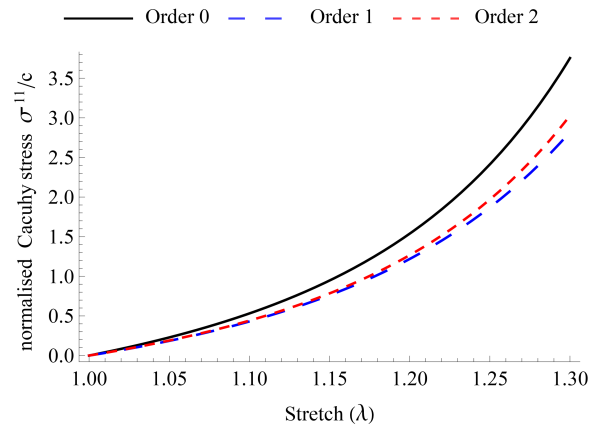
All calculations were performed using Wolfram Mathematica 9.0 [3].

### Results

A uniaxial tensile test was performed for the exponential fibre potential function

$$W(\mathbf{C}, \mathbf{A}) = (c/2) (e^{\alpha(\mathbf{C}:\mathbf{A}-1)^2} - 1)$$

and the zero-, first- and second-order approximations of the Cauchy stress were plotted as a function of the stretch in the dominant fibre direction (see figure below).



### Summary and Future Work

The mechanical properties of soft biological tissues with statistical fibre orientation must be evaluated via directional averaging integrals. An efficient approximation of these integrals can be obtained by means of Taylor expansion to a desired order.

We plan to assess this method by comparing it with the method of the spherical designs [4], which has proven to be robust, but computationally expensive.

### References

- [1] Federico S, Herzog W, 2008, *J. Biomech.*, 41:3309-3313
- [2] Gasser TC, Holzapfel GA, Ogden RW, 2006, *J. Roy. Soc. Interface*, 3: 15-35
- [3] Wolfram Research, Inc., 2012, Mathematica, Version 9.0, Champaign, IL, USA
- [4] Federico S, Gasser TC, 2010, *J. Roy. Soc. Interface*, 7: 955-966

## Estimated Bone Strength by Finite Element Analysis at Distal Skeletal Sites Predicts Femoral Failure Load

Andres Kroker<sup>1,2</sup>, Britta Jorgenson<sup>2,3</sup>, Kyle Nishiyama<sup>1,2</sup>, Steven Boyd<sup>1,2,3</sup>

<sup>1</sup>Schulich School of Engineering, <sup>2</sup>McCaig Institute for Bone and Joint Health, <sup>3</sup>Department of Radiology, Faculty of Medicine, University of Calgary

### Introduction

Osteoporosis is a degenerative bone disease characterized by reduced bone mass and increased fracture risk. The WHO uses areal bone mineral density (aBMD) measured by dual energy X-ray absorptiometry (DXA) to define osteoporosis<sup>1</sup>. However, more than 50% of all fractures in elderly people appear in individuals not classified as osteoporotic by this definition<sup>2</sup>. DXA provides a 2D estimate of bone density, but bone strength also depends on bone micro-architecture<sup>3</sup>. High-resolution peripheral quantitative computed tomography (HR-pQCT) is an imaging modality capable of capturing microarchitecture *in vivo* at peripheral skeletal sites. This study aims to investigate if these peripheral measurements can predict bone morphology and strength at the femoral neck, a central site prone to fracture that cannot be assessed by this modality.

### Methods

The left and right distal radius, tibia, and proximal femur of 10 cadavers were imaged by HR-pQCT (N=59). The radius and tibia were imaged using the standard *in vivo* protocols (9.02 mm segment, 82  $\mu$ m isotropic voxel size). The proximal femur was imaged and the neck was extracted using a custom protocol. Due to morphological differences each neck analysis region had a different thickness. The following morphological parameters were obtained: cortical porosity (Ct.Po), BMD (Ct.BMD), and thickness (Ct.Th); trabecular BMD (Tb.BMD), thickness (Tb.Th), and number (Tb.N); total BMD (Tt.BMD) and bone area (Tt.Ar). Finite element analysis (FEA) was performed on the peripheral measurements using a linear uniaxial compression model. Failure load (FL) and stiffness (K) were estimated and compared to the results of the mechanically tested femurs that were loaded to failure in a sideways fall configuration<sup>4</sup>.

### Results

All morphological and biomechanical parameters were significantly correlated between radius and tibia with the exception of Ct.Po and Ct.BMD. Between the radius and femoral neck only Tt.Ar ( $r(12)=0.81$ ,  $p<0.01$ ) and Tb.BMD ( $r(12)=0.56$ ,  $p<0.05$ ) were significantly correlated. No other morphological parameters reached significant correlations. Failure load correlated moderately but significantly between the radius and femur ( $r(15)=0.49$ ,  $p<0.05$ ). Between the tibia and femoral neck Tt.Ar ( $r(12)=0.55$ ,  $p<0.05$ ) and Tb.BMD ( $r(12)=0.57$ ,  $p<0.05$ ) were the only morphological parameters with significant correlations. Notably, both biomechanical parameters correlated significantly; K ( $r(15)=0.61$ ,  $p<0.01$ ) and FL ( $r(15)=0.73$ ,  $p<0.01$ ).

### Conclusions

The non-significant correlations for the majority of the morphological parameters between the peripheral sites and the femoral neck are consistent with previous studies<sup>5</sup>. Site-specific trabecular structure measured by bone biopsies<sup>6</sup> may explain the low morphological correlations. The significant correlations between FEA estimated failure load at peripheral sites compared to the experimentally determined failure load at the femur suggest that despite differences in morphology, bone strength at central sites can be inferred from peripheral measurements. Specifically the tibia and femur, both weight bearing bones, correlated very well. HR-pQCT measurements at the distal tibia with FEA may compliment aBMD measures and improve bone strength prediction.

### References

1. Kanis and WHO 1994 Osteoporosis Int.;
2. Stone et al. 2003 J. o. Bone and Mineral Res.;
3. Adams 2013 Nature Rev. Endocri.
4. Nishiyama et al. 2013 J. o. Biomechanics;
5. Cohen et al. 2010 Osteoporosis Int.;
6. Hildebrand et al. 1999 J. o. Bone a. Mineral Res.

## Mitochondrial dynamics in the brain of an autistic mouse model (BTBR T+ tf/j) in response to a ketogenic diet.

Warren Xu<sup>1</sup>, Christopher Newell<sup>2</sup>, Virginia L. Johnsen, Jong M. Rho<sup>3,4</sup>, Younghee Ahn<sup>3,4</sup>, Jane Shearer<sup>1,5</sup>

<sup>1</sup>Center for Bioengineering Research and Education, Departments of <sup>2</sup>Medical Science, <sup>3</sup>Pediatrics, <sup>4</sup>Clinical Neurosciences and <sup>5</sup>Biochemistry and Molecular Biology. Alberta Children's Hospital Research Institute for Child and Maternal Health, Faculty of Medicine, University of Calgary, Calgary, AB. Canada

### Introduction

Mitochondrial dysfunction is implicated in the development of autism spectrum disorders (ASD), likely due to the high energetic demands of neurodevelopment. The specific mechanisms causing this dysfunction are undetermined, but mitochondrial dynamics have been implicated as a potential cause. Ketogenic diets (90% kcal fat) are known to be neuroprotective in ASD. The aim of this study was to investigate the effects of a ketogenic diet (KD) on mitochondrial dynamics in the brain tissue of a mouse model exhibiting symptoms of ASD (BTBR T+ tf/j).

### Methods

Mitochondrial dynamics are governed by five essential fission-fusion proteins (*Fis1*, *Drp1*, *Mfn1*, *Mfn2*, *Opa1*). Male, BTBR T+ tf/j mice were fed either a chow (n=8) or KD (n=8) for 12-14 days. Following diets, the prefrontal cortex was isolated and examined. Changes in relative gene expression were established using qRT-PCR while protein expression of four of the same proteins (DRP1, MFN1, MFN2, OPA1) were analyzed by immunoblotting.

### Results

KD treated animals had a lower mass (-44%) compared to those fed a standard chow diet (p<0.05). As expected, KD resulted in reduced blood glucose and a 5-fold increase in circulating ketones. In the brain, analysis of mitochondrial gene expression revealed KD to significantly increase in the expression of *Drp1* and *Fis1* (fission) as well

as *Opa1* (fusion) (p<0.01). Despite changes in the relative gene expression, no detectable changes in the four fission/fusion proteins were detected including three different isoforms of OPA1. This suggests that changes in gene expression were not translated into alterations in protein levels.

### Conclusions

Animals consuming a ketogenic diet exhibited changes in genetic expression of three fission/fusion components, but no significant changes in the protein expression of mitochondrial dynamics in the brain of BTBR mice. Given this, the neuroprotective effects of KD diets in ASD can not be explained by changes in mitochondrial fission/fusion protein dynamics.

## Investigating Validation of Physiological Cost Index for Wheelchair Users

Zohreh Salimi<sup>1</sup>, M.Sc; Martin Ferguson-Pell<sup>1</sup>, Ph.D; Ailar Ramadi<sup>1</sup>, M.Sc; Robert Haennel<sup>1</sup>, Ph.D; Farhood Mohammadi<sup>2</sup>, M.Sc; Liping Qi<sup>3</sup>, Ph.D

1- Faculty of Rehab. Medicine, University of Alberta; 2- Math. and Statistical Sciences, University of Alberta; 3- Department of Electrical and Electronics Engineering, Dalian University of Technology

### Introduction

In this study we aim to examine the validity of a simple, easy to measure physiological factor, the PCI (Physiological Cost Index). PCI is a validated factor for walking<sup>1</sup>. It is an indicator of the energy cost<sup>2</sup> during walking with self-selected speed<sup>3</sup>. PCI has also been used for studying wheelchair users<sup>4,5</sup>, but the validity of this measure for wheelchair users has never been studied. If this measure proved to be valid in assessing wheelchair users, it could simplify wheelchair research studies, by reducing the need to wear an oxygen mask and a portable metabolic cart to the wheelchair when performing the target task. PCI, adapted for wheelchair propulsion is obtained by using this formula<sup>2</sup>:

$$PCI = (\text{wheeling heart rate} - \text{resting heart rate}) / \text{wheeling speed}$$

### Methods

12 experienced wheelchair users participated in the experiment approved by Ethics board of University of Alberta after giving written consent. They performed 4 bouts of 3-minute submaximal tests on a wheelchair ergometer, starting with a self-selected speed test and then three other tests with constant speeds in a random order: 1, 1.3, and 1.6 m/s. Kinematic data was recorded using SMART<sup>Wheels</sup> on both side of the wheelchair and heart rate and oxygen uptake was recorded using Oxycon metabolic cart.

### Results

Mechanical Work (MW) and Energy Expenditure (EE) was calculated using data of SMART<sup>Wheels</sup> and Oxycon. Using the Tukey method showed there was no outlier in the data. According statistical references<sup>6</sup>, the Pearson correlation coefficient for a sample size of 12 and  $\alpha$ -level of 0.05 should be greater than 0.591 to conclude there is a relationship. However, as shown in Table 1, PCI did not show any relationship with EE nor MW. Table 2 shows the efficiency of wheelchair propulsion for each test.

**Table 1. Pearson Correlation Coefficient**

Test	PCI_MW	PCI_EE	MW_EE
<b>Comf.</b>	0.02	0.34	0.65
<b>1</b>	0.24	0.07	0.45
<b>1.3</b>	-0.11	-0.08	0.75
<b>1.6</b>	0.16	0.07	0.55

**Table 2. Efficiency of wheelchair propulsion**

Test	Mean (%)	SD (%)
<b>Comf.</b>	14.24	7
<b>1</b>	14.63	6.3
<b>1.3</b>	17.19	7.55
<b>1.6</b>	21.83	7.81
<b>Overall</b>	16.97	7.59

### Conclusions

PCI is a very convenient index of metabolic energy cost that could particularly help patients to self-monitor their level of energy expenditure. However, this study shows that PCI is not a valid index of metabolic energy cost for wheelchair users. The efficiency of wheelchair propulsion at self-selected speed was 14.24% which is consistent with the results of other publications (15.1%<sup>7</sup>).

### References

1. Reliability of Physiological Cost Index Measurements in Walking Normal Subjects Using Steady-state, Non-steady-state and Post-exercise Heart Rate Recording. 1978.
2. Chin T, Sawamura S, Fujita H, et al. The efficacy of physiological cost index (PCI) measurement of a subject walking with an Intelligent Prosthesis. *Prosthet Orthot Int.* 1999;23(1):45-9.
3. Graham RC, Smith NM, White CM. The reliability and validity of the physiological cost index in healthy subjects while walking on 2 different tracks. *Arch Phys Med Rehabil.* 2005;86(10):2041-6.
4. Hughes B, Sawatzky BJ, Hol AT. A comparison of spinerly versus standard steel-spoke wheelchair wheels. *Arch Phys Med Rehabil.* 2005;86(3):596-601.
5. Mukherjee G, Bhowmik P, Samanta a. Physical fitness training for wheelchair ambulation by the arm crank propulsion technique. *Clin Rehabil.* 2001;15(2):125-132.
6. Aspelmeier J. *Social and Behavioral Statistics, a User-Friendly Approach.* 2nd ed. e-book, Westview Press
7. Lenton JP, Fowler NE, van der Woude L, Goosey-Tolfrey VL. Wheelchair propulsion: effects of experience and push strategy on efficiency and perceived exertion. *Appl Physiol Nutr Metab.* 2008;33(5):870-9.

## **Contractile Properties of Cardiac Muscle Following Increasing Doses of Chronic Exercise Training and Overtraining in Rats: MSc Research Proposal**

Boldt, K. R.<sup>1,2</sup>, Joumaa, V.<sup>1,2</sup> & Herzog, W.<sup>1,2</sup>

<sup>1</sup>Human Performance Lab, University of Calgary, <sup>2</sup>Faculty of Kinesiology, University of Calgary

### Introduction

Participation in cardiovascular exercise and consequential aerobic fitness has been shown to be a top predictor of athletic performance as well as both morbidity and mortality in both healthy and clinical populations<sup>1</sup>. Improvements of heart function result from increased stroke volume and eccentric hypertrophy of the heart<sup>2</sup>. At the cell-level, mechanical improvements are a result of increased calcium sensitivity, greater power output, and greater relative and absolute force production<sup>3,4</sup>. Exercise training can however, when excessive, lead to overtraining and overreaching syndromes and decreases in fitness outcomes<sup>5</sup>. Despite the established understanding of cellular adaptations to aerobic exercise training, it remains to be determined how different volumes of exercise affect cardiac myocyte mechanical contractile properties, particularly when high training volumes lead to chronic overtraining. The purpose of this study is to 1) quantify the relationship between cardiac myocyte adaptations and varying volumes of cardiovascular exercise training and to 2) determine the effects of chronic overtraining on cardiac myocyte contractile properties.

### Methods

Twenty-four, five month old male Sprague-Dawley rats will be randomized into four groups: no exercise (control) group (n=6), short duration exercise group (n=6), long duration exercise group (n=6), and overtraining (excessive duration) exercise group (n=6). Training will consist of progressive treadmill exercise for 11 weeks. One week following the end of the 11 weeks of training, rats will undergo maximal aerobic exercise testing to determine differences between groups in fitness as well as dual energy x-ray absorptiometry (DEXA) to determine differences in body composition. Rats will then be euthanized, and heart tissues will be harvested and weighed. Single cardiac myocyte

preparations will be isolated and chemically skinned. Mechanical testing will consist of peak power output and calcium sensitivity. After mechanical testing, myocytes will be analyzed for their myosin heavy chain and myosin light chain isoform expression using gel electrophoresis. All data will be analyzed using one-way analysis of variance to determine differences between treatment groups.

### Expected Results

We hypothesize that 1) contractile properties and function of cardiac myocytes will improve with increasing doses of training, but will be negatively affected by regular exhaustive exercise, 2) animals with the greatest fitness levels will have the greater cell function, and 3) heart mass will be greater in trained animals but not with overtraining compared to controls.

### Significance

It is expected that increased performance of the heart stems, in part, from increases in contractile function of the cells. Understanding this relationship between endurance exercise volume and the mechanisms leading to mechanical adaptations of the myocardium will advance understanding of cardiac contractile properties and will provide valuable insight into optimizing training loads for maximum benefit in cardiovascular health and performance.

### References

1. Bassett & Howley, (2000). *Med. Sci. Sports Exerc.*, 32(1).
2. Morganroth et al., (1975). *Annals of Internal Medicine*, 82.
3. Diffie, Seversen & Titus, (2001). *Journal of Applied Physiology*, 91.
4. Diffie & Chung, (2003). *Journal of Applied Physiology*, 94.
5. Meeusen et al., (2006). *European Journal of Sports Science*, 6(1).

## IN SITU CHONDROCYTE MECHANICS FOLLOWING STATIC AND DYNAMIC COMPRESSIVE STRESSES

Svetlana Kuznetsova<sup>1,2</sup>, Isabelle Villemure<sup>3</sup>, Ziad Abu Sara<sup>1</sup>, Eng Kuan Moo<sup>1</sup>, Yasir Al-Saffar<sup>1</sup>, Walter Herzog<sup>1</sup>  
Human Performance Lab<sup>1</sup>, Physics and Astronomy Department<sup>2</sup>, University of Calgary, Ecole Polytechnique de Montreal<sup>3</sup>

### Introduction

Articular Cartilage (AC) is a thin layer of connective tissue covering bony surfaces of joints [1]. Chondrocytes maintain AC extracellular matrix, the integrity of which depends largely on compressive loads applied to the tissue. Past studies used strain control protocols to apply static or dynamic compression to AC and observe changes in chondrocyte morphology [1]. The purpose of this study was to use stress control, a more physiologically relevant loading protocol, and evaluate cell morphology for low magnitude dynamic and static compressions.

### Methods

Patellae from New Zealand white rabbits were isolated and randomly assigned to one of two loading protocols [2]: (i) static compression with a constant stress of 100kPa; (ii) dynamic sinusoidal compression at 0.1Hz with a stress of 100kPa $\pm$ 50%. Compression was applied for 60 min, followed by 30 min recovery. Cells were stained and tracked by laser scanning microscopy during the loading protocol.

### Results

Cell volume remained nearly constant during static loading but increased beyond the original volume during recovery Fig(1b). Cell volume decreased during dynamic loading and recovered to its original, pre-loaded value following load removal. Cell height (along the tissue thickness axis) decreased for dynamic loading, while the associated cell depth (perpendicular to the tissue thickness axis) increased Fig(1a). For static loading, there was little change in cell height, width and depth Fig(1b).

### Conclusions

The small changes observed in cell morphology during static loading are likely due to the low compressive load of 100kPa.

The volume increase following static loading could be associated with active processes of the cells that affect permeability. The great variations in cell deformations across samples during dynamic loading conditions could be due to differences in cartilage structure and mechanical properties of individual samples.

We were limited in our analysis to observations of chondrocytes within 50  $\mu$ m from the top surface of the articular cartilage. We are puzzled by the difference in mechanical response of cells in the static and dynamic loading conditions. We speculate that these differences in cell responses are associated with active shape and volume regulation of chondrocytes that differ between static and dynamic loading conditions.

### References

1. Han S, et al. *JBiomech.* **45**:2450-2456,2012.
2. Madden R, et al. *JBiomech.* **46**:554-560, 2013.

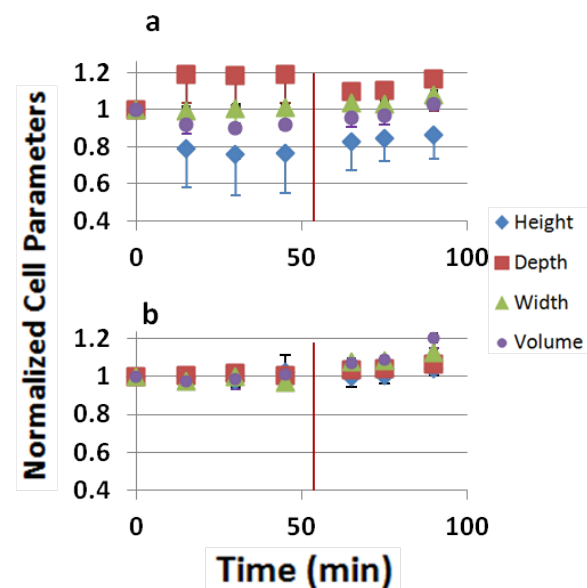


**Fig.(1):** Cell parameters normalized to the unloaded parameters for (a) dynamic (n=30) and (b) static (n=70) compressions. Red line separates loading and recovery periods. Mean $\pm$ 1SD

## The Influence of Age, Running Speed, and Running Distance on the Probability of Second Metatarsal Stress Fracture

Divya Budihal<sup>1</sup>, W. Brent Edwards<sup>2</sup>

<sup>1</sup>Henry Wise Wood High School, <sup>2</sup>Faculty of Kinesiology, University of Calgary, Calgary, AB

### Introduction

Stress fractures in long bones account for approximately 15% to 20% of all overuse injuries in runners.<sup>1</sup> The clinical consequence of stress fractures is localized pain of insidious onset and the inability to continue physical activity without rest or rehabilitation.<sup>2</sup> Cyclical loads applied to bone during locomotion cause microdamage accumulation, i.e., small cracks in the bony matrix. If this microdamage is not repaired by the action of basic multicellular units, stress fractures may occur.<sup>2</sup> The purpose of this study was to examine the influence of age, running speed, and running distance on the probability of stress fracture in the second (2<sup>nd</sup>) metatarsal, a major skeletal site for stress fracture development.

### Methods

Peak 2<sup>nd</sup> metatarsal stress during the stance phase of running was predicted for a 170 cm tall, 69 kg male using the finite element method. Stride length and ground reaction force as function of running speed were estimated from the literature.<sup>3</sup> Peak strain as a function of age was calculated from Hooke's law using an age specific modulus equation.<sup>4</sup> The number of cycles to failure for a given strain was calculated using a modified standard fatigue equation that accounted for age specific bone fatigue behavior.<sup>5,6</sup> The probability of 2<sup>nd</sup> metatarsal stress fracture as a function of age (15-65 years), running speed (2.5-4.5 m/s), and running distance (3-7 miles/day) was then determined using a theoretical model of stress fracture that accounted for bone failure, repair, and adaptation.<sup>7</sup>

### Results

The cumulative probability of stress fracture with repair and adaptation ( $P_{fra}$ ) for a referent scenario (i.e. 25 year old running at 3.5 m/s for 5 miles/day) peaked and plateaued at 0.15 after approximately 40 days of running (Figure 1).  $P_{fra}$  increased

nonlinearly with age and running speed. In contrast,  $P_{fra}$  increased linearly with running distance. To maintain the same probability of stress fracture as a 25 year old running at 3.5 m/s for 5 miles/day, the results indicated that a 55 year old must run at 2.5 m/s for 3 miles/day.

### Conclusions

The probability of stress fracture was less sensitive to changes in running distance than age or running speed; therefore, new runners may want to reduce running speed rather than distance in order to minimize their likelihood for 2<sup>nd</sup> metatarsal stress fracture. In accordance with these findings, older runners may want to adopt a slower running speed and a lower running distance when beginning a new running regimen. This study provides a comprehensive theoretical description of stress fracture probability that ultimately may aid in the prevention of this injury. In order to expand upon these results, future work will incorporate the concept of stressed volume into the theoretical model,<sup>7</sup> as well as more age-specific finite element modelling procedures.

### References

[1] Bennell (1996). *Am J Sports Med*, 24: 810-18. [2] Burr & Milgrom (2001). CRC Press NYC. [3] Mercer (2005). *J Sports Sci Med*, 4: 144-52. [4] Zioupos & Curry (1998). *Bone*, 22: 57-66. [5] Edwards (2010). *Clin Biomech*, 25: 372-77. [6] Diab (2005). *Eur J Morph*, 42: 53-9. [7] Taylor (2004). *J Ortho Res*, 22: 487-94.

### Figures

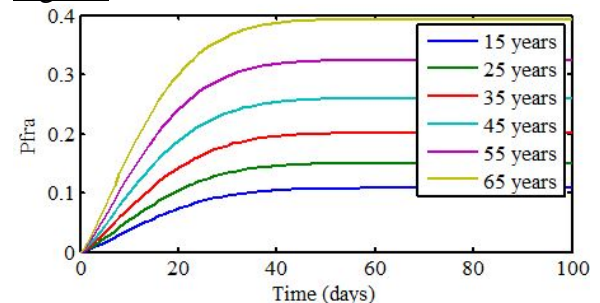


Figure 1:  $P_{fra}$  for different ages running at 3.5 m/s for 5 miles/day.

## Effect Of Counterface On Cartilage Boundary Lubricating Ability By Hyaluronan And Proteoglycan 4: Cartilage-Cartilage vs Cartilage-Glass

Allison McPeak<sup>1</sup>, Saleem Abubacker<sup>2</sup>, Tannin Schmidt<sup>1,3</sup>

<sup>1</sup>Faculty of Kinesiology, <sup>2</sup>Biomedical Engineering Graduate Program, <sup>3</sup>Schulich School of Engineering  
University of Calgary

### Introduction

Proteoglycan 4 (PRG4), also known as lubricin, is a mucin-like glycoprotein found in synovial fluid (SF) [1]. Hyaluronan (HA) is another constituent of SF that works synergistically with PRG4 to promote joint lubrication required for joint health [2]. Current *in vitro* friction tests used to analyze these lubricants have found similar trends but varying friction coefficient ( $\mu$ ) magnitudes. These effects may be attributed to different testing protocols, and in particular the various interfaces [3,4,5,6,7,8]. However, previous studies with synthetic counterfaces may not show the physiological interactions in a synovial joint. The objective of this study was to determine HA and PRG4's lubricating ability at cartilage-glass and cartilage-cartilage biointerfaces at various velocities.

### Methods

HA (1.5 MDa, Lifecore Biomedical) was prepared at 3.3 mg/mL with phosphate buffered saline (PBS) [9]. PRG4 was purified from media conditioned bovine cartilage explants, and prepared at 450  $\mu$ g/mL in PBS [9]. Two sets of tests were conducted using a modified boundary lubrication test protocol [7]. For cartilage-glass, a 6mm radius glass piece, with a root mean square surface roughness of  $6.061 \pm 0.755$  nm, acted as the base core with a cartilage annulus [7]. Three lubricants were tested over three days, PBS (n=8), HA or PRG4 (n=4), and SF (n=8). Cartilage-cartilage underwent the same test sequence. Samples were compressed to 18% of the total cartilage thickness with a 40 minute stress relaxation [9]. Samples were then rotated at effective sliding velocities of 10, 3, 1, 0.3, 0.1, and 0.01 mm/s with a 120s pre-sliding duration. Kinetic  $\mu$  was calculated with instantaneous ( $\langle \mu_{kinetic} \rangle$ ) load values. A two-factor ANOVA was used

to determine effects of lubricant and velocity, with Tukey post-hoc testing.

### Results

At the cartilage-glass interface (**Fig. 1A**),  $\langle \mu_{kinetic} \rangle$  varied with test lubricant and velocity ( $p < 0.001$ ), with no interaction ( $p = 0.78$ ). All lubricants were significantly different from each other ( $p < 0.001$ ), except for PBS/HA ( $p = 0.65$ ) and PRG4/SF ( $p = 0.72$ ). At the cartilage-cartilage interface (**Fig. 1B**),  $\langle \mu_{kinetic} \rangle$  varied with test lubricant and velocity ( $p < 0.01$ ), with no interaction ( $p = 0.82$ ). All lubricants were significantly different from each other ( $p < 0.01$ ), except for HA/SF ( $p = 0.07$ ) and HA/PRG4 ( $p = 0.35$ ).

### Conclusions

These results indicate that different articulating interfaces can result in different trends of  $\langle \mu_{kinetic} \rangle$ , and also affect the magnitude of the value. This agrees with previous research; showing that stiff and impermeable surfaces versus hydrated and permeable surfaces results in different  $\langle \mu_{kinetic} \rangle$  [3]. This data illustrates that HA is indeed a cartilage boundary lubricant and reduces friction at the cartilage-cartilage interface, but not at a cartilage-glass set up.

### References

- Swann+ JBC'81,
- Teeple+ AM J Sports Med'11,
- Dunn+ Tribo Lett'14,
- Jay+ A&R'07,
- Jay+ Connect Tissue'92,
- Gleghorn+ J Biomech'08,
- Schmidt+ OAC'07,
- Davis+ JBiomech Eng'78,
- Schmidt+ A&R'07

### Figures

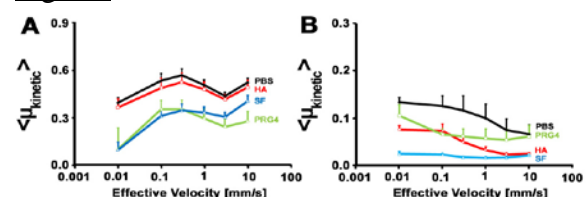


Figure 1: Average kinetic coefficient of friction  $\langle \mu_{kinetic} \rangle$  of (A) cartilage-glass and (B) cartilage-cartilage.

## Development of a Balance Assessment Tool (BAT) for a Computer-Assisted Rehabilitation Environment

Quinn Boser<sup>1,2</sup>, Jacqueline S. Hebert<sup>2,3</sup>, Albert H. Vette<sup>1,2</sup>

1. Department of Mechanical Engineering, University of Alberta; 2. Glenrose Rehabilitation Hospital, Alberta Health Services; 3. Faculty of Rehabilitation Medicine, University of Alberta

### Introduction

Postural control during standing and walking is a serious challenge for many clinical populations. As such, injurious falls present a prevalent health problem, and pose a large economic burden on our health care system. Because of this, working to reduce balance problems and build confidence is an important clinical goal. The CAREN system housed in the Glenrose Rehabilitation Hospital (GRH) is a “Computer-Assisted Rehabilitation ENvironment” which uses virtual reality, a robotic platform, and motion capture capability for the assessment and treatment of patients with balance and mobility problems (Fig. 1A). Although the CAREN system is frequently used to complement standard patient care, quantitative methods for assessing patient progress following traditional or CAREN treatment are lacking. Therefore, the purpose of this project was to develop a base module for a balance assessment tool (BAT) that can be used on the CAREN system.

### Methods

In the first phase of the project, a battery of postural tasks has been implemented in the CAREN software that can serve as the BAT base module. The chosen tasks were based on standard clinical protocols for assessing balance abilities [1] and included the *Sensory Organization Test* (SOT) and the *Limits of Stability Test* (LOS). Both of these tests are currently performed on the NeuroCom SMART EquiTest System at the GRH (Fig. 1B). In the second phase of the project, a validation study with 15 young and healthy participants is currently underway to evaluate whether the SOT and LOS can be reliably administered on the CAREN system. If this is the case, a normative set of SOT and LOS outcome measures will be identified for the base module of the CAREN BAT.

### Results

The table lists the equilibrium score (%), the main SOT outcome measure, for our first study participant (EquiTest and CAREN systems). It can be seen that the performance on the two systems was comparable for most SOT conditions, with the largest discrepancy occurring for condition 6, challenging both visual and somatosensory feedback.

SOT condition	EquiTest	CAREN
	Mean $\pm$ standard deviation (n=3)	
1	96 $\pm$ 1 %	94 $\pm$ 1 %
2	95 $\pm$ 1 %	91 $\pm$ 3 %
3	97 $\pm$ 1 %	95 $\pm$ 2 %
4	95 $\pm$ 0 %	88 $\pm$ 2 %
5	86 $\pm$ 3 %	78 $\pm$ 4 %
6	95 $\pm$ 4 %	86 $\pm$ 4 %

### Conclusions

A base module for the CAREN BAT has been developed that consists of two standard balance assessment tools. Currently, we are assessing its validity in healthy subjects, with the goal of identifying a set of normative measures. Once this study is complete, the BAT will be expanded beyond the base module, making use of the wide range of CAREN capabilities.

### References

Tesio et al. International Journal of Rehabilitation Research 2013;36:362-374.

### Figures

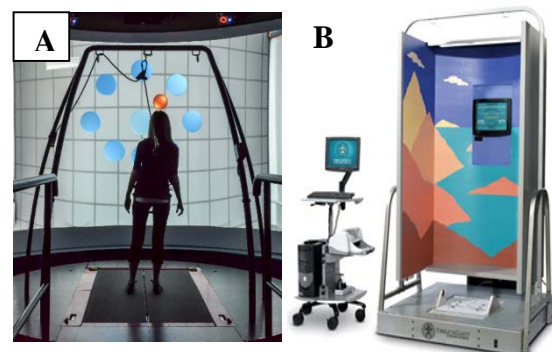


Figure 1: CAREN (A) and EquiTest (B) systems.

## **A research proposal about the association between the development of osteoarthritis and changes in the relative velocity of joint surfaces following Anterior Cruciate Ligament (ACL) and Medial Collateral Ligament (MCL) transection**

S. M. M. Shekarforoush, MSc, M. Atarod, PhD, C. B. Frank, MD, D. A. Hart, PhD, N. G. Shrive, D.Phil.  
McCaig Institute for Bone and Joint Health, Faculty of Medicine, University of Calgary

### Introduction

Post Traumatic OsteoArthritis (PTOA) is a sub-type of osteoarthritis, which can develop after injury to the joint. It is widely accepted that alterations to joint kinematics following injury are one of the main causes of subsequent cartilage damage, and the development of OA. More recently, it has been suggested that changes in joint relative surface velocity correlate more consistently with cartilage damage after joint injury [1-2]. This idea developed from the fact that frictional (shear) forces are related to the relative velocity of the contacting surfaces. The idea would be supported if the direction of the fibers (split line orientations) in the cartilage surface is aligned with the direction of average local frictional force in normal gait. One aim of this project is to investigate this subject.

### Hypothesis

ACL/MCL transection in sheep causes small but significantly abnormal variation in tibio-femoral relative surface velocity leading to damage of the cartilage surfaces.

### Objectives

This hypothesis will be evaluated by the following specific objectives: 1) Measure the relative motion of the femur with respect to the tibia before and after ACL/MCL transection; 2) Determine the 3D shape of the femur and tibia; 3) Determine the split line orientation of the cartilage and map this onto the 3D shapes; 4) Determine the loci of focal cartilage damage 52 weeks after injury and map onto the 3D bone shapes; 5) Assess any correlations.

### Methods

Five skeletally mature female Suffolk-cross sheep (N=5) will be trained to walk on a standard treadmill. Stifle joint kinematics will be measured before and 4, 20 and 52 weeks after arthroscopic surgery, where the

ACL and MCL are fully transected [3]. The animals will be sacrificed at 52 weeks: 3D data of the joint will be obtained from MRI. Software will be developed to calculate the relative velocity of the joint surfaces by defining an appropriate joint coordinate system. Cartilage split line orientations and focal damage locations will be digitized using a coordinate measuring machine. Split lines will be defined with india ink staining of "holes" in the cartilage surface, made with a needle [4]. The 3D locations of split lines and sites of damage will be mapped onto the MRI images. The average change in relative surface velocity during the stance phase of gait, due to injury, will be mapped onto the same images and any correlations between the surface velocity changes, the split line orientations and the damage will be determined.

### Expected Outcomes:

It is expected that both the magnitude and direction of the relative surface velocities will be significantly changed in all experimental subjects, with considerable inter-subject variability. Also, we expect that changes in velocity directions are more consistent with the cartilage damage.

### Significance

These experiments will provide new information about changes in relative surface velocity of the knee joint following injury, their correlation with the location of focal lesions, and potential biomechanical drivers of PTOA.

### References

- [1]. Jillian E. Beveridge, et al., J Orthop Res. 31(11):1745-56, 2013.
- [2]. William J. Anderst, et al., Inc. J Orthop Res. 27:71-77, 2009.
- [3]. Mohammad Atarod, et al., Ann Biomed Eng. 42 (5), p1121, 2014.
- [4]. Steven Below, et al., J. Arth. Rel. Surg, 18 (6), 613-617, 2002.

## Parameters of Thalamic DBS and Motor Cortical Perfusion

Muhammad S. Noor<sup>1,2</sup>, Clinton B. McCracken<sup>1</sup>, Kartikeya Murari<sup>2</sup> and Zelma H.T. Kiss<sup>1</sup>

<sup>1</sup> Department of Clinical Neurosciences, University of Calgary, <sup>2</sup> Department of Electrical and Computer Engineering, University of Calgary

### Introduction

Deep brain stimulation (DBS) applied in ventrolateral (VL) thalamus stops tremor [1]. VL thalamus projects to and receives major input from the primary motor cortex (M1) [2]. Previous studies of effective DBS in tremor patients suggest that DBS increases regional cerebral blood flow in M1 [3]; however, no systematic studies have described how various DBS parameters alter motor cortical perfusion. Here we examined how different parameters of thalamic DBS affect M1 perfusion in normal, urethane-anesthetized rats.

### Methods

Because optical properties of brain tissue are correlated with cortical perfusion [4], we used intrinsic optical imaging after thinning the skull over M1. A CCD camera and blue (~450 nm) illumination were used for the imaging.

Next, we implanted a bipolar concentric electrode into VL thalamus while imaging M1. After 10 sec of baseline imaging, biphasic, constant current stimulation was delivered for 10 sec using different combinations of frequencies (20, 100, 200, 350 Hz), pulse widths (0.05, 0.2 and 0.5 ms) and amplitudes (0.2, 0.4, 0.7 mA). Imaging continued for 160 sec after the end of stimulation. The maximum change in the reflectance data, normalized separately for each trial using the 10-s baseline data, was compared across different trials.

### Results

Initially, we confirmed that electrical stimulation has no direct, non-neural-mediated effects on blood vessels. Epidural electrical stimulation, which altered M1 perfusion at baseline, had no effect in the presence of tetrodotoxin, which blocks

neuronal activity but does not affect vascular smooth muscle.

We found that DBS reduced cortical light reflectance, indicating increased M1 perfusion. Higher pulse widths and amplitudes evoked larger increases in tissue perfusion, while frequencies greater than 100 Hz produced negligible increases. Repeated measures ANOVA revealed significant main effects of amplitude, pulse width, and frequency ( $p < 0.001$ ) on cortical perfusion, but no significant interactions ( $p > 0.089$ ). Post-hoc testing showed that all three levels of amplitudes and pulse widths had different effects ( $p < 0.006$  and  $p < 0.02$  respectively), however only the 20 Hz frequency differed from other frequencies ( $p < 0.025$ ). Using regression analysis, 67% of the variability in perfusion was predicted by charge per pulse, while adding frequency as a second predictor accounted for 71% of the variability.

### Conclusions

In conclusion, optical imaging allowed reliable measurement of the remote effects of thalamic DBS on the motor pathway involved in tremor. The amplitude and pulse width of DBS, meaning the charge per pulse, had a much greater effect on perfusion than frequency. This has important implications for programming, mechanisms of action, and design of DBS systems.

### References

- [1] A. L. Benabid, *et al.*, *Journal of Neurosurgery*, vol. 84, pp. 203-214, Feb 1996.
- [2] F. Cicirata, *et al.*, *Neuroscience*, vol. 19, pp. 81-99, 1986.
- [3] A. O. Ceballos-Baumann, *et al.*, *Neurology*, vol. 56, pp. 1347-1354, 2001.
- [4] A. Grinvald, *et al.*, *Nature*, vol. 324, pp. 361-364, 1986.

## PCL/Gelatin nanofiber mats for grafting human skin-derived precursor cells (hSKPs) into skin wounds

Fraz Anjum<sup>1</sup>, Jeff Biernaskie<sup>2</sup>, Michael S Kallos<sup>1</sup>

<sup>1</sup> Pharmaceutical Production Research Facility, University of Calgary, 2500 University Dr. Calgary AB T2N 1N4 Canada

<sup>2</sup> Department of Comparative Biology and Experimental Medicine, Faculty of Veterinary Medicine, University of Calgary 3330 Hospital Dr. Calgary, AB, T2N 4N1 Canada

### Introduction

Appropriate porosity, pore size, surface properties and mechanical integrity are fundamental characteristics of scaffolds intended for application in tissue engineering and regenerative medicine. Ideally, materials that best mimic the endogenous architecture and ECM composition will yield the best outcome [1]. Electrospun woven nanofibers address many of the above mentioned characteristics, which lead us to investigate the potential utility of nanofibrous scaffolds specifically for skin wound management [2-5]. The purpose of the current study is to investigate the potential of PCL and PCL/gelatin nanofibers as carriers for adult human skin-derived precursors (hSKPs) transplanted into skin wounds.

### Methods

After determination of appropriate solvent system, Poly( $\epsilon$ -caprolactone) and gelatin type B are electrospun using an in-house electrospinning set up. PCL nanofiber mesh was immobilized with GRGDS peptide for enhanced cell attachment. The nanofibers obtained were characterized with FT-IR for relative composition of the two polymers and Scanning Electron microscopy (SEM) for fiber morphology. The tensile testing was performed using BOSE Electroforce. The nanofiber meshes were sterilized and subsequently seeded with hSKPs. The cells were seeded at 20,000 cells/scaffolds.

### Results

The fiber morphology of PCL/gelatin nanofibers were characterized through SEM and images were analyzed using ImageJ. SEM image of PCL nanofibers is shown in Fig. 1a. The average diameter of fibers was found to be  $5.46 \pm 0.845 \mu\text{m}$  and pore size was  $2.54 \pm 0.742 \mu\text{m}$ . The tensile strength of pure PCL nanofibers is quite high ( $\sim 10 \text{ MPa}$ ) and a significant decrease in tensile strength was

observed with increasing percentage of gelatin. Cell seeding results showed the cell attachment onto RGD immobilized PCL was significantly higher than PCL. SEM image of cell-seeded PCL-RGD nanofiber mesh is shown in Fig. 1b,c indicating the intact morphology of cells showing cell processes, which was further confirmed by staining the scaffolds with phalloidine/rhodamine and counterstained with Hoechst and visualized under confocal scanning microscope shown in Fig. 1d.

### Conclusions

The nanofibers of PCL-RGD showed enhanced cell adhesion and spread morphology of cells thus presenting a potential substrate for hSKPs transplantation into skin wounds.

### References

1. Ma Z W *et al.* 2005, *Tissue Eng.* 11, 101–109.
2. Miller D C *et al* J 2004 *Biomaterials* 25, 53–61.
3. Lannutti J, 2007 *Mater. Sci. Eng. C.* 27, 504–509.
4. Xu C Y, 2004. *J. Biomed. Mater. Res. A* 71A 154–161.
5. Taepaiboon P, 2006 *Nanotechnology* 17, 2317–2329.

### Figures

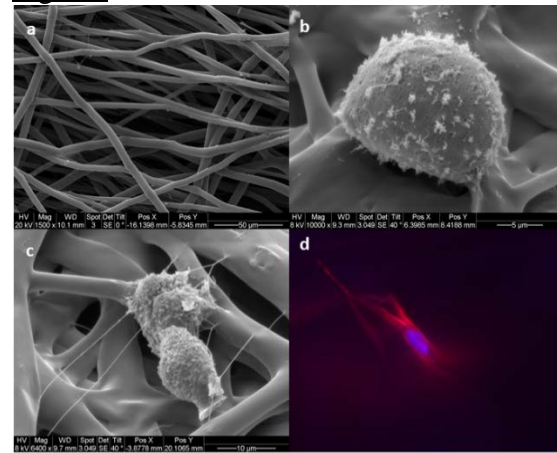


Figure 1: a) SEM of PCL nanofibers, b) hSKPs attached to PCL 2 h post seeding, c) 24 h post seeding, d) confocal image of PCL-RGD showing actin (phalloidine) and nucleus (Hoechst).

## Clinical Validation of Center of Mass using Surface Topography in Adolescent Idiopathic Scoliosis

Alexandra Melia<sup>1</sup>, Jessica Kupper<sup>2</sup>, Gulshan Sharma<sup>2</sup>, Dr. Elaine Joughin<sup>3</sup>, Dr. James Harder<sup>3</sup>, Dr. Janet Ronsky<sup>2</sup>

1. Biomedical Engineering, University of Calgary 2. Mechanical and Manufacturing Engineering, University of Calgary 3. Department of Orthopedic Surgery, Alberta Children's Hospital

### Introduction

One in 200 adolescents have idiopathic scoliosis (AIS) [1], a significant bending in the spine that is always accompanied by rotation of the vertebrae. Currently, AIS is monitored and diagnosed using full spinal 2D X-rays and the Cobb angle [2] to measure the severity of the curve. This method cannot account for 3D changes of the spinal deformity [3] and exposes patients to cumulative high doses of radiation, increasing their risk of cancer [4]. This has motivated the development of imaging systems that use Surface Topography (ST) to reconstruct 2D or 3D models of the torso. The external body shape is then quantified through various ST measures. Attempts have been made to correlate ST measures directly to the Cobb angle. This approach is limited, as the Cobb angle only measures one aspect on one plane of the 3D deformity. To overcome this limitation, previous studies in our group have evaluated ST measures in progressed and non-progressed AIS patient groups to determine their clinical relevance using the minimum detectable change (MDC) and minimum clinically important difference approaches (MCID;[5]). The MDC approach determines the reliability of ST measures, and the MCID provides a clinically relevant change against which the MDC can be evaluated.

One ST measure that has not been fully explored in AIS literature is Center of Mass (COM). COM shows to be a promising measure as previous studies have shown significant differences in COM between scoliosis and normal groups using force plates [6]. The goal of the ST measure, COM, is to describe the ST-based decompensation of the trunk as a whole in the sagittal and coronal plane. The objective of this study is to determine if the ST measure, COM, is clinically applicable for detecting and monitoring AIS progression. This will be investigated through the

following hypothesis: The ST measure, COM, can detect changes smaller than those that are clinically significant (i.e MDC will be smaller than MCID calculated for this measure).

### Methods

Using standardized protocol [7] and the novel 26-camera system [8] torso ST data will be collected at the ACH in Calgary, Alberta (15 AIS at 1 time for MDC; 40 AIS at 2 or 3 times for MCID). Subjects will be 8-18 years old with AIS and no previous spinal injury. COM will be calculated using in-house software. To test the hypothesis, the MDC will be calculated for COM, and will be validated for clinical relevance using the MCID (defined as the average of within subject change scores in the progressed group). For COM to be clinically applicable, the measure must detect changes in the torso that are smaller than those that are clinically relevant (i.e MDC must be less than the MCID of COM). Details of these techniques will be presented.

### Conclusions

COM is promising as a ST measure, as it has the ability to describe the decompensation of the trunk as a whole. The MDC and MCID approach shows promise to clinically evaluate ST measures as it groups patients using the clinical standard of care rather than directly correlating the measures to the Cobb angle. Clinically relevant ST measures have the potential to give clinicians reliable and quantifiable non-radiographic information that they currently lack.

### References

1. Kane: Clin Orthop Relat Res 1977:43–6.
2. Adams W: Lectures on the pathology and treatment of lateral and other forms of curvature of the spine 1865.
3. Goldberg et al.: Spine 2001, 26:E55–63.
4. Levy et al: Spine 1996, 21:1540–1548.
5. Dubetz et al: University of Calgary; 2012.
6. Park et al: Journal of Physical Therapy Science 2013, 25(12), 1629–31.
7. Dubetz et al: In *Proc Elev Annu Sci Conf Can Spine Soc*. Quebec, City; 2011. 8.
8. Detchev et al.: GEOMATICA 2011, 65:175-187

## Muscle Morphology of the Spastic Mice

Maria Engel, Tim Leonard, and Walter Herzog  
Human Performance Laboratory, University of Calgary  
2500 University Drive NW, Calgary, AB, T2N 1N4

### Introduction

Cerebral Palsy (CP) is a disease caused by non-progressive lesions in the brain, typically occurring at birth. It is often associated with spasticity of skeletal muscles causing characteristic structural changes. Specifically, human spastic muscles have been shown to have shorter fibres and greatly elongated sarcomeres causing increased passive forces<sup>1</sup>. This leads to a decreased range of motion about a joint, also known as hypoextensibility. The spastic mouse<sup>2</sup> may provide a useful animal model for studying spastic muscles and their resulting hypoextensibility. Spastic mice have been shown to have a decreased muscular growth rate compared to non-spastic mice<sup>3</sup>. Understanding this lack of growth may give an insight to the mechanisms of hypoextensible muscles in CP. However, muscle characteristics such as fibre and sarcomere length have not been quantified in the spastic mouse. Therefore, the purpose of our study is to examine gross muscle characteristics, as well as fascicle length, sarcomere length, and sarcomere numbers.

### Methods

Mice were bred for spasticity at the University Hospital of Würzburg. Spastic (n=4) and age-matched non-spastic (n=7) mice were selected for skeletal muscle analysis. Animals were weighed, and then sacrificed at 18-20 days old. The lower half of the body was placed in 10% formalin for a duration of at least 3 weeks. The knee and ankle joints were pinned at 90°. The Lateral Gastrocnemius (LG) muscle, Achilles tendon, and tibia lengths were measured using india ink and a custom computer software (Matrox Inspector). The Soleus, Plantaris, Extensor Digitorum Longus, Rectus Femoris, Gracilis, and Adductor Magnus were dissected and placed in nitric acid to digest the connective tissue. Individual muscle fascicles were then placed

on slides for fascicle length, sarcomere length, and sarcomere number analysis. Fascicle lengths were measured using Matrox Inspector, and sarcomere lengths were measured using laser diffraction. Sarcomere numbers were calculated by dividing fascicle length by the average sarcomere lengths.

### Results

The average weight of the non-spastic mice was  $7.8 \pm 0.9$ g, while the average weight of spastic mice was significantly smaller at  $5.6 \pm 0.6$ g ( $p < 0.01$ ). The LG muscle was significantly shorter ( $p < 0.01$ ) in the spastic mouse than the non-spastic. Additionally, when normalized to the tibia (LG length/Tibia length), there was still a significant difference between the two groups.

Fascicle length, sarcomere length, and sarcomere number results are pending.

### Conclusions

With normalization, the LG muscle length is shorter in the spastic mouse. This suggests a lack of muscle growth.

### References

1. Foran et al (2007) Structural and Mechanical Alterations in Spastic Skeletal Muscle. *Developmental Medicine & Child Neurology*, (47) 713-717.
2. Chai, CK (1961) Hereditary Spasticity in Mice. *Journal of Heredity*, 52(5) 241-243.
3. Ziv et al (1984) Muscle Growth in Normal and Spastic Mice. *Developmental Medicine & Child Neurology*, (26) 94-99.

### Acknowledgements:

CIHR, NSERC, The Killam Foundation and the Canada Research Chair Programme.

## Classification of Brain White Matter Lesion on MR Imaging

Mariana Leite,<sup>1,3</sup> Leticia Rittner,<sup>1</sup> Aline Lapa,<sup>2</sup> Simone Appenzeller,<sup>2</sup> Roberto Lotufo<sup>1</sup>

<sup>1</sup>Faculty of Electrical Engineering and <sup>2</sup>Medical Science, University of Campinas, Brazil

<sup>3</sup>Calgary Image Processing and Analysis Centre (CIPAC), University of Calgary/Foothills Medical Centre, Canada

### Introduction

Brain white matter lesions (WMLs) found on MR images are commonly observed in psychiatric or neurological patients [1]. Though the etiology of WMLs is often difficult to determine due to a lack of pathological studies, they are likely to be of either ischemic or demyelinating origin [2]. This work proposes a computerized method to distinguish tissue-containing WMLs of demyelinating or ischemic etiologies from normal white matter (nWM) using texture-based classifiers.

### Methods

Two-dimensional T2-weighted axial MR images were collected at the Faculty of Medical Science of the University of Campinas. Manually segmented regions were drawn by an expert. Seventy-six (76) regions of nWM, 143 regions of WML with demyelinating etiology (dWML), and 64 regions of WML with ischemic etiology (iWML) were extracted based on patient pathology. Seventy-four (74) texture attributes, computed based on histogram, gray level co-occurrence matrix, run-length matrix and intensity gradients [3], were extracted from each region. A support-vector machine (SVM) classifier [4] was trained to distinguish regions containing nWM from dWML and iWML. Experiments were conducted to distinguish: a) normal WM from WML (lesion-no lesion task), b) WML based on their etiology (demyelinating-ischemic task), and c) between the three classes (nWM, dWML, iWML, normal-demyelinating-ischemic task). All algorithms were implemented in the Python language, and were developed on Adessowiki [5], a web-based collaborative environment for development and documentation of computing algorithms.

### Results

An example classification is shown in Figure 1. An accuracy rate of  $99.29\% \pm 0.01\%$  was achieved for the lesion-no lesion task,  $86.50\% \pm 0.09\%$  for demyelinating-ischemic task, and  $90.09\% \pm 0.05\%$  for normal-demyelinating-ischemic task. The confusion matrix of normal-demyelinating-ischemic task was calculated (Table 1).

Table 1: Evaluation of the quality of the SVM classifier output when performing normal-demyelinating-ischemic task.

Actual Class	Predicted Class		
	nWM	dWML	iWML
nWM	76/283	0/283	0/283
dWML	1/283	132/283	10/283
iWML	0/283	17/283	47/283

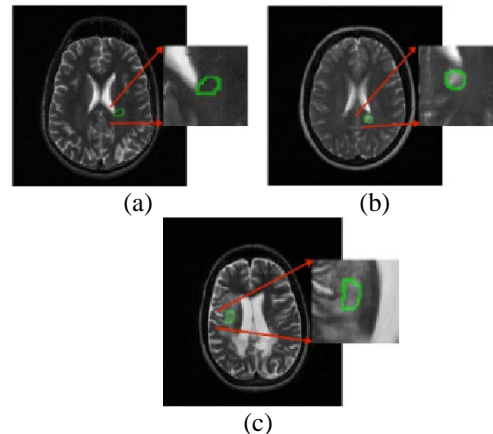


Figure 1: Region classified as (a) normal white matter (nWM), (b) demyelinating WM lesion (dWML), and (c) ischemic WML (iWML).

### Conclusions

We have shown that the combination of texture analysis and SVM classifier is able to distinguish tissue-containing WML of different etiology (*e.g.*, demyelinating or ischemic) from nWM. We tested two approaches to improve classification to distinguish nWM, dWML, and iWML in: a) a single step (normal-demyelinating-ischemic task) and b) separate steps (lesion-no lesion and demyelinating-ischemic tasks). The most difficult classification was the demyelinating-ischemic task, since it yielded the lowest accuracy rate. We intend to validate these results in a larger database, including images acquired at different centers, and three-dimensional MR images.

### References

- [1] Kloppenborg, *et al. Neurology* 2014; 82: 2127.
- [2] Kim, *et al. Biological Psychiatry* 2009; 64: 273.
- [3] Gonzalez and Woods. *Digital Image Processing* 2008.
- [4] Cortes and Vapnik. *Machine Learning* 1995; 20:273.
- [5] Lotufo, *et al. 5th International Symposium on Wikis and Open Collaboration* 2009.

## An Examination of Sarcomere Length Non-Uniformities in Actively Stretched Muscle Myofibrils

Kaleena Johnston, Azim Jinha, & Walter Herzog  
Human Performance Laboratory, Faculty of Kinesiology, University of Calgary

### Introduction

Residual force enhancement (RFE) is a characteristic of skeletal muscle describing the increase in isometric steady-state force following an active stretch (force-enhanced, FE), compared to the force of an isometric contraction at the final length (purely isometric, PI) [1]. It has been suggested that RFE is a result of sarcomeres along a single myofibril becoming more non-uniform in length after an active stretch due to instability on the descending limb of the force-length relationship [2]. Previous research, however, has reported an inherent stability of sarcomeres following active stretching. While this contradicts earlier hypotheses, it is still unclear whether sarcomere length non-uniformities play a role in the development of RFE. Therefore, the purpose of this study was to investigate the hypothesis that sarcomere length non-uniformities would increase from the PI state to the FE state.

### Methods

Isolated rabbit psoas myofibrils were stretched passively to an average sarcomere length along the descending limb of the force length relationship [3]. Myofibrils were then activated. Five seconds after full activation, they were rapidly shortened, held for ten seconds, and then stretched back to the original length [4]. Individual sarcomere lengths and force were determined throughout the protocol and were used to identify steady state PI and FE conditions (Figure 1). Standard deviations (SDs) of the mean sarcomere lengths in each state were compared to analyze non-uniformity.

### Results

Myofibril ( $n = 7$ ) forces increased from the PI state ( $122 \pm 62$  nN) to the FE state ( $161 \pm 71$  nN), showing  $38 \pm 34$  % RFE ( $p = 0.02$ ). Mean SDs were  $0.5$   $\mu\text{m}$  and  $0.8$   $\mu\text{m}$  for the PI and FE states, respectively. These values were significantly different ( $p = 0.03$ ).

### Conclusions

While statistical analyses of the current results suggest that non-uniformity may play a role in the phenomenon of RFE, two of the seven myofibrils did not show an increase in sarcomere length non-uniformity. In one, sarcomere length non-uniformity remained the same and in the other, it decreased. Despite this, both of these myofibrils demonstrated RFE: 97% and 20%, respectively. Due to this contradicting evidence, it is possible that while the development of sarcomere length non-uniformities may play a role in RFE, other mechanisms may also be occurring. Therefore, in the immediate future, we will increase the sample size of the current project and will investigate other possible mechanisms contributing to RFE.

### References

- [1] Gordon, AM, et al., *Journal of Physiology*, 184, pp, 170-192, 1966.
- [2] Morgan, DL, *Biophysical Journal*, 57, 209-221, 1990.
- [3] Herzog, W, et al., *Molecular and Cellular Biomechanics*, pp, 25-31, 2010.
- [4] Rassier, DE, et al., *Journal of Biomechanics*, 37, 1305-1312, 2004.

### Figures

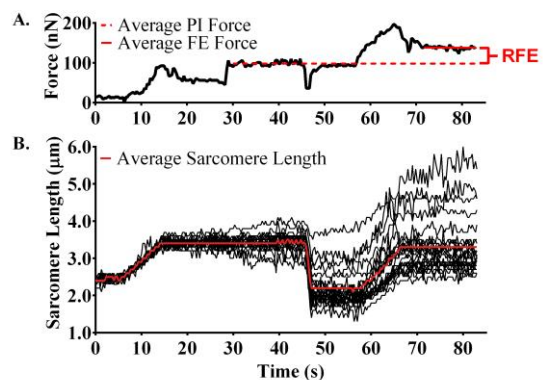


Figure 1. Results from one of the myofibrils indicating the force (A) and the lengths (B) of each individual ( $n = 23$ ) sarcomere along the myofibril throughout the experiment. Red lines on each graph indicate average values. This example demonstrates 40% RFE and an increase in sarcomere length non-uniformity from  $0.2$   $\mu\text{m}$  to  $0.8$   $\mu\text{m}$ .

## Evaluation of Primary Elbow Osteoarthritis using High-Resolution Peripheral Quantitative Computed Tomography: An Exploratory Study

Katherine Archibold, Sarah Manske, Kevin Hildebrand, Steven Boyd  
McCaig Institute for Bone and Joint Health, University of Calgary, Calgary, AB Canada

### Introduction

Osteoarthritis (OA) is a degenerative joint disease characterized by morphological and histological changes of bone and cartilage. A feature of this disease is the development of osteophytes, which alter the structure of the bone. Bony changes are especially common in the olecranon fossa of the humerus [1].

Primary OA of the elbow has a unique disease progression. To the best of our knowledge, prior to this study microarchitectural changes in primary elbow OA have never been examined. With second-generation high-resolution peripheral quantitative computed tomography (HR-pQCT) scanners, images of the elbow *in vivo* can now be obtained. This project involved establishing a scanning protocol appropriate for this population and anatomical region to explore the relation of primary elbow OA with the underlying bone structure. Examining the microarchitectural features will provide new insight into the pathophysiology of this disease.

### Methods

Two male subjects with OA (aged 47 & 50) and four age and gender matched healthy controls (aged 36-59) were recruited. Elbow pain and function were recorded using the PREE questionnaire [2]. Image data of the subjects' dominant humerus were acquired using a HR-pQCT scanner (XtremeCTII; Scanco Medical). To minimize movement, subjects were instructed remain still and their arms were immobilized using a custom-made, padded, carbon fibre support. A scout view ensured the region of interest was correctly defined by a trained operator to ensure the entire region of interest was scanned. A 40.79 mm scan consisting of 672 slices were obtained to capture the distal humerus including the olecranon fossa (Figure 1) using a custom protocol derived from the manufacturer's standard for other anatomical regions (61µm nominal isotropic voxel size, 43ms integration time, 900 projections). Images were contoured to segment the bony region of interest and evaluated using Image Processing Language (v5.15, Scanco Medical).

### Results

A scan protocol consisting of a single scan of four stacks was determined to be most appropriate for this population to minimize scan duration (15min) and movement while still capturing the area of interest. However, motion artifacts were problematic in some scans. The resulting images showed great variability in the anatomy of the fossa.

### Conclusions

Prior to this study, *in vivo* HR-pQCT images of the elbow have never been obtained. Through this pilot project a scan protocol to capture the olecranon fossa of the humerus was developed for the first time.

The variability in the anatomy of the region presents challenges in isolating the area of interest, thus making quantitative analysis of microarchitecture complex. Future work includes scanning additional subjects and finalizing how to isolate the olecranon fossa to enable quantitative analysis of bone microarchitecture in this region. Studying this region will increase our understanding of the pathophysiology of OA and open new exciting research opportunities.

### References

1. Adla & Stanley. *Shoulder Elbow*. **3(1)**:41-48, 2011.
2. MacDermid. *J Hand Ther*. **14(2)**:105-114, 2001.

### Figure



**Figure 1.** A 3-dimensional reconstructed HR-pQCT image of posterior aspect of the humerus showing the olecranon fossa.

## HR-pQCT FE derived bone strength differentiates between older women with and without recent distal radial fracture

Morteza Amini<sup>1</sup>, Chantal E. Kawalilak<sup>2</sup>, Cathy M. Arnold<sup>3</sup>, Saija A. Kontulainen<sup>2</sup>, James D. Johnston<sup>1</sup>

<sup>1</sup>Mechanical Engineering Department, University of Saskatchewan, Saskatoon, SK, Canada

<sup>2</sup>College of Kinesiology, University of Saskatchewan, Saskatoon, SK, Canada

<sup>3</sup>College of Medicine, University of Saskatchewan, Saskatoon, SK, Canada

### Introduction

Osteoporosis is a systemic skeletal disease characterized by low bone mass and microarchitectural deterioration of bone tissue, with a consequent increase in bone fragility and susceptibility to fracture [1]. Distal radius fractures (DRF) are the most common osteoporotic fracture in women and an important predictor of other osteoporotic fractures [2]. The primary clinical diagnostic tool for osteoporosis (DXA) has proven incapable of predicting risk of DRF, probably due to the microarchitectural deterioration of bone tissue that is not detectable by DXA [3]. High resolution peripheral quantitative computed tomography (HR-pQCT) provides information of distal radius microarchitecture that can be applied to Finite Element (FE) analysis to estimate distal radius strength (i.e., mechanical properties such as failure load, stiffness, stress distribution). The aim of this study was to compare bone mechanical properties at the wrist measured with HR-pQCT FE method in postmenopausal women with and without a recent distal radius fracture.

### Methods

We recruited 76 postmenopausal women (mean age 65, SD 8 years) from local clinics and through advertisement. Participants with a recent DRF (6-24 months post-fracture) (Fx, N=31) served as cases and age- and size-matched participants with no history of DRF (Nonfx, N=45) as controls. We measured non-fractured wrist in cases and non-dominant wrist in controls. We used XtremeCT (HR-pQCT) to scan 9.5 mm region of interest of distal radius of each participant (Fig. 1). Each scan consisted of 110 slices with 82-micron resolution. We used a semi-automatic slice by slice segmentation method to build the 3D reconstruction of the scanned section for each subject (Fig. 1). Voxel-based, isotropic,

linearly elastic micro-FE model of each volume using a global threshold to separate soft tissue from the bone and 8-node brick elements were developed (Fig. 1). Bone elastic modulus (E) was set to 20 GPa with Poisson's ratio of 0.3 [4]. FE-based failure load using Pistoia's criteria [5], overall stiffness of the distal radius, and maximum and average von Mises stresses were compared between the Nonfx and Fx groups using multivariate analysis of variance followed by pairwise comparisons with Bonferroni adjustment for multiple comparisons.

### Results

There was a significant group difference (Wilks' lambda 0.874,  $P < 0.05$ ). Pairwise comparison between Fx and NonFx groups showed that the Fx group had 6600 KN/m lower stiffness ( $P < 0.05$ ). There were no significant differences in other FE outcomes.

### Conclusions

Women with recent DRF had 10% lower HR-pQCT FE derived distal radius stiffness. This technique may help to improve the prediction of distal radius fracture risk in postmenopausal women.

### References

[1] Kanis et al., 2002, [2] Cuddihy et al., 1999, [3] Zysset et al., 2013, [4] Vilayphiou, 2010 [5] Pistoia et al., 2002

### Figures

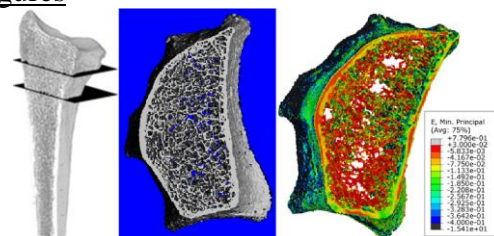


Figure 1) 9.5 mm sections of the distal radius of all participants were scanned. A semi-automatic slice-by-slice segmentation method, with a global threshold, was used to separate bone from soft tissue. The final model was constructed using a single modulus of elasticity for all elements (20 GPa).

## Developing an Optical Measure of in Vivo Mitochondrial Redox Status in Rodent Brain

Daniel Korchinski, Thomas Johnson, Dr. Jeff Dunn

Experimental Imaging Center, Hotchkiss Brain Institute, Faculty of Medicine, University of Calgary

### Introduction

Metabolic dysregulation and hypoxia are implicated in the etiology of many diseases including multiple sclerosis, Alzheimer's, stroke, birth asphyxia, traumatic brain injury, and post-surgical neurological dysfunction. A non-invasive method to monitor oxygenation and mitochondrial status would be useful for these patients. Non-invasive near infrared spectroscopy (NIRS) may provide a solution, as its measured chromophores including oxy- and deoxy-hemoglobin as well as cytochrome C oxidase (COX)<sup>1,2</sup>. COX is of particular use in measuring mitochondrial status, as its redox state is dependent upon electron flux in the mitochondrial electron transport chain and is measurable via NIRS.

This project has the aim of developing a non-invasive NIRS system capable of tracking COX changes in vivo, and applying this to study metabolic disease in animal models.

### Methods

The NIRS system utilized an Andor CCD camera cooled to -40 Celsius and Shamrock SR303i spectrometer to quantify the attenuation of broadband light reflected by the sample. Spectral data were collected between 712 - 985nm at 20Hz.

To account for unknown tissue geometry and scattering effects, a second differential method was employed to extract the differential path length factor for deoxyhemoglobin.

Optical fibre bundles were used to transmit and receive light.

Mice were anesthetized with isoflurane and the head shaved to improve contact between the skin and fibre. Animals were spontaneously ventilating. Gas mixtures were varied using a computer controlled flow regulator. Animals were maintained at 30% inspired O<sub>2</sub>. COX redox status was changed by sacrificing the animal with intraperitoneal injection of 40mg/kg sodium azide bolus, a COX blocker.

### Results

Approximately nine minutes post injection saw the mouse cease spontaneous respiration. This correlates closely with the rapid decrease in the COX signal (Fig. 1) expected from animal death.

### Conclusions

The precipitous decline in COX signal during animal sacrifice validates the dynamic range of our NIRS system. Relative stability of the COX signal before and after respiratory failure suggests the efficacy of the NIRS system. Further validation will be required to prove deconvolution of hemoglobin and COX signals. This system is an important step in tracking metabolic dysregulation in rodent models of injury and disease.

### References

1. Cooper, C. E., & Springett, R. (1997). Measurement of cytochrome oxidase and mitochondrial energetics by near-infrared spectroscopy. *Philosophical Transactions of the Royal Society B: Biological Sciences*, 352(1354), 669–676.
2. D. T., & Cope, M. (1997). Quantification in tissue near-infrared spectroscopy. *Philosophical Transactions of the Royal Society of London. Series B: Biological Sciences*, 352(1354), 649–659.

### Figures

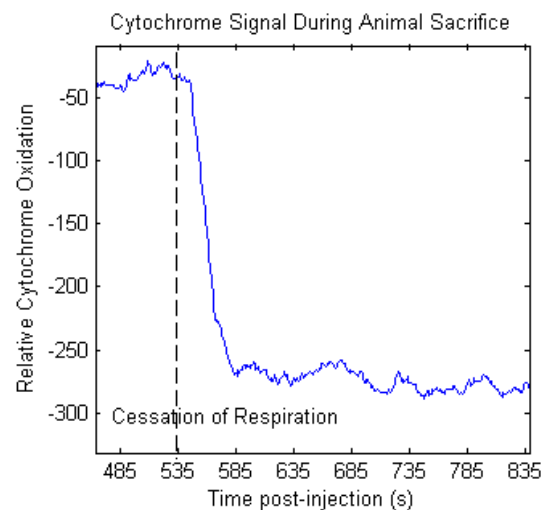


**Figure 1.**

## Clinically Usable Real-Time Simulation of Lumbar Spine Model

Nathaniel K. Maeda<sup>1</sup>, Pierre Boulanger<sup>2</sup>, Jason P. Carey<sup>1</sup>

<sup>1</sup>Department of Mechanical Engineering; <sup>2</sup>Department of Computing Science, University of Alberta

### Introduction

Back pain is a debilitating health concern, where over 50% of Canadians have been treated by clinicians using spinal manipulation therapy (SMT)<sup>1</sup>. Adverse effects associated with SMT occur at a 23% incidence rate<sup>2</sup> and may be due to deficits in understanding the biomechanics governing SMT. Finite element spine models (FESMs) have improved spine biomechanics knowledge, but current FESMs are computationally slow, patient-specific, and cannot be applied to clinical situations. With recent advances in graphics processing units (GPUs), including a GPU programming interface (CUDA by nVidia), new finite element (FE) implementations significantly increase computation speeds<sup>3</sup>. A projection system is currently under development that allows the clinician to visualize spine response during SMT. This study aims to develop a clinically usable real-time spine simulation that will allow clinicians to visualize biomechanical response during force application.

### Methods

The lumbar spine solid model was developed using SolidWorks 2013, with initial dimensions approximated from literature<sup>4</sup>. Initial FE analysis of SMT forces was completed using ANSYS Workbench 13.0. A custom FE program was developed based on a previous GPU implementation<sup>3</sup>. The solid model was integrated into the custom FE program. The FE mesh included tetrahedral elements for the intervertebral disc, rigid bodies for the vertebrae, beam elements for the pedicles, and bar elements for the ligaments. Fixed boundary conditions were applied at the L1 and L5 vertebral bodies. Linear material properties were acquired from studies in literature<sup>5</sup>.

### Results

A fully parameterized lumbar spine solid model was developed using elliptical bodies to define the vertebral structures. FE

analysis exhibited realistic results with low strain response (maximum of 0.0078 mm/mm) to SMT forces (Fig. 1). The GPU implementation of the resulting FESM demonstrated greatly increased computation speed (less than 5 seconds using the nVidia Quadro 3000M), which was close to real-time.

### Conclusions

A fully parametric and scalable FESM was developed and implemented in GPU architecture. While the computation speed is close to real-time, speed is limited mostly by computational capabilities of the GPU. Real-time analysis may be achieved on an improved GPU (nVidia TITAN BLACK). Nonetheless, this study demonstrates that the current model will be useful for helping clinicians improve their understanding of spine biomechanics and prevent adverse effects during SMT.

### References

1. E.R.Group, *Chiropractic*(2005)
2. Baker, G., *CMAJ* (2004)
3. Mafi, R., *Int. J. Numer. Meth. Biomed. Engng* (2014)
4. Panjabi, M., *Spine* (1992)
5. Shirazi-Adl, A., *Trans. ASME* (1994)

### Figure

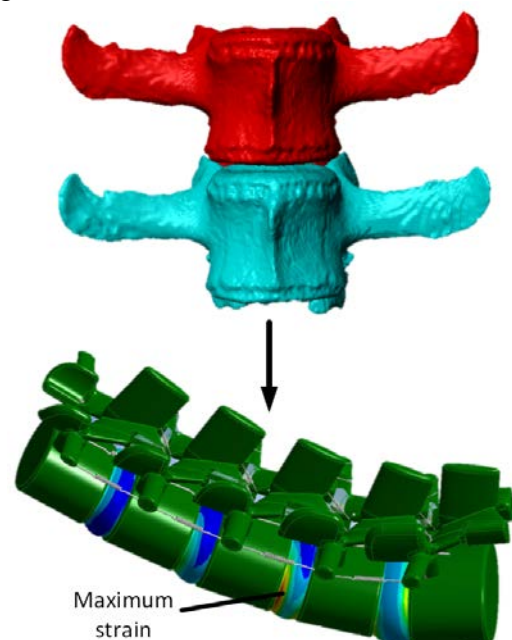


Fig. 1: Solid model development and FE analysis

## Comparison of Two Optical Imaging Systems to Reduce Radiation in Adolescents with Scoliosis

Sarah Sanni<sup>1</sup>, Alexandra Melia<sup>2</sup>, Jessica Küpper<sup>1</sup>, Gulshan Sharma<sup>1</sup>, Janet Ronsky<sup>1</sup>

<sup>1</sup>Mechanical and Manufacturing Engineering, University of Calgary; <sup>2</sup>Biomedical Engineering, University of Calgary

### Introduction

Adolescent Idiopathic Scoliosis (AIS) is a three-dimensional (3D) deformity of the spine characterized by abnormal lateral curvature and vertebral rotation affecting 2-3% of adolescents [1]. The current clinical diagnostic and monitoring method consists of full torso X-rays where the Cobb angle, a measure of spinal deviation from the vertical, is used to determine the magnitude of the deformity. Two major limitations are associated with this approach. First, the routine exposure to radiation has been linked to an increased risk of cancer in scoliotic patients [2]. Second, the Cobb angle is inadequate to fully define the deformity because it is a two-dimensional measure. A holistic approach to define the deformity and reduce radiation exposure is needed.

Changes in spinal curvature alter torsal shape making the use of surface topography (ST) a potential alternative to detect and monitor AIS progression in 3D [3] as well as reduce periodic radiation exposure. The majority of recent attempts to validate ST for clinical implementation have used commercial fringe topographic (FT) methods, which are expensive and take prolonged captures. A novel low-cost photogrammetric system that takes instantaneous captures has been developed to remove errors resulting from movement during a capture and increase torso reconstruction accuracy [4]. The effect of the improved accuracy on the ST measures in the new system is not yet understood. The aim of this study was to compare FT and photogrammetric data, thereby providing

### Methods

Models of four AIS (1M, 3F) and four normal (1M, 3F) subjects between the ages of 9-16 were reconstructed via FT (InSpeck Inc, Montreal; now owned by Creafom, Lévis) and photogrammetric methods in order to compare ST measures in three

regions, i.e. upper (T7), middle (T12) and lower (L4). Captures from the two systems were taken consecutively while subjects were in a positioning frame to reduce movement artifacts between systems. MeshLab was used to generate meshes from the photogrammetric point clouds. A custom scoliosis code [5] calculated ST measures from meshes between T1 and S1. Anatomical landmarks determined each individual's fixed reference frame.

### Results

A repeated measures multivariate analysis of variability compared 11 distinct ST indices calculated from torsal cross-sections [6]. There were two subject groups, normal and scoliosis; two optical methods, FT and photogrammetry; and three analyzed levels, T7, T12 and L4. Statistically significant (SS) differences were found in ST measures between methods ( $p < 0.001$ ) and spinal levels ( $p = 0.032$ ). Further tests revealed SS difference in both the normal ( $p = 0.006$ ) and scoliosis ( $p = 0.002$ ) groups ST measures from the two methods.

### Conclusions

The photogrammetry method produced different ST measures from the FT method. Further method comparison includes distorting photogrammetry data until it matches FT data. Increasing sample size will provide SS information on interaction effects and the effects of improved accuracy and repeatability of the novel system vs. InSpeck (accuracy: 0.3 mm vs. 1.29 $\pm$ 0.45mm; repeatability: 0.19mm vs. 1.4mm; [4, 6]) on ST measures.

### References

1. Weinstein S. Spine (Phila Pa 1976). 24:2592-2600,1999.
2. Levy A, et al. Spine. 21:1540-1547,1996.
3. Komeili A, et al. Spine J. 14:973-83, 2014.
4. Detchev I, et al. Geomatica. 65:175-187, 2011.
5. Sharma G, et al. COA [Poster], 2012.
6. Dubetz T, [MSc Thesis]. 2012.

## Visualization of Collagen Crimp in Annulus Fibrosus using Ultra-High Field 9.4T MRI

Scott Moorman, BSc, Jeff F. Dunn, PhD, John Matyas, PhD, Neil A. Duncan, PhD  
McCaig Institute for Bone and Joint Health, University of Calgary, Alberta, Canada

### Introduction

The annulus fibrosus (AF) surrounds and encloses the gel-like contents of the center nucleus pulposus by its highly organized concentric layers (15-25 lamellae). The outer layers are primarily made up of type I collagen fiber bundles oriented at  $\sim 30\text{-}35^\circ$  referenced to the spinal axis [1]. Morphologically, collagen has been visualized by polarized light microscopy to form a 'zigzag' pattern, known as 'crimp' with a periodicity of  $\sim 50\text{-}200\mu\text{m}$  [2]. Detecting collagen 'crimp' allows for the ability to further investigate the biomechanical properties of a connective tissue. Ultra high-field ( $>7.0\text{T}$ ) magnetic resonance imaging (MRI) is a non-invasive imaging technique with a significantly higher spatial resolution than current clinical devices. The purpose of this study was to characterize the microarchitecture in the AF.

### Methods

Bovine tails were collected from the butcher within 24 hours after slaughter. Transverse incisions were made along the endplates above and below the disc. Circumferential samples were placed in 4% paraformaldehyde and fixed for 24hrs. They were then placed on a small custom platform and loaded into a 20mm RF surface cryocoil. All specimens ( $n=3$ ) were imaged with a 9.4-T magnet. A Bruker FLASH gradient-echo sequence was used to obtain high-resolution images: TE/TR: 6.5/250ms, Pulse Angle =  $30^\circ$ , NT = 3, FOV = 1.92x1.92cm, matrix = 512x512, slice thickness = 0.25mm giving a  $37.5 \times 37.5 \times 250 \mu\text{m}^3$  voxel. The periodicity of crimp was measured using line scans (5 pixel width) parallel to the 'banding pattern' on matching slices and measuring the trough-to-trough change in signal intensity over the length of that area (5 averages within that area). Following MRI, sagittal and coronal sections ( $20\mu\text{m}$ ) were illuminated with circularly polarized light. Similarly, line scans (5 pixel width and 5 averages) were measured within the matching area.

### Results

With this novel imaging sequence and RF surface cryocoil, we have demonstrated the ability to detect a periodic banding pattern along coronal, axial, and sagittal views (Figure 1). More specifically along the coronal slice, the patterns were organized in bundles that run at  $\sim 30\text{-}36^\circ$  to the spinal axis. Sequentially through each 0.25mm MR slice, the banding patterns move in and out of each slice and flipped orientation from layer to layer. The mean periodicity ( $\pm$ SD) of the banding pattern from the coronal view was calculated to be  $103.0 \pm 0.2\mu\text{m}$ , while the sagittal view was  $104.0 \pm 5.9\mu\text{m}$ .

### Conclusions

This is the first study using a novel RF surface cryocoil and ultra high-field MRI to characterize the micro-architecture of AF tissue. We have obtained high-resolution images illustrating banding patterns that match the 'zigzag' pattern of collagen 'crimp'. Furthermore, the calculated mean periodicity of the patterns from signal intensity has been determined to fall within the range (50-200 $\mu\text{m}$ ) of collagen 'crimp' described in the literature [2,3].

### References

- [1] Marchand, F., and Ahmed, A. *Spine* 1990.
- [2] Gathercole, L., and Keller, A. *Matrix* 1991.
- [3] Mountain, K., *et al. Mag. Reson. in Med.* 2011.

### Figures

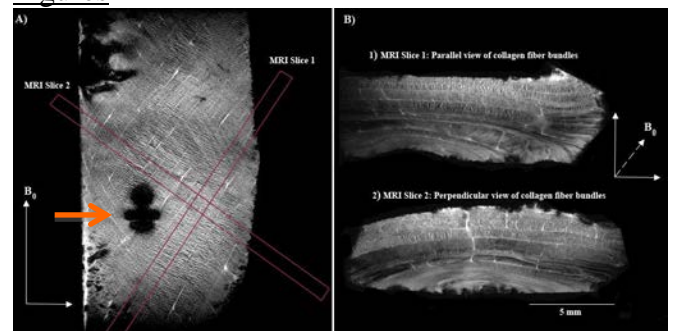


**Figure 1:** (A) Coronal slice of circumferential outer annulus fibrosus. (B) Axial and sagittal slices of circumferential outer annulus fibrosus. Note – the orange arrow represents an artifact. FLASH gradient-echo sequence: TE/TR: 6.5/250ms, Pulse Angle =  $30^\circ$ , NT = 3, FOV = 1.92 x 1.92cm, matrix = 512 x 512, slice thickness = 0.25mm, and voxel =  $37.5 \times 37.5 \times 250\mu\text{m}^3$ .

## Preliminary study of the Mechanical Properties of Hydrogel Substrates on Cell Viability

Liqun Ning<sup>1</sup>, Yitong Xu<sup>2</sup>, Daniel Chen<sup>1,3</sup>, David Schreyer<sup>2,3</sup>

1: Department of Mechanical Engineering, College of Engineering, University of Saskatchewan; 2: Department of Anatomy and Cell Biology, College of Medicine, University of Saskatchewan; 3: Division of Biomedical Engineering, College of Engineering, University of Saskatchewan

### Introduction

Schwann cells play an essential role for neuron regrowth in the peripheral nerve repair process [1]. Cell adhesion is a factor that directly affects cell behaviors such as survival, proliferation and migration. Cells interact with their surrounding not only biochemically but also physically [2]. We first mixed proteins and peptides into an alginate hydrogel to promote attachment of cells. By comparing the morphology of Schwann cells, determined the appropriate protein or peptide was determined. We then studied the effect of changing the mechanical property of the hydrogel by varying the alginate concentration.

### Methods

Poly-L-lysine (PLL), fibronectin and RGD peptide were selected for promoting cell attachment. Each of these three materials was mixed with 1.5% alginate solution crosslinked with calcium-ions. A cell line derived from Schwann cells (RSC96) was seeded onto the surface of the gel and cultured for 48 hours, then cell morphology was examined microscopically. Once the appropriate protein or peptide was chosen, different concentrations of alginate solution including the chosen material were crosslinked. 3-(4,5-dimethylthiazol-2-yl)-2,5-diphenyltetrazolium bromide (MTT) assay was performed to assess cell viability. Cylinder hydrogel samples of different alginate concentrations were prepared and then tested to calculate the Young's modulus.

### Results

Figure 1 shows the morphology of cells seeded onto the surface of alginate substrates with different additives. Cells on plain alginate were round and clumped. Cells on substrates including PLL or fibronectin were less clumped, but remained round. Inclusion of RGD peptide was associated with a flattened, polygonal morphology of Schwann cells, and they began to extend processes, suggesting that

this condition is the best choice for cell proliferation compared with others. The mechanical property of alginate hydrogel (Young's modulus) expected to vary when changing alginate concentration between 1.0% and 2.5%. Figure 2 shows the results of the compression test and MTT assay and illustrates that cells viability can be influenced by the mechanical property. A Young's modulus of 4.6 KPa appears to be optimal. Comparison of negative control group suggests that cell viability may be as least as sensitive to mechanical property of their environment as they are to the presence of adhesion-promoting peptides.

### Conclusions and Discussion

Our results show that alginate hydrogel mixed with RGD peptide can promote cell adhesion and viability. They also demonstrate that the mechanical property of an alginate substrate can influence cell viability directly. Further experiments will be conducted for 3D cultures encapsulating Schwann cells. This test will determine the relation between encapsulated cell viability and hydrogel mechanical property.

### References

- [1] Mirsky, et al. *Journal of Physiology-Paris*, 2002  
[2] Gu Y, et al. *Biomaterials*, 2012

### Figures

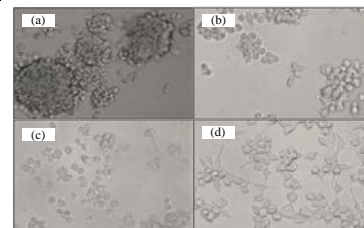


Fig. 1 Cell morphology on 1.5% alginate gel with (a) no additive; (b) PLL; (c) fibronectin or (d) RGD peptide

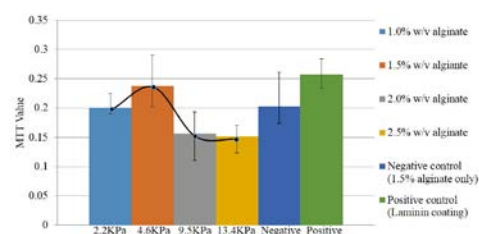


Fig. 2 Relation between Schwann cell viability (MTT value) and Young's modulus of alginate substrate

## Electrical stimulation of a rat sciatic nerve using an addressable-electrode nerve conduit

M. Purdy<sup>1</sup>, Y. Shapira<sup>2,3</sup>, R. Midha<sup>2,3</sup>, D. W. Zochodne<sup>3</sup>, C. Dalton<sup>4</sup>

<sup>1</sup>Biomedical Engineering Program, <sup>2</sup>Department of Clinical Neurosciences, <sup>3</sup>Hotchkiss Brain Institute, <sup>4</sup>Department of Electrical and Computer Engineering - University of Calgary, Calgary, Alberta, Canada

### Introduction

Peripheral nerve injury afflicts 2.4% of the world's population, with many causes including disease and physical trauma<sup>1</sup>. Fortunately, brief electrical stimulation (ES) has been shown to both accelerate and direct growth of axons<sup>2,3</sup>. Guided growth of axons could reduce misalignment and improve regenerative outcomes of the otherwise slow process. Current *in vivo* techniques utilize long distance electric fields through hook electrodes or conductive nerve scaffolds<sup>4</sup>. In this project, a nerve conduit has been fabricated that will apply multiple, progressive ES to leading growth cones of regenerating nerves. The purpose of this study is to evaluate such a nerve conduit in its ability to apply ES to a nerve without causing debilitating discomfort or adverse effects within an animal.

### Methods

Two implantable nerve conduits were designed to deliver voltages between nerve stumps after transection injury. One device consisted of 10 0.75 mm-wide copper electrodes spaced 0.25 mm from one another, printed on a flexible laminate. The other device had 7 electrodes. 8 mm of the 25 mm-long electrodes were coated with a biocompatible gold layer, and the rest were coated with an insulating polyimide.

The implant was rolled into a hook shape and secured around the right sciatic nerve of a male Lewis rat, acting as a guiding scaffold without preventing vascularization of the regenerating nerve (Fig.1). The nerve was either transected leaving a 5 mm gap (n=1) or left intact (n=2), and then sutured to the nerve. Connecting wires were tunneled from the leg to the base of the neck subcutaneously, where they were joined to a zero-insertion force connector. Stimulation was applied with a Grass stimulator immediately after implantation and consisted of a brief 20 Hz train of 0.1 msec-duration electrical pulses at supramaximal

voltage (3V). This ES paradigm is a standard procedure in nerve regeneration experiments<sup>4</sup>. Implants were then left within the animal for one week before removal and assessment of discomfort and locomotion.

### Results

The nerve conduits were successfully implanted and secured to the intact and transected sciatic nerves. Intact nerve models were successfully stimulated using each of the designs, and multiple electrodes were tested. It was noted however that the devices were too large to remain within the animals for an extended period of time. After one week, animals were more reluctant to use their injured leg than the transection accounted for. Although the devices remained in place, inflammatory response and fibrosis were suggesting that the device was not entirely compatible within the body.

### Conclusions

Preliminary studies have shown successful implantation of the nerve conduit, but a smaller device will be necessary to prevent complications throughout the experiment. To prevent inflammation, fully biocompatible materials will be used. Such a device has been created and is in testing, consisting of short platinum wires embedded in a polymer, allowing for a less bulky, more flexible, and fully biocompatible device.

### References

1. Hughes + 2002. 2. Al-majed + 2000. 3. Gordon + 2010. 4. Haastert-Talini + 2013. 5. Song + 2004.

### Figures



**Fig.1** A nerve conduit is wrapped around the un-transected nerve and sutured into place.

## EMBRYONIC MYOSIN HEAVY CHAIN EXPRESSION IN SKELETAL MUSCLE AS A MARKER OF RECOVERY AFTER ELECTRICAL STIMULATION DAMAGE

Vivian Arian Wang, Kelly Kaiser, Walter Herzog  
2500 University Drive NW, Calgary, AB, Canada T2N 1N4

### Introduction

Spasticity is a symptom commonly found in neuromuscular disorders. It is characterized by involuntary muscular activation which may lead to increased passive stiffness and hypo-extensibility [1]. To investigate the muscular adaptations of spasticity, serial sarcomere loss in electrically stimulated guinea pig soleus was determined, resulting in an average of 25% serial sarcomere loss in twelve hours [2]. Similar results were found using the same protocol in a New Zealand White Rabbit model [3].

Preliminary results in our lab suggested that 48 hours following a 10-hour continuous stimulation protocol was sufficient for recovering most of the lost serial sarcomeres. The purpose of this study was to investigate how this remarkable sarcomere recovery may be occurring. It has been suggested that after skeletal muscle damage, a re-expression of developmental forms of myosin heavy chain (MHC) occurs [4]. Therefore, the purpose of this study was to test the possibility that re-expression of developmental forms of MHC might be involved in the recovery of lost sarcomeres.

### Methods

Three New Zealand White Rabbits were used. One hind limb acted as the experimental and the contralateral limb as the control. The experimental limb was electrically stimulated (30Hz) through the tibial nerve over a 10-hour period followed by a 48-hour recovery period prior to muscle harvest. Sarcomere loss was determined in chemically isolated fascicles by dividing fascicle length by the average sarcomere length determined using laser diffraction. Re-expression of developmental MHC's was measured using SDS-PAGE and Western Blot techniques with the use of embryonic and neonatal MHC specific antibodies.

### Results

Serial sarcomere loss following 48 hours of recovery was  $0.8 \pm 1.7\%$ ,  $1.7 \pm 0.9\%$ , and  $7.9 \pm 9.6\%$  for medial gastrocnemius (MG), plantaris and soleus, respectively.

Western blot analysis showed strong signals of developmental MHC in the positive control, and mild signals in all samples for the neonatal MHC antibody.

### Conclusions

The 25% sarcomere loss associated with 10 hours of muscle stimulation was almost fully recovered following a 48 hour recovery period. There was little developmental MHC expression in the experimental tissues. The low strength of positive signals may indicate a minor crossover from the adult forms of MHC, and therefore was disregarded.

We conclude from these results that serial sarcomere recovery in this model does not occur through the re-expression of developmental forms of MHC. Future studies may focus on the disassembly and reassembly of sarcomeres in series, rather than the production of new sarcomeres. These findings may be beneficial in furthering our understanding of serial sarcomere regulation in healthy muscles and might help develop treatment strategies for structural muscle diseases resulting in serial sarcomere loss, such as spasticity.

### References

1. Friden J. & Lieber R.L. *Muscle Nerve*. **27**(2):157-164, 2003.
2. Tabary J. *et al. Muscle Nerve*. **4**:198-203, 1981
3. Yamamoto M., Leonard T. & Herzog W. *JURA*. **2**(1), 2012.
4. Yoshimura K. & Harii K. *J SURG RES*. **81**:139-146, 1999.

## Integrin $\alpha 1\beta 1$ Increases Signs of Post-traumatic Osteoarthritis in a Tissue Specific Manner

<sup>1</sup>Shin, S Y, <sup>2</sup>Milo, L, <sup>3</sup>Floreani, E, <sup>4</sup>Pozzi, A and <sup>1</sup>Clark, A L

Faculties of <sup>1</sup>Kinesiology, <sup>2</sup>Medicine, and <sup>3</sup>Engineering, University of Calgary, Calgary AB;

<sup>4</sup>Division of Nephrology and Hypertension, Vanderbilt University, Nashville, TN

### Introduction

Post-traumatic osteoarthritis (PTOA) develops in 40% of people following a significant knee injury [1]. The collagen receptor integrin  $\alpha 1\beta 1$  negatively regulates epidermal growth factor receptor (EGFR) signaling [2] and its expression is increased in cartilage with spontaneous OA [3,4]. Interestingly, integrin  $\alpha 1$ -null (KO) mice develop spontaneous OA 2 months earlier than wild-type (WT) controls [3,5]. Furthermore, mice deficient in Mig-6 show increased EGFR signaling and accelerated spontaneous OA [6]. Erlotinib, an EGFR inhibitor, has been used to effectively treat rheumatoid arthritis in mice [7]. The role of integrin  $\alpha 1\beta 1$  in PTOA and the mechanism(s) by which integrin  $\alpha 1\beta 1$  exerts its influence upon OA are unknown. It is hypothesized that integrin  $\alpha 1\beta 1$  protects against PTOA by a mechanism that involves dampening of EGFR signaling.

### Methods

Surgery to destabilize the medial meniscus (DMM) or sham control surgery was performed on the left leg of 50 skeletally mature male KO and WT mice. Mice were sacrificed at 2, 4, 8 or 12 weeks post-surgery. Half of the 12 week mice were given erlotinib (50mg/kg/day) by oral gavage. After sacrifice, hind-limbs were isolated, skinned and fixed prior to microCT scanning. Bone mineral density and volume were calculated for the calcified portions of the menisci, trabecular, and subchondral bone. Data was analyzed with ANOVA and Fisher LSD post hoc ( $p < 0.05$ )

### Results

There was no significant difference in mass between WT and KO mice (WT =  $31.7 \pm 0.4$ g, KO =  $31.1 \pm 0.3$ g). Anterior medial meniscus volume increased from 2 to 12 weeks in the DMM surgery leg of both WT and KO mice, and it was larger in mice treated with erlotinib compared to control,

with this effect being greater in WT compared to KO mice (Fig 1). In addition, subchondral bone volume in the DMM surgery leg increased significantly from 8 to 12 weeks post-surgery in WT but not in KO mice independently of erlotinib (Not shown). Genotype, time post-surgery and erlotinib had no effect on bony signs of PTOA in sham and contralateral legs (Not shown).

### Conclusions

Integrin  $\alpha 1\beta 1$  increases signs of PTOA in a tissue specific manner affecting subchondral bone but not meniscus. On the other hand, EGFR signaling decreases signs of PTOA in the meniscus but not subchondral bone. Contrary to our hypothesis, integrin  $\alpha 1\beta 1$  plays contrasting roles in two models of OA: increasing signs of PTOA but decreasing signs of spontaneous OA, and this may be due to the disease occurring over a shorter time frame and involving sudden mechanical and inflammatory changes in PTOA.

### References

[1] Anderson+ J Orthop Res, 29: 802-809, 2011, [2] Chen+ J Clin Invest, 124: 3295-3310, 2014 [3] Zemmyo+ Arthritis Rheum, 48: 2873-2880, 2003, [4] Loeser+ Exp Cell Res, 217: 248-257, 1995 [5] Shin+ 58th Annu Meet Orthop Res Soc 2012, [6] Zhang+ P Natl Acad Sci USA, 111: 2590-2595, 2014. [7] Swanson+ J Immunol, 188: 3513-3521, 2012.

### Figures

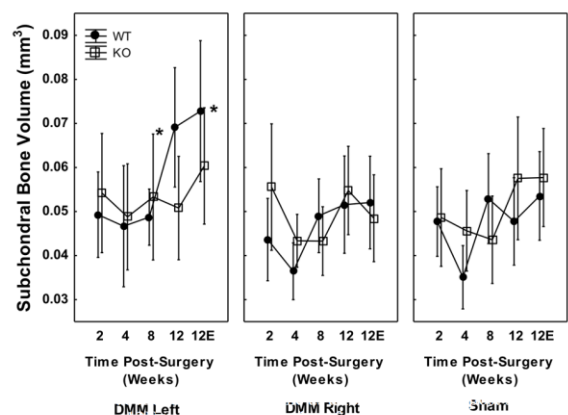


**Figure 1:** Subchondral bone volume as a function of time post surgery and genotype. 12E was given 50 mg/kg of erlotinib daily until sacrifice. Bars represent a 95% confidence interval. Significantly ( $p < 0.05$ ) different from \* = KO equivalent.

## Chondrogenic differentiation of synovial progenitors isolated from patients with hip pathologies

Asmaa Affan  
aaffan@ucalgary.ca

### Introduction

Osteoarthritis (OA) is a chronic degenerative joint disease that is characterized by the loss of articular cartilage, inflammation, and pain<sup>1</sup>. Within the hip joint, arthroplasty (joint replacement) remains one of the only interventions available<sup>1</sup>. Interestingly, there is a resident synovial mesenchymal progenitor cell (sMPC) population within the synovial membrane and the synovial fluid of the joint<sup>2</sup>. These cells have the ability to differentiate into bone, fat and cartilage<sup>2</sup>.

The objectives of this study were to quantify, characterize, and compare the chondrogenic differentiation potential of sMPCs derived from multiple patients.

### Methods

The synovial membrane tissue and synovial fluid obtained from hip samples of OA patients undergoing arthroplasty underwent flow cytometry analysis as well as qRT-PCR to characterize endogenous cell populations. In brief, the synovial membrane and synovial fluid were vigorously digested in 1 mg/mL of collagenase for 2 hours. The samples were then filtered and washed in PBS, and then fixed in paraformaldehyde. They were subsequently stained with CD90, which is an sMPC marker, as well as CD68 and CD14, which are macrophage markers<sup>3</sup>. For pRT-PCR, the synovium biopsy samples were seeded, and the cells were cultured and purified with the CD90 marker using magnetic purification. The cells were expanded, and then underwent a 21-day chondrogenic differentiation process, both in pellet form and monolayer form (50K cells/well). The differentiation media contained TGFβ, BMP-2, and ascorbic acid. Following chondrogenesis, mRNA was then extracted, cDNA was made, and subsequently a PCR was run in triplicate.

### Results

Flow cytometry data collected from Patient #44 OA hip synovial membrane and synovial fluid shows that there was positive staining for both macrophages as well as synovial MPCs. For the qPCR data, the samples from osteoarthritic patients #32 and #34 were normalized to the monolayer chondrogenic data to assess the fold differences in gene expression of Aggrecan (Acan), Collagen IIa (Col2a), and Sox 9 in pellet versus monolayer form. The data obtained for both patients shows that the sMPCs undergoing pellet-cultured chondrogenesis had lower expression levels of Acan, Col2a, and Sox9 compared to monolayer chondrogenesis.

### Conclusions

In the study, it was seen that mesenchymal progenitor cells are found to be present in OA hip synovial membrane as well as synovial fluid.

These sMPCs had higher expression of Acan, Col2a, and Sox9 following monolayer chondrogenesis compared to pellet chondrogenesis.

Future work will assess if distinct synovial mesenchymal progenitor cells and/or phenotypes are present, and this will be done through single cell sorting using FACS technology.

### References

- <sup>1</sup> Harris Q, *et al.* (2013) Monocyte chemotactic protein-1 inhibits chondrogenesis of synovial mesenchymal progenitor cells: An in vitro study. *Stem Cells* 31(10): 2253-65
- <sup>2</sup> De Bari C, *et al.* (2001) Multipotent mesenchymal stem cells from adult human synovial membrane. *Arthritis Rheum* 44(8): 1928-42
- <sup>3</sup> Kunisch E, *et al.* (2004) Macrophage specificity of three anti-CD68 monoclonal antibodies (KP1, EBM11, and PGM1) widely used for immunohistochemistry and flow cytometry. *Ann Rheum Dis* 63: 774-784

## Investigation of Factors that Impact Compressed sensing Reconstruction Resolution

Paniz Adibpour<sup>1</sup>, Michael Smith<sup>1,2</sup>

<sup>1</sup> Electrical and Computer Engineering, <sup>2</sup> Radiology, University of Calgary, Calgary, Alberta, Canada

**Introduction:** Magnetic resonance imaging (MRI) is a frequently used medical imaging modality for studies of stroke or neurological diseases. Reconstructing MRI data sets involving time series introduces conflicts between high spatial and high temporal resolution. Compressive sensing (CS) has revolutionized MRI data acquisition by exploiting sparseness properties to recover randomly under-sampled k-space data using an appropriate nonlinear recovery scheme [1]. Two important factors affect the resolution accuracy of CS reconstructed data set:

1) DFT imposed k-space continuity property constraints must be taken into account since CS repeatedly uses DFT to move data between k-space and image domains [2]. This directly impacts the effective texture resolution by introducing a position dependent resolution property. Smith et al. [2] suggested a high resolution k-space extrapolation enabled (*Hi-KEE*) extension to eliminate this issue.

2) Based on the main image features, choose the most appropriate transform that will best sparsely represent image data set. With brain images texture-rich and involving contour shaped components, the better direction selectivity of Contourlet transform [3] has been shown to provide a sparser representation with higher redundancy [4] outperforming the common wavelet sparse transform [5].

In this manuscript we propose the combination of the *Hi-KEE* approach with Contourlet CS reconstruction. We quantitatively evaluate experimental results of *Hi-KEE* implementation on brain phantom data set and compare *Hi-KEE* and CS methods based on wavelet and Contourlet transform.

**Methods:** The software settings for *CS\_MRI\_Contourlet* package ([quxiaobo.8866.org/project/CS\\_MRI\\_Contourlet/CS\\_MRI\\_Contourlet.zip](http://quxiaobo.8866.org/project/CS_MRI_Contourlet/CS_MRI_Contourlet.zip)) were left unchanged. A random variable density sampling pattern with 33% sampling rate (fully sampled centre core of size 0.1) was applied to a 128 x 128 data set truncated from a 512 x 512 data set (Fig. A). Two objective criteria were used to evaluate the correlation between CS and IDFT reconstructed data set. Mutual information (MI) [6] computes how much information is transferred from fully sampled k-space to CS-based reconstructed image while transferred edge information

(TEI) [7] measures the amount of edge information CS reconstructs. The same brain data set truncated to 128x128 has been used.

**Results:** The experimental results of performing CS method based on Contourlet (Fig. C) shows better recovery of contours and high resolution features in comparison to CS based on wavelet (Fig. B). *Hi-KEE* combined with Contourlet outperforms the two aforementioned methods by restoring the artifacts still visually recognizable (Fig. D). A comparison of CS methods using TEI (Fig. E) and MI (Fig. F) evaluation quantitatively proves the superiority of Contourlet based *Hi-KEE*.

**Conclusion:** Investigating DFT imposed properties on CS method on one hand and understanding the important features of the image on the other hand can lead to a more reliable reconstruction algorithm. An I3T scholarship will fund a future investigation of the open problem of making the proposed method adaptive, i.e. automatically applicable for different image characteristics.

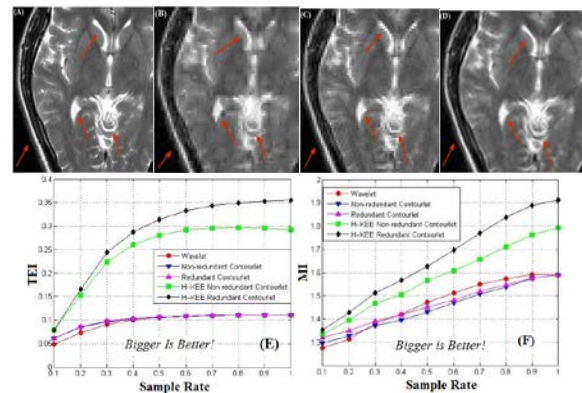


**Figure:** (A) The original 512x512 brain data set. (B) 128x128 CS reconstructed based on wavelet, pixel duplicated to 512x512 has lower high resolution accuracy as does (C) CS reconstructed based on non-redundant Contourlet, pixel duplicated to 512x512. (D) *Hi-KEE* based on non-redundant Contourlet better recovered all contour and high resolution individual components of the image. (E) TEI and (F) MI evaluation criteria quantitatively shows the superiority of the *Hi-KEE* redundant Contourlet combination.

**References:** [1] Lustig et al., *MRM*, 58(6), 1182-95, 2007; [2] Smith et al., *ISSC*, 2013. [3] Do et al., *IEEE TIP*, 14(12), 2091-2106, 2005; [4] Coifman et al., *Wavelets and Statistics*, 125-50, 1995; [5] Qu et al., *IPSE*, 18(6), 737-58, 2010; [6] Qu et al., *Electron. Lett.*, 38, 313-15, 2002; [7] Xydeas et al., *Electronics Letters*, 36(4), 308-9, 2000.

## An idealized branching airway geometry that mimics average aerosol deposition in pediatric central conducting airways

Azadeh A. T. Borojeni, Michelle L. Noga, Andrew R. Martin, Warren H. Finlay

Department of Mechanical Engineering, University of Alberta, Edmonton, Alberta, Canada, T6G 2G8

### Introduction

To date, idealized conducting airway geometries for children are not widely available, largely due to limited aerosol deposition data in children's airways upon which to develop and validate such a geometry. In our recent study, aerosol particle deposition was measured in physical replicas of central conducting airway geometries obtained from segmented computed tomography (CT) scans of school-aged children<sup>1</sup>. Considerable variation in deposition was observed, due to intersubject variability in airway geometry. However, for development of inhaled pharmaceutical products, an idealized geometry that mimics average deposition in the pediatric population is highly desirable.

### Methods

#### Idealized Model Development

Recently, good agreement between aerosol deposition measured in physical replicas of pediatric central conducting airways and analytical predictions made using the Chan and Lippmann<sup>2</sup> correlation was reported<sup>1</sup>. The ability of this correlation to predict deposition in pediatric airways suggests that the main geometrical features affecting deposition in child and adult central conducting airways are similar. Consistent with this suggestion, in the present work, an idealized adult geometry previously described by Zhang et al.<sup>3</sup> was uniformly scaled down to yield an idealized child geometry. In order to determine an appropriate scale factor, least-squares fitting was done to compare predicted deposition in scaled, idealized geometries to the average deposition measured in the 10 realistic pediatric airways.

#### Particle Deposition Measurements

The total deposition for each particle size in the idealized hollow replica is defined as:

$$\eta_{\text{Total}} = \frac{M_m}{(M_m + M_f)} \times 100$$

where  $M_m$  is the mass of particles deposited in the idealized airway cast and  $M_f$  is the mass deposition on the filters.

### Results

#### Idealized Model Development

A range of geometric scale factors was assessed analytically to predict total deposition in scaled airway replicas. These predictions were compared to the average deposition measured in 10 realistic central conducting airway replicas of children aged 4-8 years old<sup>1</sup>. A best-fit scale factor of 0.56 was selected based on least-squares fitting to the average data from the realistic replicas.

#### Particle Deposition Measurements

Using the optimal scale factor of 0.56 as predicted analytically, an idealized pediatric central conducting airway geometry was built and tested in vitro. The idealized data was found to lie well within the range of the experimental data, and correspond closely with the average deposition data in the 10 realistic replicas.

### Conclusions

Experiments confirmed that aerosol deposition in the idealized geometry was consistent with the average deposition measured in 10 realistic replicas for children 4-8 years old. In contrast, airway resistance in the idealized geometry fell near the lower limit of resistances measured in the realistic replicas, and aerosol deposition was only weakly correlated with pressure drop across the airways. The present idealized geometry represents a tool that may be useful in the research and development of pharmaceutical aerosol delivery to school-aged children.

### References

- <sup>1</sup>Borojeni, A. A., M. L. Noga, R. Vehring and W. H. Finlay. Measurements of total aerosol deposition in intrathoracic conducting airway replicas of children. *Journal of Aerosol Science*. 73 :39-47, 2014.
- <sup>2</sup>Chan, T. L. and M. Lippmann. Experimental measurements and empirical modeling of the regional deposition of inhaled particles in human. *American Industrial Hygiene Association Journal*. 41 :399-459, 1980.
- <sup>3</sup>Zhang, Y. and W. H. Finlay. Experimental measurements of particle deposition in three proximal lung bifurcation models with an idealized mouth-throat. *Journal of Aerosol Medicine*. 18:460-473, 2005.

# Measurements of Anisotropy Ratio and Fiber Orientation in Cardiac Tissue Propagation

Amin Ghazanfari, Anders Nygren  
University of Calgary

## Introduction

Cardiac propagation characteristics such as anisotropy ratio and conduction velocities are often determined experimentally from epicardial measurements. We showed previously that these measurements have inaccuracies due to intramural fiber rotation and transmural electrotonic interactions. We also showed that optical mapping (OM) recordings compound the error, due to contributions from deeper layers. Three different methods introduced to measure anisotropy ratio (AR) and fiber orientation. Also effects of an uncoupler on these measurements are simulated.

## Methods

A mathematical model of rat ventricular myocytes was used as the base single cell model. Tissue slabs were created with different thicknesses (1mm, 2mm, 4mm, and 1cm). The myocardial tissue included fiber orientation that varied continuously and linearly 120 degrees from epicardium to endocardium.

Activation time was defined for each point as the moment when membrane potential crossed zero in the action potential upstroke. Isochrones were defined as contour plots of the activation time which represent the points that have the same activation time. Since the action potential propagates faster in the fiber direction, isochrones were expected to have an elliptic shape. A least square error algorithm was implemented to fit ellipses to each isochrone.

Conduction velocity vectors for each point were calculated using the gradient of activation maps. We introduced three different methods to measure anisotropy ratio. 1) The ratio of major to minor axis of the best-fit ellipse, 2) The ratio of maximum conduction velocity to minimum conduction velocity ( $\theta_{max}/\theta_{min}$ ), 3) The ratio of longitudinal to transverse conduction velocity observed at the apices of the best-fit ellipse.

The angle of wave propagation was considered to be the angle of the major axis of the ellipse relative to the epicardial fiber orientation. This angle could be one possible estimate of the fiber orientation. We also introduced an alternative measure in which the fiber direction was considered to be the direction of maximum conduction velocity along the relative isochrone.

## Results

Previous results showed that even when the measurements are ideal and there is no OM effect, there are still inaccuracies in the measurements and these errors increase as the tissue gets thinner. It also showed that OM increases the error in measurements.

Simulation results are summarized in Table 1. Results showed for noise free simulated data,  $\theta_{max}/\theta_{min}$  method is more accurate to measure the AR and the angle of propagation but when this method applied to experimental data the measurements based on the fitted ellipse was more accurate (Fig.1a).

Our results also showed using a gap junction uncoupler is not likely to improve estimates AR,  $\theta_l$  and  $\theta_t$  since it affects the conductivity in the same way in all direction (Fig.1b).

## Conclusions

This paper showed that fiber rotation causes error in conventional measurement methods used to estimate fiber orientation and anisotropy ratio. These errors are affected by the tissue thickness and intramural conductivity and are increased by optical effects during optical mapping recordings. Despite significant errors in thin tissue preparations, the most appropriate method (at least of the ones considered here) for estimating fiber orientation and AR experimentally appears to be least-squares fitting of an ellipse to an activation time isochrone.

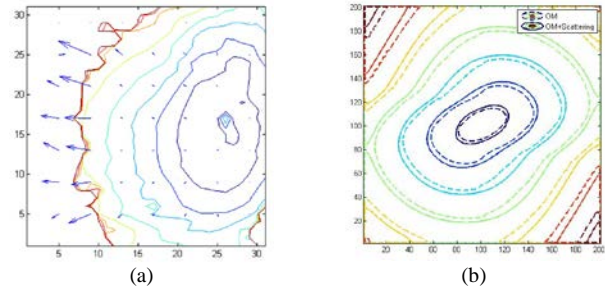


Fig. 1. (a) Direction of  $\theta_{max}$  for experimental data. (b) Simulation results of using an uncoupler (50% reduction in conductivities)

TABLE I  
MEASURED EPICARDIAL FIBER DIRECTION AND ANISOTROPY RATIO

		Thickness			
		1mm	2mm	4mm	1cm
AR	Ellipse	1.7	2.2	2.7	2.9
	$\theta_l/\theta_t$	1	1.8	2.4	2.9
	$\theta_{max}/\theta_{min}$	2.1	2.4	2.7	2.9
$\varphi$ (degrees)	Ellipse	24	16	7	2
	$\theta_{max}$	10	8	4	2

Measured epicardial fiber direction and anisotropy ratio for different methods: direction of 1) fitted ellipse (Ellipse) and 2) maximum conduction velocity ( $\theta_{max}$ ). AR is calculated based on: the ratio of 1) major and minor axis of fitted ellipse (Ellipse), 2) longitudinal to transverse conduction velocities of fitted ellipse ( $\theta_l/\theta_t$ ), and 3) maximum to minimum conduction velocity ( $\theta_{max}/\theta_{min}$ ).

## Using multimodal near-infrared spectroscopy and magnetic resonance imaging to measure in-vivo oxidative metabolism in mice

Thomas W. Johnson, Jeff F. Dunn  
Univeristy of Calgary, Faculty of Medicine, Calgary, Alberta

### Introduction

The brain has an absolute requirement for oxygen. Disruption of oxygen metabolism occurs with many disorders including stroke, multiple sclerosis, dementia, and brain injury. Multimodal near-infrared/MR imaging has the potential to be used to measure global oxidative metabolism in brain tissue. Here we demonstrate its use in measuring cerebral metabolic rate of oxygen consumption ( $CMRO_2$ ) in mouse models of neurological disease.

### Methods

C57BL/6 mice (n=4) were spontaneously ventilated with 3% isoflurane, 30%  $O_2$ , and 67%  $N_2$ . Breathing, heart rate and temperature were all monitored and kept as constant as possible.  $CMRO_2$  was calculated using the Fick principle, given by  $CMRO_2 = 1.36(\text{ml} \cdot \text{g}^{-1}) \times CBF \times (S_a - S_v) \times [tHb]$ . Cerebral blood flow ( $CBF$ ) was obtained with ASL-MRI; where  $S_a$  is arterial blood saturation obtained through pulse oximetry;  $S_v$  is venous blood saturation and is calculated from NIRS data; and  $[tHb]$  is total hemoglobin concentration, also obtained with NIRS. Arterial spin labelling data was collected with a 9.4T Bruker animal MRI system using the Bruker Avance II console, an CASL HASTE sequence and a spin-tagging plane through the carotid artery, matrix dimensions of 128 x 128 pixels, FOV=3cm, TE=2.66ms, TR=3000ms. The arithmetic difference between two 'tagged' and two 'control' images were used for the perfusion-weighted images. NIRS data was obtained by transmitting broadband light through fibre optics onto the dorsal skull and collecting via another fiber placed 6mm laterally into a spectrometer, where it was digitized with a CCD camera. Data was processed using an in-house MATLAB software package based on a second-differential spectrum least-squares fitting algorithm<sup>1</sup>, giving  $[Hb]$  and  $[tHb]$ . To determine regions of the brain that were contributing to the NIRS signal,

transport of NIR light in skin, skull and brain tissue was modelled using a finite element mesh derived from an MR image of a mouse in the NIRFAST software package<sup>2</sup> and ROIs were placed in the centre of the light path. The MR image was obtained with a helium-cooled low-noise surface coil using a FLASH sequence at 512x512 pixels, TR=1500ms, TE=6.5ms, FOV=19.2mm x 19.2mm for a resolution of 37.5 x 37.5 x 250  $\mu\text{m}$ .

### Results

The  $CMRO_2$  for the group (n=4) was calculated to be  $2.03 \pm 0.48$  mL  $O_2$ /100g/min (mean $\pm$ S.D.) using data shown in Table 1. These results agree with ?? measured using ? PET? in rats.

### Conclusions

By combining NIRS and ASL-MRI we have shown it is possible to obtain in vivo measurements of  $CMRO_2$  in mice. Due to the high utility of mice as a model organism, this technique will be useful in investigating neurodegenerative disorders and other diseases that might affect brain metabolism.

### References

1. Mather, S. J. & Cooper, C. E. *Phys. Med. Biol.* **39**, 1295 (1999).
2. Dehghani, H. *et al. Commun Numer Methods Eng* **25**, 711–732 (2008).

### Figures

	CBF (mL/g/s)	$S_a$	$S_c$	$CMRO_2$ (mL/100g/min)
<b>M1</b>	0.0408	0.992	0.802	1.73
<b>M2</b>	0.0545	0.992	0.786	2.51
<b>M3</b>	0.0356	0.992	0.817	1.40
<b>M4</b>	0.0469	0.972	0.738	2.46

**Table 1:** Experimentally determined values of cerebral blood flow ( $CBF$ ), arterial saturation ( $S_a$ ), capillary saturation ( $S_c$ ) and calculated  $CMRO_2$  values for each mouse.

## Validating pQCT-based Indices of Distal Radius Bone Strength under Combined Loading

Matthew P. McDonald<sup>1</sup>, James D. Johnston<sup>1</sup>, Cathy M. Arnold<sup>2</sup>, Geoff Johnston<sup>2</sup>, Saija A. Kontulainen<sup>3</sup>

<sup>1</sup>Mechanical Engineering Department, University of Saskatchewan, Saskatoon, SK, Canada

<sup>2</sup>College of Medicine, University of Saskatchewan, Saskatoon, SK, Canada

<sup>3</sup>College of Kinesiology, University of Saskatchewan, Saskatoon, SK, Canada

### Introduction

Distal radius fractures (DRF) are the most common osteoporotic fracture in women and an important predictor of other osteoporotic fractures [1]. A DRF occurs when the external forces applied to bone—usually due to fall—exceed the strength of bone (i.e., failure load). Peripheral quantitative computed tomography (pQCT) provides a potential monitoring tool for estimating DRF failure load via structural strength indices such as area (related to axial loading resistance) or area moment of inertia (related to bending resistance). Research to date has focused primarily on axial-based indices of bone strength, specifically area [2]. However, during a fall, the distal radius is subjected to a combination of axial compression and “off-axis” dorsal- and lateral-directed forces, which result in bending [3].

Using pQCT imaging, mechanical testing and finite element (FE) modeling, the objective of this research will be to develop and validate pQCT-based indices of bone strength under an off-axis loading scenario.

### Methods

**Specimens:** Ten cadaveric forearms (hand included) will be acquired from an anatomical tissue bank. We will scan distal radius using pQCT (at 4% site) and QCT (for FE modeling purposes). Forearms will be potted at the midshaft. Three tri-axial strain gauges will be applied to the distal radius at the 4% pQCT imaging site, located approximately 10mm proximal to Lister’s Tuberosity [4,5].

**Mechanical Testing:** Potted forearms will be aligned in a material testing system (MTS Bionix) with 15° of dorsal inclination and 3-6° of radial inclination [5,6]. Failure testing will be performed at 30mm/min onto the palm of the intact hand. Failure force, displacement and strain data will be gathered for each specimen.

**pQCT Imaging Analyses:** Custom image processing algorithms (Matlab) will be used to model the distal radius as a beam composed of cortical and trabecular bone. Using composite beam theory, trabecular and porous cortical bone will be converted to equivalent pure cortical bone using both linear and nonlinear approaches. Using axial strain measures and beam theory, the line of action of the force vector will be determined relative to the centroid and principal axes [4]. The line of action will provide required x,y offset values defining dorsal and lateral bending moments corresponding with off-axis loading. Derived bending moments and axial load will be used to generate strength indices for each individual pQCT pixel (e.g., strain, stress, failure load). Maximum and minimum strength indices will be correlated with experimental failure loads using linear regression.

**FE Analyses:** This research will be conducted in parallel with a PhD student. FE results will be used to cross-validate and refine pQCT-based strength indices.

### Results

This work is currently ongoing. Mechanical testing protocols have been developed [5] and potential pQCT-based strength indices have been investigated [7]. As well, FE models are currently being generated.

### Anticipated Conclusions

pQCT-based strength indices will predict distal radius failure occurring due to off-axis loading. Ultimately, pQCT-based strength indices may help to improve the prediction of distal radius fracture risk.

### References

- [1] Cuddihy et al., 1999; [2] Pistoia et al., 2002; [3] Troy and Grabiner 2007; [4] Edwards and Troy 2012; [5] Adam et al, 2014; [6] Augat et al., 1998; [7] Bespflug et al., 2014

## Multi Muscle Patterns In Post-Surgical Total Knee Arthroplasty

Cam Cummings<sup>1,2</sup>, Gregor Kuntze<sup>2</sup>, Janet Ronsky<sup>2</sup>

<sup>1</sup>Geomatics Engineering, University of Calgary <sup>2</sup>Clinical Movement Assessment Laboratory

### Introduction

Total Knee Arthroplasty (TKA) is a common surgical intervention for end stage Osteoarthritis (OA). It is implemented for pain relief and joint function restoration. There is an increasing expectation from patients concerning post-operative performance.<sup>1</sup> However, TKA patients often experience functional impairment such as movement, loading, and muscle activation pattern abnormalities.<sup>2</sup> This project focused on identifying temporal differences in muscle activations in lower limb electromyographs (EMG) between healthy persons and TKA patients, using wavelet patterns and machine learning classification.

### Methods

Ten post-surgical female TKA patients (TKA: 19±3 months post-surgery; 61.9±8.8 yrs) and 9 healthy age matched female controls (CON: 61.4±7.4 yrs) participated in this study. EMGs were collected during both level walking and stair climbing for 7 leg muscles: tibialis anterior (TA), gastrocnemius (GAS), semitendinosus (SEM), biceps femoris (BF), rectus femoris (RF), vastus medialis (VM) and vastus lateralis (VL). Five acceptable EMG trials per subject were selected for analysis, normalized in time (stance phase ±30%) and processed in Matlab using a wavelet transform.<sup>3</sup> EMG data were normalized to the total signal intensity. Support Vector Machine (SVM) classification was performed for all subjects using an iterative thresholding approach and leave-one-out cross-validation. Rates of classification (recognition rates) were deemed significant if they were greater than or equal to 68.4% (according to binomial test). SVM discriminants were visualized to aid in the identification of functional differences between CON and TKA groups.

### Results

Mean multi muscle patterns (MMPs) for walking (Fig. 1) demonstrate substantive differences between groups. The muscles that gave significant recognition rates in level

walking were: VM (68.4%) and BF (73.7%); and in stair climbing were: BF (84.2%), SEM (73.7%), GAS (68.4%), and TA (68.4%). The stair climbing task yielded a greater number of muscles with significant recognition rates, as well as higher recognition rates.

Temporal activation differences, indicative of muscle co-activation by TKA subjects, were observable in the discriminant pattern. In walking, BF and VM were active in mid-stance, illustrated as a red activity pattern in the discriminant. BF activity shifted from pre-HS to post-HS to coincide with the main activity in the quadriceps muscles (VL, VM, RF). In stair climbing, TA displayed a co-activation with GAS at mid-stance. Further, SEM and BF displayed pronounced activation patterns at mid-stance and at TO and early swing. This may indicate an activation strategy to assist in hip extension for the TKA group.

### Conclusions

The analysis approach chosen in this study identified functional differences between healthy subjects and TKA patients. There is evidence for the employment of co-activation strategy by the TKA group in both walking and stair climbing.

### References

1. Nilsson AK, et al. *Acta Orthop.* **80**:55–61, 2009
2. Catani F, et al. *Clin Biomech.* **18**:410–418, 2003
3. von Tscharner V, et al. *J Electromyogr Kinesiol.* **10**:433–445, 2000

Acknowledgements: funding from NSERC and Zymetrix.

### Figures

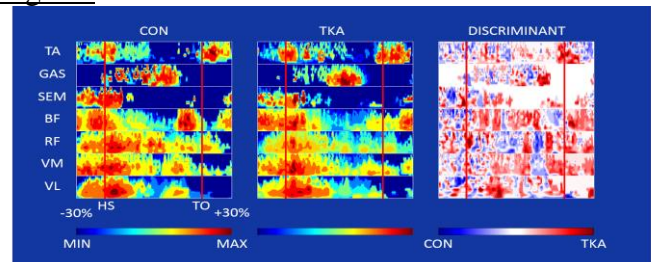


**Fig. 1:** Mean activity patterns and SVM discriminant produced for level walking (HS=heel strike, TO=toe off).

## A Novel Method for Comparison of Scan Greyscale Values Acquired Using Cone-Beam CT

Dietrich NH, Lagravere MO, Secanell M, Carey JP  
Mechanical Engineering, University of Alberta

### Introduction

In maxillofacial imaging the use of cone-beam computed tomography (CBCT) is becoming the go-to imaging tool due to accurate 3D output images. CBCT does not output Hounsfield Units (HU), which correspond to object density. Instead, due to low radiation requirements, CBCT outputs greyscale units which are only loosely related to object density. Several authors have suggested conversions for converting greyscale values to find density or HU.<sup>1-2</sup> This use of CBCT is considered inappropriate by many authors.<sup>3</sup> One factor is that different CBCT machines can give different greyscale results for the same object based on machine settings and manufacturer. An issue that has not been tested previously is the effect of weekly machine calibration on greyscale results. A method is proposed for testing the variations a single machine can give and for testing the variation between machines. A dry skull is then tested over five days to find if calibration effects occur.

### Methods

A dry skull was placed in a container filled with water to simulate tissue. The skull was placed in the machine as a patient would be placed to imitate a clinical setting. The skull was then imaged using identical settings seven times each day for 5 days. Calibration was performed at the beginning of each day. The proposed method works by locating two landmarks within the cranial base, shown as yellow circles in figure 1. A sphere is then centered on this point shown, inscribed in red on figure 1. In this study, the sphere has a radius of 30mm. The average of all greyscale voxels within this sphere is then computed and is used for comparison. A sensitivity analysis is performed using a single days scans where the landmark location is varied randomly up to 0.8mm. This is done 100 times for each scan of the day resulting in 700 scans over the entire day for analysis. The test is then repeated over 4 more days to test calibration effects.

### Results

Within a single scan's sensitivity analysis the max variation is 1.6 greyscale units. The 95% confidence interval for all sensitivity analysis scans is  $[-885.72, -885.63]$  greyscale. The mean value is -885.7 greyscale. The range of bone in the scans was 3100 greyscale units.

The multi-day test results are shown in figure 2. The results of the multiday comparison found statistically significant differences between days ( $P < 0.0005$ ). The largest variation in day average values was 7.4 greyscale units. The largest variation seen between all scans is 9.8 greyscale units.

### Conclusions

The proposed method appears to give consistent results. Variations due to potential landmark placement error are smaller than the apparent variation within a single day's scans. Using this method, it appears that calibration has an effect on the average greyscale value for the dry skull being imaged. The variation is small compared to the range of greyscale values of bone within the images and may not be clinically significant, depending on application.

### References

1. Lagravere MO et al. DMFR 2006 Nov;35(6):407-409.
2. Mah P et al. DMFR 2010 Sep;39(6):323-335.
3. Spin-Neto R et al. DMFR 2014;43(4):20130376.

### Figures



Figure 1. 3D Render of Dry Skull, landmarks shown in yellow. Sphere inscribed in red.

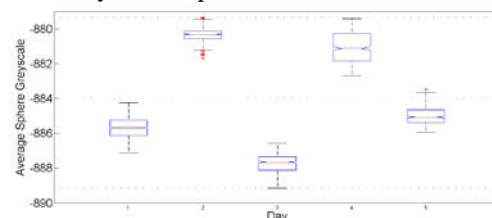


Figure 2. Tukey Boxplots of Sphere Method Results for each Day

## Micro-tissue engineering for retinal transplant

Abdullah Al-Ani and Mark Ungrin

Over 100 million people worldwide are visually impaired due to retinal degenerative diseases such as age-related macular degeneration. This group of diseases leads to the irreversible loss of light sensitive photoreceptors. Yet current clinical therapies are aimed at merely slowing the degeneration of photoreceptors. In contrast, cell replacement therapies promise to regenerate diseased retinas; however, one of the major challenges is minimal survival and engraftment of transplanted photoreceptors. This may be due partially to the absence of healthy retinal pigment epithelium (RPE), the layer responsible for providing trophic support to photoreceptors under physiological conditions. To address this, we plan on employing micro-scale tissue engineering techniques to develop an effective retinal cell delivery system that improves transplants survival and integration. We hypothesize that co-culturing cone photoreceptor committed precursors with RPE cells as sub-millimeter aggregates will enhance *in vitro* photoreceptor survival, cellular organization, maturation, polarization and axonal outgrowth, compared to single cell suspension. Photoreceptors from P4 NRL<sup>-/-</sup> X Ccdc136-GFP mice are co-aggregated with mCherry<sup>+</sup> RPE cells using the AggreWell system and characterize for: (1) interactions between RPE and photoreceptors using live-cell imaging; and (2) cone survival, maturation, and axon outgrowth using immunocytochemistry, RT-PCR and confocal microscopy. We have successfully generated these aggregates in various sizes and RPE:photoreceptor ratios, and characterization is underway. This novel approach will provide an effective retinal cell delivery system that improves the integration of retinal transplants. Overcoming this obstacle is an essential step in the road of correcting the presently irreversible vision loss associated with retinal degenerative diseases.

## Investigating associations between OA-related knee pain and mechanical behavior using subject-specific finite element modeling of the knee

Arjmand, H<sup>1</sup>; Nazemi, M<sup>1</sup>; Burnett, WD<sup>1</sup>; Kontulainen, SA<sup>1</sup>; McLennan, CE<sup>2</sup>;  
Hazel, D<sup>2</sup>; Talmo, C<sup>2</sup>; Hunter, DJ<sup>3</sup>; Wilson, DR<sup>4</sup>; Johnston, JD<sup>1</sup>

1. University of Saskatchewan, Saskatoon, SK; 2. New England Baptist Hospital, Boston, MA;  
3. University of Sydney, Sydney, NSW; 4. University of British Columbia, Vancouver, BC

**Introduction:** Knee osteoarthritis (OA) is a painful and debilitating joint disease. Pain is the dominant symptom of OA [1]; however, the source of OA-related pain is poorly understood [2]. Although OA is generally considered as a cartilage disease, the OA knee is marked by other changes, such as altered subchondral bone volume and mechanical properties, cyst presence, osteophyte formation and malalignment. It is currently unknown what role these structural changes have in OA-related pain.

Subject-specific finite element (FE) modeling has potential to clarify the role of structural changes in OA-related knee pain. These models can be evaluated computationally (and noninvasively) to assess local stiffness, internal stress and strain distributions *in vivo* which cannot currently be measured experimentally. Our group has previously developed and validated a FE model of the knee [3].

The first objective of this study will be the test the precision of FE-based mechanical measures at the proximal tibia and distal femur (e.g., stiffness, max/min/average stress and strain distributions). Using the most precise measures, the second objective will be to explore associations between FE-based mechanical measures with knee pain.

### Methods

**Precision Study:** Fourteen participants (2 men, 12 women; mean age 51.4, SD 11.8 years) were previously scanned using clinical quantitative CT (QCT) 3 times.

**FE Modeling:** The distal femur, proximal tibia and fibula will be segmented from surrounding bones using segmentation software (ANALYZE). A surface will be generated from each bone using reverse engineering software (GEOMAGICS) and converted to volumes. The volumes will be imported into FE software (ABAQUS) and meshed using 10-noded tetrahedral elements. To simulate soft tissues in the knee, bones

will be surrounded by an incompressible cylindrical medium [4]. A custom code (Matlab) will be used to map imaged bone mineral density (BMD) to bone's elastic modulus (E) [5-6]. For surrounding soft tissues, homogeneous, incompressible and isotropic material properties will be applied (E=10MPa; Poisson's=0.495) [4]. Body weight will be applied through the femur's most proximal portion. The most distal sections of tibia and fibula will be constrained in all direction; femur's most proximal section will be constrained laterally. Mechanical measures of stiffness and stress/strain distributions will be acquired for the proximal tibia and distal femur (Matlab, ABAQUS).

**Statistical Analysis:** Root mean square coefficients of variation (CV%) will be used to assess repeatability.

**Pain Study:** The preoperative knee of 52 patients (23 men, 29 women, mean age 64, SD 9.4 years) were previously scanned in the same manner as the previous study. Participants were scored for pain using Western Ontario and McMaster Universities Arthritis Index (WOMAC) [7].

**Statistical Analysis:** Spearman's rank correlations will be used to determine associations between WOMAC pain scores and FE-based mechanical measures.

### Anticipated Conclusions:

This study will lead to a precise FE model of the OA knee linked with measures of OA-related knee pain. This study will validate new tools with potential to improve our understanding of the role of subchondral bone in OA-related pain pathogenesis.

### References:

[1] McAlindon et al., 1992; [2] Lo et al., 2009; [3] Nazemi et al., 2013; [4] McErlain et al., 2011; [5] Goulet et al., 1994; [6] Rho et al., 1995; [7] Bellamy et al., 1988

## A novel method to fabricate biodegradable stents for stroke treatment

D. Wang<sup>1</sup>, X. HAN<sup>2</sup>, M. Kelly<sup>3</sup>, and X.B. Chen<sup>2,4</sup>

<sup>1</sup>Department of Medicine, University of Saskatchewan, Saskatoon, Canada, S7N5E5

<sup>2</sup>Department of Mechanical Engineering, University of Saskatchewan, Saskatoon, Canada, S7N5A9

<sup>3</sup>Department of Neurosurgery, University of Saskatchewan, Saskatoon, Canada, S7N5E5

<sup>4</sup>Division of Biomedical Engineering, University of Saskatchewan, Saskatoon, Canada, S7N5A9

### Introduction

Being able to control the drug release and to reduce in-stent neointimal formation, biodegradable stents are considered promising for use in the stroke treatment. With the degradation of the stents, only is healed arterial vessel left behind. However, the conventional methods of fabricating biodegradable stent, such as laser machining and monofilaments braiding, are time-consuming and expensive; and lack precise control over the stent microstructure. Recently, as an emerging fabrication technique, the dispensing-based rapid prototyping (DBRP) allows for more accurate control over the scaffold microstructure [1]. Based on this technique, this paper presents a novel method to fabricate biodegradable stents for stroke treatment.

### Methods

For stroke treatment, biodegradable stents should possess appropriate mechanical properties, featured by the sufficient radial strength and flexibility. For this, Polycaprolactone (PCL) was chosen and dissolved in chloroform for stent fabrication, and the DBRP technique is creatively utilized to drive the 50% w/v PCL solution out of a needle (with a diameter of 410  $\mu\text{m}$ ), depositing on the mandrel and thus forming the stents of tubular structure (Figure 1). To accurately deposit the designated material, the air pressure (100psi) and the moving speed of the needle (0.3 inch/sec) were carefully determined by means of the models developed by our previous study [1]. Also, the angular velocity of the mandrel and the speed of the dispensing head were coordinated and programmed in order to fabricate the stents with structure as desired.

### Results

The results illustrated that DBRP is a promising technique for fabricating

biodegradable stents, with the good control over their structure. Stents fabricated with varying patterns are shown in Figure 2, in which the overall size of stents is 2 mm in diameter and 20 mm in length, with a strut diameter of 410  $\mu\text{m}$ . The mechanical properties of stents fabricated was examined qualitatively and it was found that molecular weight of PCL played an important role in the mechanical properties of stents. Stents with low molecular weight of PCL tend to be brittle, while mechanical properties of stents are significantly improved by high molecular weight PCL, which are more elastic and flexible.

### Conclusions

Biodegradable stents with proper mechanical properties for stroke treatment can be directly fabricated from polymer powders through DBRP technique, which would not be possible by means of conventional methods. Thus, the DBRP technique can contribute to accelerating the stent product development process.

### References

[1] Li, M., X. Tian, and X.B. Chen, *A brief review of dispensing-based rapid prototyping techniques in tissue scaffold fabrication: role of modeling on scaffold properties prediction*. Biofabrication, 2009. **1**(3): p. 032001.

### Figures

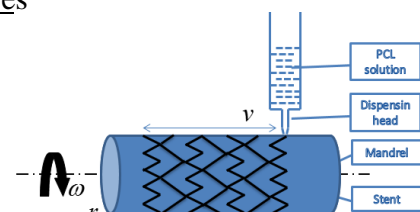


Figure 1. Fabrication process for stents

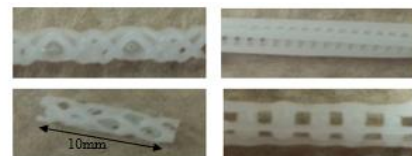


Figure 2. Various patterns of biodegradable stents